Msc. Thesis in Aerodynamics & Wind Energy

Application of Acoustic Metamaterials in Boundary Layer Instability Control

Coert de Koning

2021

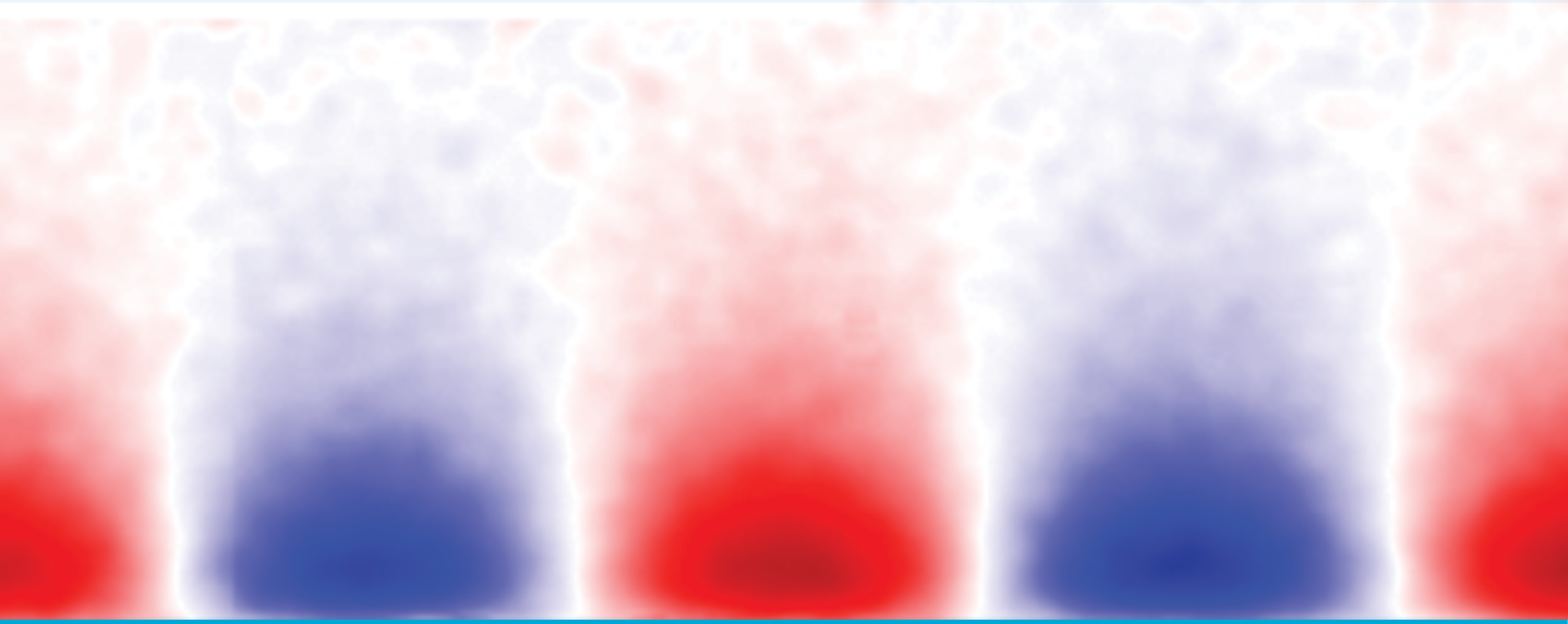

APPLICATION OF ACOUSTIC METAMATERIALS IN BOUNDARY LAYER INSTABILITY CONTROL

A thesis submitted to the Delft University of Technology in partial fulfilment of the requirements for the degree of

Master of Science in Aerospace Engineering

by

Coert de Koning

April 2021

Coert de Koning (4376951): *Application of Acoustic Metamaterials in Boundary Layer Instability Control* (2021)

The work in this thesis was made in the:

Section of Aerodynamics
Department of Aerodynamics & Wind Energy
Faculty of Aerospace Engineering
Delft University of Technology

Supervisors:	Dr. M. Kotsonis	(Committee Chair)
	Dr. T. Michelis	
External examiner:	Dr. D. Ragni	

ABSTRACT

In order to reduce skin friction drag on wings, laminar-to-turbulent transition of boundary layers should be delayed. This can be achieved by controlling instabilities, Tollmien-Schlichting (TS) waves, inside a laminar boundary layer to inhibit the process from receptivity to turbulence. Studies about actively actuated methods are successful in attenuating these waves by changing the flow conditions or by counteracting the TS waves. However, methods that do not require an energy input, have not successfully achieved TS wave damping in a practical aeronautical situation. Novel concepts of acoustic metamaterials show extraordinary behaviour in sound wave manipulation. Sub-wavelength resonant meta-atoms structured in an array or lattice, form a system that could completely suppress sound wave transmittance for a particular frequency. Since TS instabilities inside a laminar boundary layer behave like convective waves, the objective of this project is to study whether an acoustic metamaterial concept is applicable for TS wave damping.

To investigate this, the desired wall controller property of the metamaterial and the interaction between a TS wave and a single meta-atom are evaluated. For this study, a Helmholtz resonator was used as the meta-atom. To satisfy the research objective, a PSE solver is modified to enable the possibility of imposing inhomogeneous boundary conditions. Besides this, linearised Navier-Stokes simulations in COMSOL Multiphysics and a wind tunnel experiment are used to investigate the interaction in detail.

Similar to the impedance in acoustics, the relation between pressure and wall-normal velocity is an important wall controller property to reach TS wave damping. In general, optimal TS wave attenuation is achieved if the pressure and wall-normal velocity are in-phase. TS wave amplification is obtained if these parameters are more than (approximately) 90° out of phase. A thermoviscous acoustics simulation in COMSOL is used to characterise the velocity-pressure relation for a Helmholtz resonator with the assumption that the resonator behaves purely acoustic. A single Helmholtz resonator is not reaching an attenuating phase relation between pressure and velocity for the tested frequency range. This means that a TS wave is only amplified by a Helmholtz resonator.

This hypothesis, based on numerical models, is endorsed by the experimental results. The qualitative result of the interaction between a TS wave and a Helmholtz resonator is that the TS wave is amplified. The magnitude of amplification is dependent on the difference between the TS wave frequency and the resonant frequency of the resonator. Besides this, the resonator emits an acoustic wave, which leads to a global fluctuating pressure in the background. The experimental results are in good agreement with the outcomes of the linearised Navier-Stokes simulations. The adjusted PSE solver, coupled with the thermoviscous acoustics simulation, can only give qualitative information on the interaction due to solver stability limitations and possible oversimplifications in the model.

All in all, acoustic metamaterials can be applicable to control boundary layer instabilities if the desired velocity-pressure relation can be reached. A single meta-atom, in the form of a Helmholtz resonator, does not meet this requirement. However, subsequent research should demonstrate whether a structure of Helmholtz resonators or another acoustic metamaterial concept could be applied to control boundary layer instabilities.

PREFACE

With this thesis, I finish my time as a TU Delft student. I want to use this page to say thanks to the people who helped me achieving the Masters degree in Aerospace Engineering.

First of all, I want to thank my supervisors Marios and Theo. Our numerous meetings helped me a lot in progressing through my thesis and with your feedback on my work, I think that I created a nice piece of research. When I had my first conversation with Marios about a thesis subject, I only had a little idea what he was talking about. A study including a literature review, developing a numerical model, several simulations and two wind tunnel campaigns gave me a lot of insights into the interesting area of boundary layer transition. Special thanks to Theo who was always available to help me out and who made my time in the wind tunnel definitely more enjoyable.

Besides my direct supervisors, I want to thank all the other people who are working in the Low Speed Laboratory. Especially Giulia, Kaisheng and Emiel, always took time to help me out whenever I needed. This did not only include technical advise, but also culinary. Giulia explained me the ins and outs of the Italian kitchen, where Kaisheng let me taste some new Chinese dishes and Emiel introduced me to the classic sandwich Kip Milano.

Furthermore, I want to say thank you to the project group I had a good time with during my Bachelor phase and the friends I kept from my time at Eco-Runner Team Delft. They certainly made me feel more comfortable in Delft. Special thanks to Sid, Reinier and Gijs who brought some joy to the Masters projects, classes and coffee breaks. When Covid-19 hit us, and a lot of fun things in life were cancelled, my roommates gave me the distraction I needed during my thesis time. Suddenly everybody needed to stay at home and we made the best of it. Thank you for the time that I never wanted to miss.

Last, but definitely not least, I am incredibly thankful to my parents who made my study time possible. Although they, my brother and other family had probably no idea what I was talking about, they always listened to me and my study related problems and tried to help me out. The same holds for my friends from Zevenbergen, although we were all studying or working in different parts of the Netherlands, we still got time to have fun in the weekends. I am also very grateful to my girlfriend Marieke, who was always interested in what I was doing and she kept motivating me to reach to this degree. Although she studies at the other side of the country, she was always there for me when I needed her.

Without all the people that I mentioned (and the ones that I forgot) my time as a student would have been a lot less interesting and more boring. It was a great experience that I will never forget!

Coert de Koning
April 2021

Contents

List of Figures

List of Tables

SYMBOLS AND ABBREVIATIONS

Abbreviations

2D	Two-dimensional
3D	Three-dimensional
AC	Alternating Current
DBD	Dielectric Barrier Discharge
FEM	Finite Element Method
FOV	Field Of View
FSI	Fluid-Structure Interaction
HR	Helmholtz Resonator
LHS	Left Hand Side
LQG	Linear Quadratic Gaussian
LST	Linear Stabilty Theory
NS	Navier-Stokes
OS	Orr-Sommerfeld
PIV	Particle Image Velocimetry
PSD	Power Spectral Density
PSE	Parabolised Stability Equations
PTV	Particle Tracking Velocimetry
RHS	Right Hand Side
RMS	Root Mean Square
TS	Tollmien-Schlichting
UAC	Ultrasonic Absorbing Coating

Notation

$.^*$	Dimensional quantity
$\cdot_x$	Derivative to x (d/dx)
$\langle . \rangle$	Averaging operator
$\tilde{.}$	Normalised quantity

Complex number convention

$\cdot_i$	Imaginary part
$\cdot_r$	Real part
$\Im(.)$	Imaginary part
$\Re(.)$	Real part
i	Imaginary unit ($\sqrt{-1}$)

Symbols

α	Steamwise wavenumber
β	Spanwise wavenumber
Δ	Difference
δ^*	Displacement thickness
δ_ν	Viscous penetration depth
δ_{99}	Boundary layer thickness
ϵ	Electric permittivity
η	Gas viscosity
λ	Wavelength
$\mathbf{q}$	Eigenvector
μ	Magnetic permeability
μ_m	Medium viscosity
μ_f	Dynamic viscosity of the fluid
∇	Laplace operator
ν	Kinematic viscosity
ω	Angular frequency
ϕ	Phase angle
ρ	Density
ρ_{eff}	Effective mass/density
Σ	Summation
σ	Stress
σ_x	Standard deviation
τ_g	Group delay
τ_w	Shear stress at wall
θ	Momentum thickness
A	Amplitude
a	Acceleration
B	Bulk modulus

C	Resonator configuration
c	Speed of sound
C_f	Friction coefficient
C_p	Pressure coefficient
D	Derivative to y (d/dy)
$f\#$	Aperture size
f	Frequency
F_{BC}	Multiplication factor
H	Height
k	Wavenumber
L'	Corrected throat length
M	Mach number
N	Amplification factor
n	Amount of samples
n	Refractive index
N_{im}	Amount of images
P	Performance
p	Pressure
q	Displacement
R	$\sqrt{Re_{\delta^*}}$
Re_L	Length based Reynolds number
Re_{δ^*}	Displacement thickness based Reynolds number
S	Cross sectional area
t	Time
U	Uncertainty
u	Steamwise velocity component
U_∞	Freestream velocity
V	Volume
v	Wall normal velocity component
v_p	Point velocity
V_{pp}	Peak to peak voltage
w	Spanwise velocity component
x	Streamwise direction
y	Wall normal direction
Z	Impedance
z	Spanwise direction

1 INTRODUCTION

This thesis describes a feasibility study to the use of acoustic metamaterials in boundary layer instability control. A literature review to this subject is discussed and different numerical techniques are used to investigate the interaction between boundary layer instabilities and metamaterials. Moreover, experimental wind tunnel tests are performed to investigate the behaviour of the instabilities more elaborately to eventually come up with a physical framework describing the interaction.

In this first chapter of the thesis, some introductory background information will be given to outline the research framework. The importance of the research will be addressed and this will lead to a problem formulation. At the end of this chapter, the research questions and objectives will be given.

1.1 RESEARCH FRAMEWORK

Already since the early 1900s, people are interested in the flow past their objects and boundary layers. In that time, they observed that flows were either laminar or turbulent and that laminar boundary layers become turbulent. There was no explanation for this phenomenon until Walter Tollmien published his findings [1]. Within Germany, the idea of instability growth to turbulence was further developed by Hermann Schlichting [2]. Their idea was that there are growing vortex-like waves inside a boundary layer and when they become large enough, the laminar boundary layer becomes turbulent. These waves are now known as Tollmien-Schlichting (TS) waves.

In Germany, researchers generally agreed to the idea of having growing instability waves that cause turbulence. Outside of Germany, this was different and that was mainly caused by unsuccessful observance of these waves. In that time it was impossible to show the presence of the waves, until Schubauer and Skramstad published their findings in 1947 [3]. They used hot wire anemometry as their flow measurement technique to confirm the Tollmien-Schlichting theory, which suggests that the amplitude of an instability wave grows selectively based on Reynolds number and frequency.

Small environmental disturbances are present in the flow and these can be perceived by the boundary layer in a process called receptivity. From here, there are multiple paths that can be followed in order to reach transition to turbulence. These paths are presented in figure 1.1a. For a flat plate model without pressure gradient or sweep angle path ”A” is assumed to be followed. From receptivity, small instabilities result in growth of the primary modes that will eventually break down into turbulence. In other situations, different paths will be followed to reach this transition.

The main benefit of delaying or even preventing the transition process in a subsonic boundary layer is drag reduction. Skin friction drag is dependent on the shear stress at the wall, which is a function of the derivative of the u-velocity to y, the wall normal direction, near the wall. The corresponding formulas are given in equations 1.1 and 1.2. For a laminar boundary layer, this term $\partial u/\partial y|_{\text{wall}}$ is smaller than for a turbulent boundary layer, this can be seen in figure 1.1b. For reduction of the skin friction and the overall drag accordingly, boundary layer transition should be delayed. There are methods that achieved this, but all successful methods that are practical in an aeronautical application need an input of energy. The net energy win by controlling the flow is therefore the difference between the energy used by the controller and the energy saved from drag reduction. The concepts in literature that describe boundary layer instability control for aeronautical applications that do not require an energy input are very limited and this opens a gap for the study described in this thesis.

$$\tau_w = \mu_m \frac{\partial u}{\partial y}|_{\text{wall}} \tag{1.1}$$

$$C_f = \frac{\tau_w}{\frac{1}{2}\rho U_\infty^2} \tag{1.2}$$

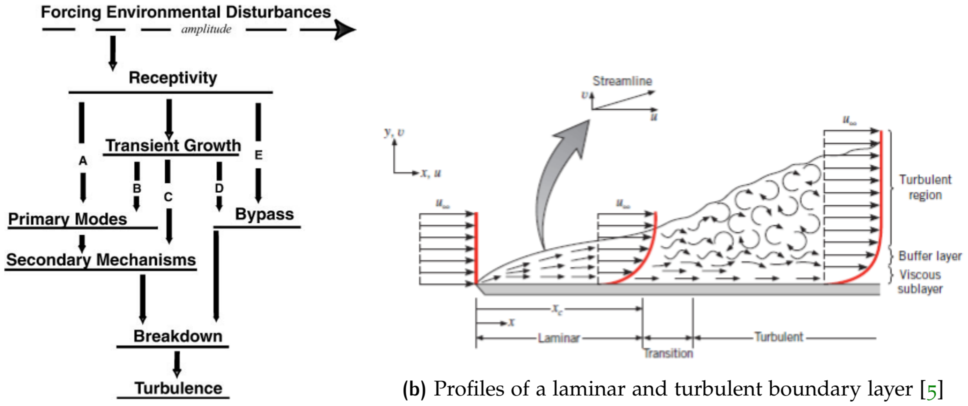

(a) Different paths from receptivity to transition [4]

(b) Profiles of a laminar and turbulent boundary layer [5]

Figure 1.1

In the first years of this century, acoustic materials were first reported in the papers by Fang et al. [6] and Yang et al. [7]. They showed that materials or surfaces with a specific arrangement of small resonant units could lead to exceptional acoustic wave manipulative behaviour. Small structures were able to suppress certain frequencies from the sound spectrum in ways that were never possible with natural materials. This invention opened the doors to a whole new research area in acoustics.

With this new way of manipulating waves and the fact that laminar-to-turbulent transition can be induced by wave-like instabilities, an investigation of the possibilities to use acoustic metamaterials in instability control needs to be made. The research described in this thesis is a first evaluation of using metamaterial concepts from acoustics to get a method for boundary layer instability control that does not require an energy input.

From the broader spectrum of possible acoustic metamaterials, the concept which uses an array or lattice of Helmholtz resonators is a promising one. The Helmholtz resonator serves as the meta-atom in this metamaterial system. In multiple studies, sound wave damping with this kind of acoustic metamaterial was demonstrated [6] [8] [9] [10]. In a study by Fey & Robertson [11], it was shown that even a single Helmholtz resonator is able to damp sound of some frequencies in a waveguide experiment. In this research, an investigation is made on how a TS wave in a laminar boundary layer would respond to a single Helmholtz resonator. The influence of a spanwise row of resonators to the turbulence inside a boundary layer was tested by Flynn et al. [12] and a Helmholtz resonator was used to delay flow separation in a study by Lin et al. [13] without success. A more elaborate description of their work is given in section 2.4. Studies to the use of Helmholtz resonators to suppress growing instability modes inside a laminar boundary layer are only limitedly available in literature.

1.1.1 Boundary layer stability

The theory of Walter Tollmien and Hermann Schlichting [1] [2] about growing convective vortex-like instabilities in the boundary layer that eventually lead to transition was later expanded to the boundary layer stability theory that is now commonly used. This theory is known as Linear Stability Theory (LST) that can describe the growth of the TS waves in their linear phase. This theory, which is described in the report of Mack from 1984 [14], is widely used and verified with experimental data. The mathematics behind this theory represent the wave-like nature of the instability as well as the way they are growing or shrinking. Boundary layer transition is often linked to a critical Reynolds number, with this linear stability theory and the path to transition in figure 1.1a, it is indicated that this is not necessarily correct. There are ways to manipulate the unstable mechanisms inside a laminar boundary layer to force or delay transition and this can be evaluated using the stability theory of Mack [14].

There is another boundary layer stability theory with some different assumptions, called Parabolised Stability Equations (PSE). This was described in a paper by Herbert in 1993 [15]. Both of the stability theories are presented in this section and eventually a comparison is shown to say whether their stability predictions match. Both theories have advantages and disadvantages depending on the application. In the current study, the interaction between an acoustic metamaterial and a boundary layer instability is investigated. Eventually this is done experimentally, but in order to predict the experimental outcome and to create a physical framework of the interaction, the stability theories presented in this section are used.

Linear Stability Theory

The linear stability theory (LST) that gives the stability of an incompressible laminar boundary is described in the report written by Mack [14]. The main procedure to evaluate the stability of a boundary layer is described here.
The derivation starts with the three-dimensional Navier-Stokes equations for a viscous, incompressible fluid, given in equation 1.3.

$$\begin{aligned} \frac{\partial \bar{u}_i^*}{\partial t^*} + \bar{u}_j^* \frac{\partial \bar{u}_i^*}{\partial x_j^*} &= -\frac{1}{\rho^*}\frac{\partial \bar{p}^*}{\partial x_i^*} + \nu^* \nabla^2 \bar{u}_i^* \\ \frac{\partial \bar{u}_i^*}{\partial x_i^*} &= 0 \end{aligned} \tag{1.3}$$

Where $.^*$ denotes a dimensional quantity, u_i the velocities in three directions and x_i the three different directions, where x is streamwise, z is spanwise and y is normal to the wall, i,j are 1 to 3 according to the summation convention.

The terms in equation 1.3 are all dimensional, these quantities can all be nondimensionalized with a velocity, length and pressure scale. The flow can be divided into a steady mean flow term and an unsteady disturbance term U_i and u_i respectively. The same can be done to the pressure. Since this is linear stability theory, the terms that are quadratic in the small disturbance are dropped. The Navier-Stokes equations then reduce to the following dimensionless linearised equations.

$$\begin{aligned} \frac{\partial u_i}{\partial t_j} + u_j \frac{\partial U_i}{\partial x_j} + U_j \frac{\partial u_i}{\partial x_j} &= -\frac{\partial p}{\partial x_i} + \nu \nabla^2 u_i \\ \frac{\partial u_i}{\partial x_i} &= 0 \end{aligned} \tag{1.4}$$

The assumption is made that there is truly parallel mean flow. Therefore, the mean V-velocity is zero and U, W are only functions of y. The solutions of these equations are assumed to be normal-mode solutions in the form of equation 1.5.

$$[u, v, w, p]^T = [\hat{u}(y), \hat{v}(y), \hat{w}(y), \hat{p}(y)]^T \, e^{i(\alpha x + \beta z - \omega t)} \tag{1.5}$$

In this equation, the terms denoted with a hat are the eigenfunctions. They describe the shape of the wave at a certain point in the domain. The term that is in the exponent describes how the wave travels through the domain.
If the solution ansatz is inserted in equations 1.4, it can be reduced to a fourth-order system of equations. Homogeneous boundary conditions can be assumed as well as the W-velocity and β term to be zero. This reduces equations 1.4 to the Orr-Sommerfeld equation (1.6), named after William McFadden Orr and Arnold Sommerfeld who derived the equation first.

$$(D^2 - \alpha^2)^2 \hat{v} = iR \left[(\alpha U - \omega)(D^2 - \alpha^2) - \alpha D^2 U \right] \hat{v} \tag{1.6}$$

This Orr-Sommerfeld (OS) equation is the basis for most of the work that has been done in incompressible stability theory [14]. The outcome of this eigenvalue problem characterises the shape and behaviour of the TS wave. In the equation, the only part of the eigenfunctions taken into account is the $\hat{v}$ component. The other components ($\hat{u}$, $\hat{w}$ and $\hat{p}$) can be derived via this term since these have a fixed relation. This means that also the phase relation between the velocity components and the pressure of a TS wave is fixed.

Using the spatial amplification theory, it can be determined whether an instability of a certain form amplifies or damps out. This is all dependent on the term $-\alpha_i$, the growth rate. This is the negative of the imaginary part of the streamwise wavenumber. The three possible outcomes correspond with three effects.

$$\begin{aligned} -\alpha_i &< 0 \quad \text{damped wave} \\ -\alpha_i &= 0 \quad \text{neutral wave} \\ -\alpha_i &> 0 \quad \text{amplified wave} \end{aligned} \tag{1.7}$$

Using this linear stability theory, for a specific boundary layer, its stability can be calculated for a certain frequency at a certain Reynolds number (Re_{δ^*} used as a length scale) or x-location. For a certain free stream velocity, a stability diagram can be created by solving the OS equation for different frequencies at different x-locations. An example of such stability diagram is given in figure 1.2 for a free stream velocity of 10 m/s and no pressure gradient. As this is an example, this stability diagram does not represent the experimental situation. The linear stability theory described in the paper by Mack [14] is also compared to some experimental studies. The predicted outcomes of the LST calculations show good agreement with these hot wire measurements [14].

Figure 1.2 gives the information with a non-dimensional x-axis, where the streamwise location is given as the Reynolds number based on the displacement thickness (Re_{δ^*}). The left figure gives the imaginary part of the steamwise wavenumber in the spectrum. In red, the neutral curve ($\alpha_i = 0$) is highlighted. The middle figure of

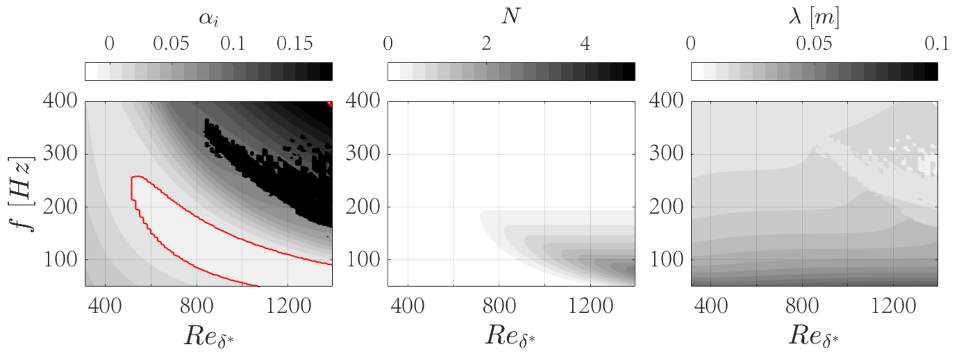

Figure 1.2: Dimensional stability diagrams of a boundary layer computed with LST with a free stream velocity of 10 m/s, on the left the imaginary part of the streamwise wavenumber with in red the neutral curve ($\alpha_i = 0$), in the middle the calculated N-factor and on the right the wavelength is given

the three gives the value of N in the spectrum. This is calculated as Van Ingen [16] described in his paper and the main equation is given below.

$$N = \ln(A/A_0) = \int_{x_0}^{x} -\alpha_i \mathrm{d}x \tag{1.8}$$

The N-factor is therefore seen as an amplification factor, which is the integral over x of the instability of the wave. The method is also called e^N. This term gives the amplification ratio, the ratio between an initial instability amplitude and the instability amplitude at a certain streamwise location. The factor N can be calculated from LST or another stability theory via the streamwise integral of the growth rate and via the amplitude ratio from numerical simulations and experiments. Besides that, the N-factor is a non-dimensional number. This makes the N-factor a direct method for comparison between numerical and experimental data.

The theory by Van Ingen [16] and Smith & Gamberoni [17] claims that the transition from a laminar to a turbulent boundary layer starts naturally when the ratio between the initial amplitude of the instability and the magnitude of the amplified TS wave reaches a certain value. The important factor in transition is therefore the ratio rather than the absolute magnitude. This theory has been successfully used as an engineering tool ever since the paper was published. The theory can also characterise the free stream turbulence level. It must be noted that the N-factors presented in figures 1.2 and 1.3 are only calculated over parts where α_i is negative.

The most right part of figure 1.2 shows the wavelength corresponding to a certain frequency and at a certain location in the domain. This λ can be calculated from the real part of the streamwise wavenumber α_r, which is also dependent on the frequency and Reynolds number.

Parabolised Stability Equations

The use of LST to evaluate the stability of a boundary layer has proven to be accurate, despite all the assumptions that are used. In 1993, a new theory to capture boundary layer stability with less/other assumptions was published in a paper by Herbert [15]. This method uses the approach of Parabolised Stability Equations (PSE). It starts at the same point as LST, but it makes a different ansatz for the solution mode, given in equation 1.9.

$$\mathbf{q}'(x,y,z,t) = \mathbf{q}(x,y)\, e^{(i\theta(x)+i\beta z-i\omega t)} \qquad \text{With: } \theta_x = \alpha(x) \tag{1.9}$$

The eigenfunctions ($\mathbf{q}$) are a function of x and y, contrary to LST, where it was only a function of y. This can be seen as less of an assumption than the LST ansatz.

Moreover, LST only uses the u-velocity field to solve the OS equation at a specific x-location, where PSE also includes the v-velocity field and the derivatives to y of these velocity fields. PSE solves a system of equations by marching though the domain and it requires knowledge of the previous spatial step. LST on the other hand, solves an eigenvalue problem at a streamwise location, independent of the solution at the other steps.

In order to make the equations solvable, the RHS of equation 1.9 can be divided into a slowly varying term and a quickly varying term. Because $\mathbf{q}$ and α are slowly varying, the derivatives are small. Therefore, terms with $\mathbf{q}_{xx}$, α_{xx}, or products $(\mathbf{q}_x\alpha_x)$ or higher derivatives will be neglected. The parabolised equation can be written in a compact from, this is given in equation 1.10.

$$L\mathbf{q} + M\frac{\partial \mathbf{q}}{\partial x} + \frac{d\alpha}{dx}N\mathbf{q} = \mathbf{0} \tag{1.10}$$

Where L, M and N are operators that only act in y.

The PSE solver will calculate the stability of the TS wave in a boundary layer by marching through the domain. It needs a starting point at x_0, so at this point, LST is used to compute the initial conditions. After that, at each x station, the solver iterates until convergence is reached and then it marches to the next x station. It does this for a specific frequency and if a sweep over a set of frequency is taken, similar stability diagrams can be computed using PSE as shown in figure 1.2 for LST. In this way, the outcomes of solvers using these different approaches can be compared.

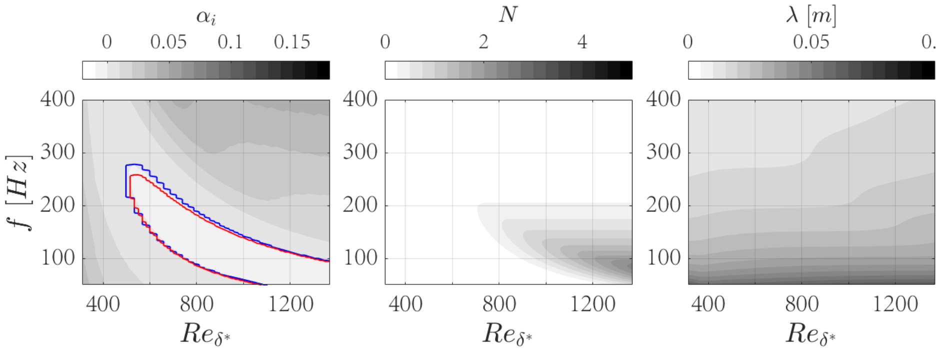

Figure 1.3: Dimensional stability diagrams of a boundary layer computed with PSE with a free stream velocity of 10 m/s, on the left the imaginary part of the streamwise wavenumber with in red the neutral curve ($\alpha_i = 0$) calculated with PSE, in blue LST, in the middle the calculated N-factor and on the right the wavelength is given

The left figure of figure 1.3 shows the neutral curves as they are calculated with LST (blue) and PSE (red). Close to the leading edge, for higher frequencies, the two curves show some differences. However, for the lower frequencies, the two curves are very similar. This also holds for the N-factor and wavelength λ calculations.

Eventually, as mentioned at the beginning of this section, a solver based on either of the two presented stability theories could be used as a tool to predict the behaviour of TS waves in the boundary layer during the experiment. The chosen approach that is most suitable for the current application is PSE. The reason why this method is chosen over LST is the possibility to add periodic inhomogeneous boundary conditions to the problem for both u- and v-velocity. In LST, only the u-velocity field is taken as an input to the calculation. In this way, the reaction from any metamaterial or another wall controller to the flow can be simulated. The PSE solver comes with lower computational costs because it computes its solution based on a matrix inversion. The LST solver, on the other hand, ends up with an eigenvalue problem and an extra algorithm to find the eigenvalue corresponding to the TS wave. Before an modified PSE tool including inhomogenous boundary conditions can be used, the homogeneous version should be validated to a reference. Since LST is proven experimentally [14], this can serve as the reference.

In order to compare the two methods, one can look at the stability diagrams given in figure 1.3. Besides that, the stability of a single TS wave frequency over the domain can be evaluated with both methods. For a fixed combination of the free stream velocity and TS wave frequency, the development of the amplification factor N is given over x as well as the growth rate α_i. An example is given in figure 1.4a for a free stream velocity of 10 m/s and a frequency of 100 Hz. The N-factor in figure 1.4b was calculated starting from the x-location of neutral stability ($\alpha_i = 0$). This represents the stability of a wave initiated at the point of neutral stability. A wave introduced earlier would first be damped in amplitude upstream of the neutral stability point.

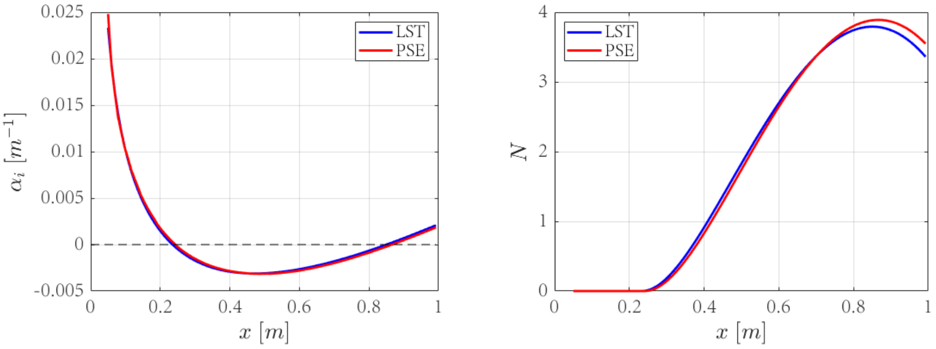

(a) Growth rate α_i

(b) N-factor

Figure 1.4: TS wave stability for a free stream velocity of 10 m/s and a frequency of 100 Hz

In the figures that show the development of α_i, a dashed line is added at $\alpha_i = 0$ to show when the neutral curve is intersected. It can be seen that the lines representing LST and PSE in figure 1.4 is that they are closely together, especially for the values of α_i. There is only a small difference noticeable in the N-factor. The biggest difference is in the height of the maximum N-factor and the x-location of this maximum and even this difference is small taken into account that the N-factor is very sensitive to small changes because it is an integral quantity. The comparison is also not completely objective because the starting points for the current N-factor calculation is chosen to be the intersection with the $\alpha_i = 0$ line. This point is not exactly the same for the LST and PSE calculations.

In general, the conclusion can be drawn that the PSE solver predicts the TS wave stability accurately, comparably with the LST solver. The main advantage of using PSE is, as mentioned earlier, that there is a possibility of implementing a periodic inhomogeneous boundary condition in u and v. Besides that, that the PSE solver is computationally less expensive and the only outcome of the solver is the TS wave. In LST, a spectrum of eigenmodes comes out of the solver and the TS eigenmode must be chosen using a filtering algorithm. This additional step adds complexity and since the algorithm lacks robustness for weak TS waves, this could lead to noise in the stability diagrams. This noise can be seen in the top right corner of figure 1.2. This is not a problem with the PSE solver, however, there are also some downsides to the use of PSE. The main disadvantage is that the PSE solver is unstable for small step sizes. This is more elaborately discussed in section 3.1.

1.1.2 Metamaterials

Metamaterials are discrete geometrical structures. This enables the ability to manipulate waves unnaturally on macroscopic scale. This is regularly not dependent on the chemical composition of the material, but on its internal or external geometry. The abilities of these metamaterials to manipulate waves are unconventional compared to normal materials. Therefore, this opens a broad horizon of new possibilities. Since a TS instability behaves like a convective wave in a boundary layer as shown in section 1.1.1, metamaterials can possibly be used in the application of boundary layer instability control. In this section, a general introduction to metamaterials is given. A more thorough review of different kinds and applications of metamaterials is given in section 2.2.

The first metamaterials found in literature were based on electromagnetic waves. For these electromagnetic waves through a medium, for example light travelling through glass, the wavelength is much larger than the atoms that build up the glass. The effect that the medium has on the wave can go down to the interaction on micro level, but the general wave interaction properties are caught in two macroscopic parameters: electric permittivity (ϵ) and magnetic permeability (μ) [18]. For most of the natural materials, both of these parameters are positive. For some specific semiconductors or ferrites, one of these parameters become negative. However, in natural materials, a simultaneously negative permittivity and permeability is not found. This is summarised in figure 1.5a.

Preliminary to possibility to produce these double negative metamaterials, there was already a theoretical investigation of their behaviour performed by Veselago, which was presented in 1968 [19]. The main conclusions were that in materials with a simultaneously negative ϵ and μ, the Poynting vector is antiparallel to the wave vector and that the phase refractive index, described in equation 1.11, must be negative to conserve causality [4]. This negative refractive index causes an unnatural wave propagation at the interaction between a 'normal' material/medium and a double negative metamaterial. The incoming wave bends to the other side of the surface normal and the wave vector is in opposite direction of the group velocity of the ray [18].

$$n = \sqrt{|\epsilon_r||\mu_r|} \tag{1.11}$$

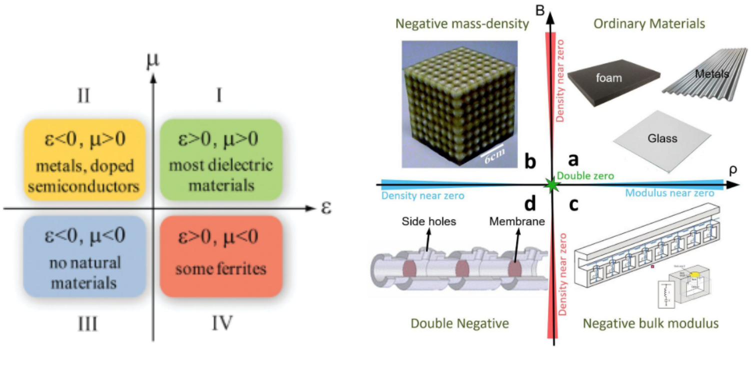

(a) Taken from [4]

(b) Taken from [20]

Figure 1.5: Material parameter space characterised by (a) electric permittivity (ϵ) and magnetic permeability (μ) and (b) effective mass/density (ρ_{eff}) and bulk modulus (B)

Metamaterials generally consist of a structure in which a specific arrangement of small resonant units can be found. These meta-atoms are usually smaller than a wavelength. These units can have their resonance in electromagnetics, but an analogy can be found in acoustics. Materials can consist of acoustic meta-atoms in a particular lattice to get acoustic metamaterials. The global parameters that describe an acoustic wave propagating through a medium are the effective mass/density and the bulk modulus, denoted with ρ_{eff} and B respectively. This can be derived from equation 1.12, which describes the behaviour of acoustic waves through a linear fluid [20]. A similar material parameter space characterisation as for electromagnetic metamaterials can be made for these metamaterials, this is given in figure 1.5b.

$$\nabla^2 P(r) - \frac{\rho_{\text{eff}}}{B}\frac{\partial^2 P(r)}{\partial t^2} = 0 \tag{1.12}$$

In the equation, P represents the pressure.
Furthermore, the effective density and bulk modulus determine the phase velocity of the acoustic wave: $v_{\text{ph}} = \sqrt{B/\rho_{\text{eff}}}$

In contradiction with electromagnetic metamaterials, materials with only one negative characterising parameter cannot be found in nature [21]. Acoustic metamaterials with a negative effective mass/density usually have resonant meta-atoms made of mass-membrane or mass-in-mass systems. A negative bulk modulus on the other hand, is usually achieved using Helmholtz resonators as resonant units. A combination of both can cause double negativity, where the effective mass/density and bulk modulus are simultaneously negative. This can also be reached using more complex concepts. Applications of metamaterials in acoustics are given in section 2.2.

1.2 PROBLEM FORMULATION

Acoustic metamaterials have shown their functionality in manipulating acoustic waves. In this research, the application of these metamaterials to boundary layer instability control is investigated. The main research question can therefore be stated:

Are acoustic metamaterials suitable for attenuating Tollmien-Schlichting waves to delay boundary layer transition in subsonic conditions?

Several sub-questions need to be answered before conclusions can be drawn about the primary research question. The first set of sub-questions can be answered based on a literature study to boundary layer stability, flow control and (acoustic) metamaterials.

1 *What properties of a wall controller are necessary to attenuate the most dominant mode in the path to transition?*
First, it is needed to find out what the frequency is of the most unstable and dominant TS wave. This can be done using stability diagrams that can be created with different stability theories. Then, other ways of flow control need to be evaluated to investigate what properties the wall controller needs to have in order to get TS wave attenuation in a particular frequency range.

2 *What acoustic metamaterial is most suitable to suppress Tollmien-Schlichting waves in an experimental setup?*
Since the performance of the acoustic metamaterial will be evaluated experimentally in a wind tunnel, the metamaterial should be designed and produced with limited resources. Therefore, acoustic metamaterial concepts should be

mapped and for each concept the expected effect and feasibility need to be evaluated.

Once an answer is found to these questions, a more clear image can be created on what the eventual experiment will look like. The following questions will then arise.

3 *How can a wind tunnel experiment be designed to investigate the influence of an acoustic metamaterial to a TS wave?*
To design the experiment, the metamaterial needs to be designed and produced. This can be done with help of numerical design tools that calculate the boundary layer stability like LST or PSE. Moreover, linearised Navier-Stokes simulations can be used to predict the experimental outcome.

4 *What flow measurement technique is needed to evaluate the interaction between the TS wave and the acoustic metamaterial?*
The kind of flow measurement technique used in the experiment needs to give the opportunity to evaluate the TS wave behaviour when passing the acoustic metamaterial.

5 *What behaviour of the acoustic metamaterial is needed to achieve TS wave damping?*
Using numerical simulations, it is possible to find out what the desired behaviour of the acoustic metamaterial should be in order to suppress TS waves. This behaviour can include amplitude/phase relations similar to acoustic impedance matching.

When the experiment is designed, it needs to be performed. The data from this experiment need to be post-processed in order to draw conclusions. The last sub-questions arise.

6 *Do the experimental results match with the prediction made by numerical models and simulations?*
A hypothesis of the influence of the acoustic metamaterial can be made using numerical simulations. It can be investigated to what extend this matches the experimental results to indicate the reliability and accuracy of these numerical tools.

7 *To what extent could the interaction between the acoustic metamaterial and TS wave be captured in a physical framework?*
The physical mechanisms that play a role in the interaction between the acoustic metamaterial and the boundary layer instabilities should be identified in order to fully understand the behaviour.

Some of the sub-questions will be answered during the research to move forward to the wind tunnel experiment. After the wind tunnel test is conducted, the results of the experiment can be used to answer the latter questions together with any numerical results. Eventually, an initial conclusion can be drawn on the feasibility to use acoustic metamaterials in boundary layer instability control.

Together with the research question, a research objective can be stated that serves as the goal of the study:

The research objective is to achieve experimental, numerical and theoretical evidence on how the stability of a subsonic laminar boundary layer is influenced by an acoustic metamaterial in a test case of a flat plate boundary layer.

To reach this goal, a design of the experiment needs to be made first. This includes determination of flow parameters and a physical design of the acoustic metamaterial. This will all be based on preliminary numerical simulations that predict the outcome of the experiment and available information from literature. With the data from the right flow measurement techniques, the information should be gathered to answer the main research question.

In the following chapters, the research questions will be answered. In order to do so, the state of the art will be analysed in chapter 2. Next, the methods to answer the research questions are given in chapter 3. In the following chapter (chapter 4), the findings are given and directly discussed per subject. Finally, the main conclusions are stated in chapter 5. This chapter will also include recommendations for further research to this subject.

2 STATE OF THE ART

In order to design the experimental setup and to investigate the possibilities in the field of metamaterials and flow control, the state of the art needs to be identified. In this chapter, related studies will be described in four different categories. First, methods of boundary layer instability control will be given in section 2.1. Secondly, some applications and concepts of acoustic metamaterials are described in section 2.2. Next, the most closely related work will be given in section 2.3 in which studies are presented that use metamaterial concepts to control flow. Eventually, in section 2.4, other studies are discussed that deal with the interaction between Helmholtz resonators and boundary layer flows.

2.1 BOUNDARY LAYER STABILITY CONTROL

The assumed path to transition in this study is path "A" from figure 1.1a. Receptivity initiates the growth of wave-like modes until they eventually break down into turbulence. Transition delay can be achieved if the primary modes, like the TS wave, can be suppressed. In order to prevent these primary modes from growing to lead to transition, mainly actively actuated methods are used. In these methods, energy is used to suppress the instability. The net gain is therefore the difference between the energy saved due to the drag reduction and the energy used to accomplish this.

The approaches used in these methods can be divided into two categories. In the first category, a passive, steady effect is created that influences the TS wave growth via the external flow conditions [22] [23]. The second category involves the active use of information of the TS wave to control the wall actuator accordingly [24] [25] [26]. The acoustic metamaterial concept in boundary layer instability control is assumed to actively respond to the passing TS wave without external actuation or energy input. In this section, the desired wall controller properties are investigated that are desired for the eventual metamaterial system.

One of the first methods used for transition delay is suction through the wall. This was described by Reynolds in 1986 in an experimental study [22]. With a vibrating ribbon, a specific TS wave was initiated near the leading edge of the flat plate. Either continuous or discrete suction strips were attached to the wall in different experiments and it was shown that the growth of the TS waves was reduced. The continuous and discrete suction strips have similar effects and the effect is strengthened if the strips are applied close to the point of neutral stability rather than at the point of maximum growth rate.

A theoretical analysis on the effect of wall cooling to the growth of boundary layer disturbances was performed by Malik [23]. For supersonic and hypersonic Mach numbers, the growth of the first instability mode could be damped by cooling the wall. The second mode however, can be destabilised due to this cooling and can become the dominant mode for transition, but the frequency of the unstable band increases. Therefore, a fixed second mode instability frequency can be damped due to cooling, but the disturbance that is most amplified shifts to a higher frequency. So, if the incoming flow is free of high frequency disturbances, wall cooling can also stabilise the second mode and with that the whole boundary layer.

Besides steady suction through the wall, there are also methods that make use of periodic suction and blowing. This method was opted by Biringen [27]. The paper describes a numerical study based on two and three dimensional Navier-Stokes simulations to the influence of periodic suction and blowing to TS waves in a channel flow. Optimal damping of these TS waves is achieved if the boundary conditions form a wave that has over twice the amplitude of the primary TS wave and if these waves are induced completely out of phase.
A similar control method was used by Liepmann & Nosenchuck [28]. They used local heating elements on a flat plate model. It was shown that the periodic heating of flush-mounted heating elements could introduce a TS wave instability in the boundary layer. A similar heating element was used downstream to attenuate the TS waves by inducing a second instability out-of-phase with the passing TS wave.

If a vibrating ribbon can be used to initiate a boundary layer instability, it might also be used to cancel them out. This was the idea behind the study by Thomas [24]. The main principle of this study is to impose a similar wave as the TS wave but with a different phase such that a superposition leads to cancellation. A wind tunnel experiment was used with a flat plate model of which a schematic is given in figure 2.1a. In a natural situation, transition would not take place over the length of the flat plate model. By initiating an instability with the most upstream vibrating ribbon, the amplitude of the waves inside the boundary layer increases, so transition would take place upstream of the trailing edge of the plate. An optimal amplitude/phase relation was found for the vibration of the second ribbon to cancel out the TS waves. This was investigated by measuring the velocity fluctuation downstream of both ribbons. The frequency spectrum of this velocity fluctuation is given in figure 2.1b. Adding the second ribbon with the optimal control conditions attenuates the whole spectrum, but it does not completely match the baseline spectrum. This means that TS wave suppression by wave superposition is successful for damping a specific TS wave frequency, but it will never bring the boundary layer back to its natural state [24].

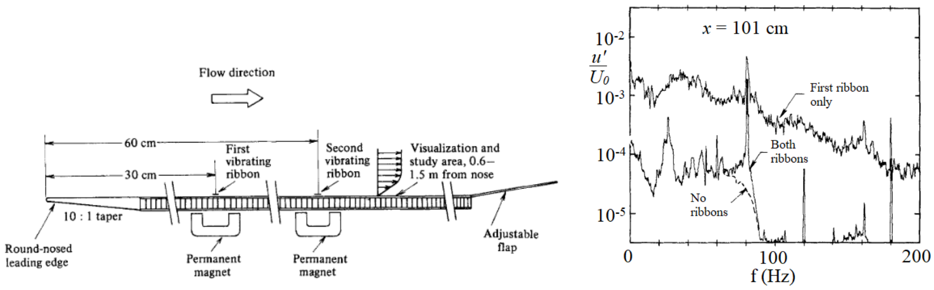

(a) Schematic of the test setup with two vibrating ribbons

(b) Velocity fluctuation spectrum evaluated downstream of second vibrating ribbon

Figure 2.1: Taken from [24]

Another way of active transition delay is by using dielectric barrier discharge (DBD) plasma actuators. These plasma actuators ionise the air locally and the interaction between the ionised air and the neutral air cause a momentum transfer that adds a body force to the boundary layer [29]. The strength of this body force is dependent on the AC voltage amplitude and the carrier frequency. A schematic of a DBD plasma actuator is given in figure 2.2.

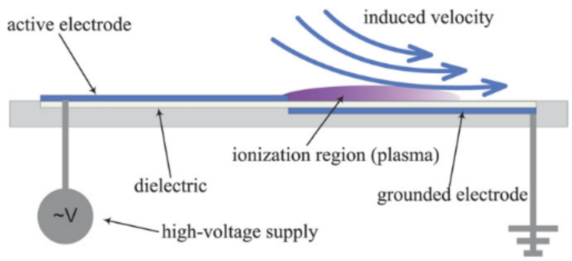

Figure 2.2: Schematic of a DBD plasma actuator operating in a flow [29]

Because the plasma actuator induces a small body force in the boundary layer, it can be used to control the flow and more specifically to control TS waves. In the study by Kotsonis et al. [25], experiments were conducted on the influence of a control system using plasma actuators to the development of TS waves on a NACA 0012 airfoil wing model. Using a closed-loop control system, an attenuation of 50% of the TS wave amplitude was reached with specific flow conditions. Also for other conditions, wave suppression was also found.

A similar setup was used in the research conducted by Tol et al. [26]. With a similar plasma actuator and a point wall measurement both upsteam and downstream of the actuator, an optimal control system was designed based on a combination of feedback and feedforward techniques. This study also shows a damping of TS waves with respect to a baseline case without control. This is given in figure 2.3a, which shows the RMS (Root Mean Square) of the velocity fluctuation of the TS wave over the streamwise distance from the leading edge based on a numerical simulation. It can clearly be seen that the controlled cases end up with a lower RMS downstream of the plasma actuator. The LQG (Linear Quadratic Gaussian) control methods perform superior in attenuating the TS wave with respect to the open loop controllers.

The simulations show good attenuation of the TS waves with the goal to delay boundary layer transition. This was also evaluated experimentally. In figure 2.3b, a power spectral density (PSD) plot of the downstream microphone measurement is given. In this PSD, the amplitudes corresponding to the different frequencies are given for the different control methods. In accordance with the simulation, all control methods reduce the TS wave amplitude in comparison with the uncontrolled baseline case. This attenuation is achieved for all measured frequencies.

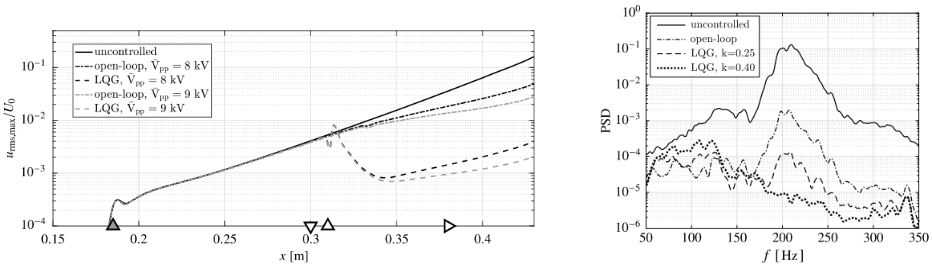

(a) RMS of TS-wave velocity fluctuation with different control methods, at the x-axis, the locations of the source (dark Δ), sensor (∇), actuator(Δ) and control objective (▷) are highlighted

(b) PSD of the downstream sensor signal

Figure 2.3: Taken from [26]

The body force that is exerted by the plasma actuator used in the study by Tol et al. [26] is given in figure 2.4. It can be seen in the figure that directly above the plasma actuator, there is a force field acting primarily along the horizontal direction. The conclusion can be drawn that this forcing near the wall can attenuate the TS wave amplitude at an appropriate phase. This indicates that the wall controller property that is desired for the acoustic metamaterial concept in this study is dependent on the phase relation between the TS wave and the actuation from the metamaterial. In this way, cancellation by superposition can be expected in accordance with the studies by Biringen [27], Liepmann & Nosenchuck [28] and Thomas [24].

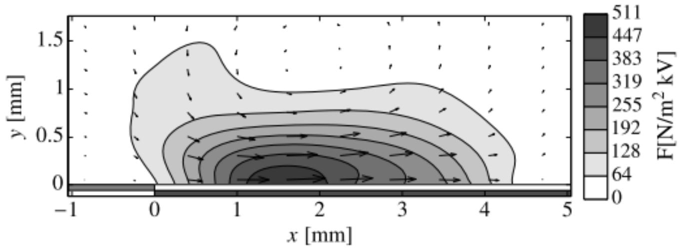

Figure 2.4: 2D plot of the body force exerted by the plasma actuator [26]

2.2 APPLICATIONS OF ACOUSTIC METAMATERIALS

TS waves in a laminar boundary layer behave like convective waves. From the introductory chapter, it is known that metamaterials have the ability to unnaturally manipulate waves. This manipulation is based on the controlling properties of the metamaterial with respect to the nature of the wave. In the previous section, the wall controller properties that are desired for a metamaterial in boundary layer instability control are discussed. In order to investigate what concept is most suitable to use for this study, an inventarisation of the possibly applicable acoustic metamaterials is made in this section.

As mentioned earlier in the introductory chapter, acoustic metamaterials either have a negative effective mass/density or a negative bulk modulus. These parameters can also be simultaneously negative, this would make it a double negative acoustic metamaterial. Concepts and applications corresponding to these three different kinds of acoustic metamaterials are presented here.

2.2.1 Negative effective mass/density

The first category that will be discussed is the acoustic metamaterial with a negative effective mass/density. In general there are two methods of reaching this property: with a mass-membrane system or with a mass-in-mass system. Both of these methods make use of the resonance of the meta-atoms in the system.

In the paper by Yang et al. [7], a mass-membrane type acoustic metamaterial is introduced. A mass-membrane unit consists of a circular membrane, which is made of a thin and lightweight material, and a mass in its centre. Because of the elastic properties of the membrane, the system can vibrate at low frequencies. Depending on the mass in the centre and the stiffness of the membrane, the system will start resonating at a specific frequency. In figure 2.5, the amplitude of the transmission through the membrane and the corresponding phase are given. It can be seen that there are peaks in transmission at 146 and 974 Hz. There is also a dip in the figure, at 272 Hz. At this dip, the transmission of the incoming acoustic wave is almost zero. This means that at this frequency, the acoustic wave is almost fully damped by the mass-membrane system.

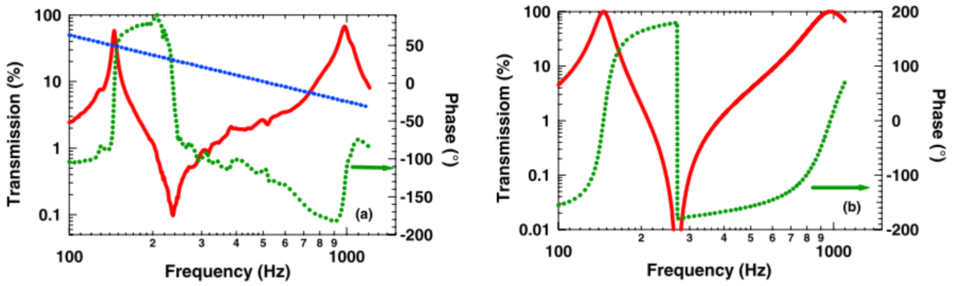

(a) Experimental

(b) Theoretical

Figure 2.5: Transmission amplitude (red) and phase (green) for an acoustic wave through a specific mass-membrane system, in blue the expected transmission amplitude according to the mass density law [7]

From figure 2.5, the conclusion can be drawn that the transmission is accurately predicted by the theory. The phases are less adequately represented. It can be seen from figure 2.5a that the mass-membrane system damps a broaden range of frequencies between the two eigenfrequencies. A peak in the transmission is found when the phase crosses the zero degree phase line, according to figure 2.5b. The dip occurs when the phase crosses ± 180 degrees. The drawn conclusion is that wave damping occurs between the eigenmodes of the mass-membrane system given in figure 2.6a. These eigenmodes are given in figure 2.6b, which is taken from a similar experiment conducted by Ma et al. [30].

The effective mass of the mass-membrane system is determined using equation 2.1. In which $\langle . \rangle$ denotes the volume average of the whole structure. The stress in the membrane is represented by σ_{zz} while the acceleration normal to the membrane plane is given by a_z.

$$\rho_{eff} = \frac{\langle \sigma_{zz} \rangle}{\langle a_z \rangle} \tag{2.1}$$

The effective mass becomes negative close to the dip frequency and it turns back to positive again at the dip frequency. A negative effective mass physically implies that forcing to one side leads to acceleration to the opposite side. For higher frequencies, the effective mass approaches the actual value of the system [7].

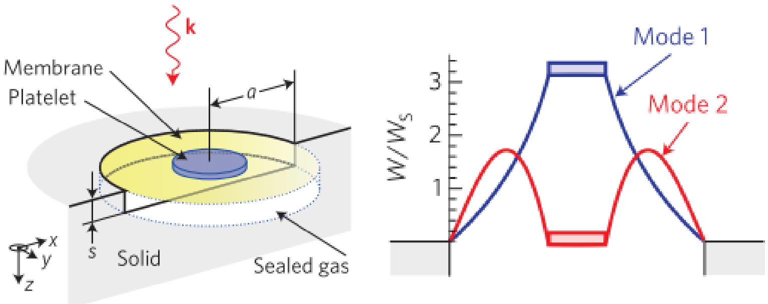

(a) Mass-membrane unit

(b) First two eigenmode of a mass-membrane system

Figure 2.6: Taken from [30]

In the study by Ma et al. [30], the dip in transmission is denoted as the hybrid resonance absorption peak, since the acoustic energy is absorbed at that frequency. The mode corresponding to this hybrid resonant absorption peak is given in figure 2.7. It can be seen that the membrane and mass vibrate out of phase. At this frequency, the impedance of the surface with the mass-membrane system and the airborne sound match. There is no reflected wave generated.

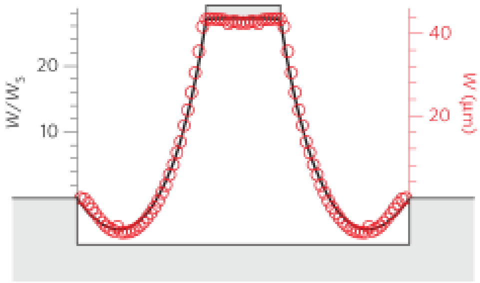

Figure 2.7: Normal displacement (W/W_s) of the mass-membrane system at the hybrid resonant absorption peak [30]

The system in the paper by Ma et al. [30] does not only damp the sound wave, but it also uses the mass-membrane system as energy harvester. A magnet is used as the mass attached to the membrane and another magnet is mounted to the membrane holder. The magnet on the membrane starts vibrating and due to their relative movement, energy can be harvested.

In the studies mentioned above, the mass was a circular disk. Changing the shape of this mass, can lead to some advantages. This was shown by Lu et al. [31] in 2019. The mass was chosen to be an eccentric split ring (figure 2.8). Using this geometry, the amount of parameters that define the system's performance increases.
A downside of using the simple mass-membrane system is that the sound absorption only peaks at a narrow band of frequencies. By using the split ring mass, the membrane is also 'split' into multiple sub-membranes. This increases the amount of (anti) resonances in the system and if the right geometry is chosen, the frequency band of high absorption can be increased. In this way, the metamaterial can be used in a broader range of frequencies to attenuate incoming sound waves.

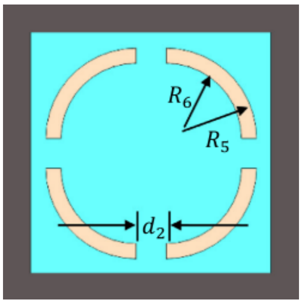

Figure 2.8: Membrane with eccentric split ring mass [31]

Another method of using the resonance of a mass-membrane coupling is described in the paper by Lee et al. [32]. In this study, the sound absorption properties of a series of unit cells with a membrane are investigated. The unit cell geometry is given in figure 2.9a, a schematic of the experiment with a series of unit cells is given in figure 2.9b. The mass that is used in this concept is the mass of air between two membranes. With this mass-membrane system, sound with a frequency lower than a certain cut-off frequency can be completely damped. In this frequency region the effective mass, defined as in equation 2.2, is negative. Therefore, the acceleration is not in the same direction as the force.

$$\rho_{eff} \equiv \frac{-\partial p/\partial z}{\partial^2 q/\partial t^2} \tag{2.2}$$

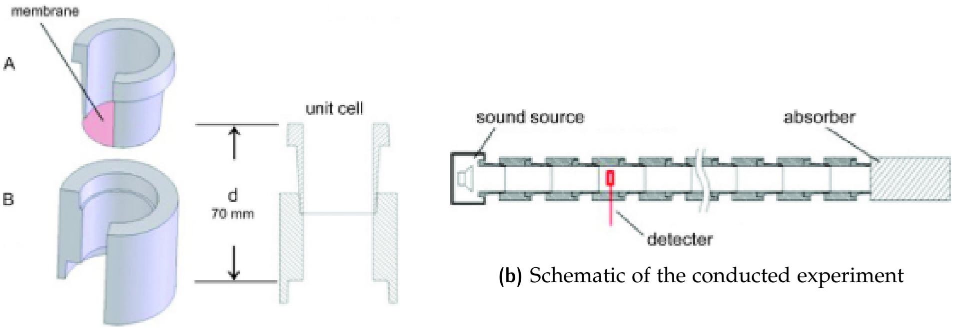

(a) Geometry of a unit cell

(b) Schematic of the conducted experiment

Figure 2.9: Taken from [32]

Besides the mass-membrane configuration, an acoustic metamaterial with negative effective mass/density can also be obtained with mass-in-mass systems. A theoretical example of this concept is given in the paper by Huang and Sun [33]. A study was conducted to the mass-in-mass structure shown in figure 2.10a. This structure consists of an infinitely long series of unit cells. The only parameters that can be varied are the ratios between the spring stiffnesses and the ratios between the masses. The result of the calculations in the study is that there are band gaps in the dispersion curve (figure 2.10b) corresponding to the system. In these band gaps, the effective mass of the system becomes negative. In the study, a micro-structure model is compared to an exact solution.

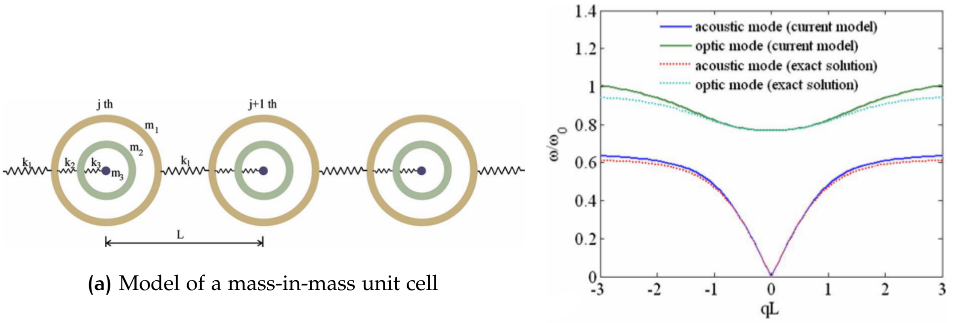

(a) Model of a mass-in-mass unit cell

(b) Dispersion curve with a band gap of about $0.61 \leq \omega/\omega_0 \leq 0.77$ and $\omega/\omega_0 \geq 1$

Figure 2.10: Taken from [33]

With some applications of this first branch of acoustic metamaterials discussed, some conclusions can be drawn on their applicability to boundary layer instability control. Suppression of sound wave transmission through the material was demonstrated, but for the instability control application, waves that are passing over a surface need to be attenuated. Therefore, the only concepts that remain from this section are the mass-membrane systems. A lattice of mass-membrane meta-atoms can form a metasurface that could possibly damp a passing wave. However, tensioning a membrane exactly up to the right specifications can be challenging for experimental applications. Also, the moving mass might also increase the surface roughness locally. These are some disadvantages of using this type of acoustic metamaterial concepts in the current study, but in general, there is some potential for mass-membrane systems in boundary layer instability control.

2.2.2 Negative bulk modulus

Next to the the effective mass (ρ_{eff}), there is another important parameter in the propagation of acoustic waves that is present in equation 1.12, namely the bulk modulus (B). The acoustic metamaterials that are presented in this section will have a negative bulk modulus in certain frequency bands. Most of the metamaterials in this quadrant of the spectrum make use of a series of Helmholtz Resonators (HR). A HR consists of a cavity with a relatively large volume and a small throat. A schematic of a HR is given in figure 2.11a.

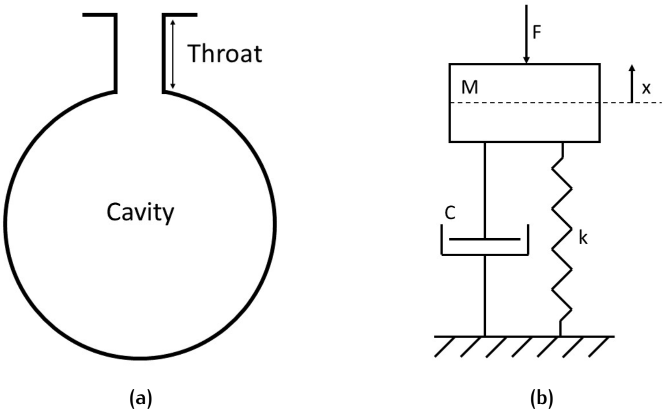

Figure 2.11: Schematic of (a) a Helmholtz resonator and (b) a mass-spring-damper system

A HR is driven by a fluctuating incoming (acoustic) pressure. For a specific frequency, the pressure fluctuation is amplified, this is called the resonant frequency (f_{res}). There is a clear analogy between a HR and a mass-spring-damper system 2.11b. The resonant frequency and other properties can be derived from this analogy. The cavity volume serves as the spring stiffness of the system. The mass term represents the mass of air oscillating inside the throat of the resonator. The total mass however, is subject to a correction factor to account for the air just above and beneath the throat. The damping term is equivalent to the flow resistance through the throat. Since the resonant frequency of a mass-spring-damper system is equal to the square root of the spring stiffness divided by the mass, the resonant frequency of a HR can be calculated using equation 2.3. The driven part of the resonator is the mass inside the throat, this mass oscillates dependent on the forcing and resonant behaviour. This is equivalent to the movement of the mass in the mass-spring-damper system.

$$f_{res} = \frac{c}{2\pi}\sqrt{\frac{S}{VL'}} \tag{2.3}$$

In the equation, c represents the speed of sound. S and V represent the cross sectional area of the throat and the volume of the cavity respectively. L' represents the corrected throat length.

The first paper that shows an acoustic metamaterial with negative bulk modulus was written by Fang et al. [6] in 2006. This paper addresses a metamaterial that is designed to manipulate ultrasound waves. The experimental setup used in this paper consists of a waveguide with an array of HRs connected to it. The medium that was used is water. A schematic of the setup is given in figure 2.12a. With hydrophones, the pressure fluctuations are measured at the beginning and at the end of the channel.

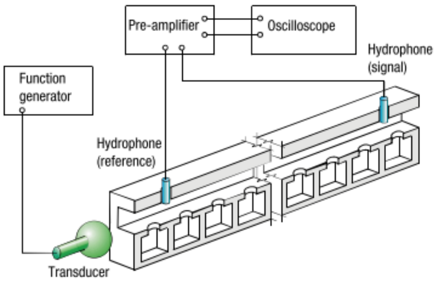

(a) Schematic of the test setup

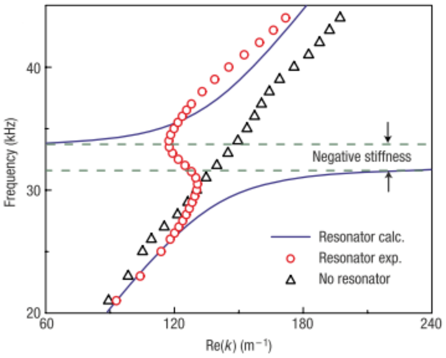

(b) Dispersion curve of the metamaterial

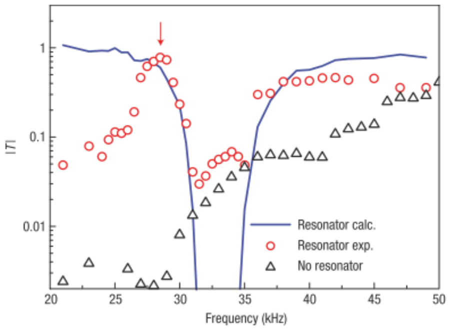

(c) Transmittance amplitude through the channel referenced to the upstream hydrophone

Figure 2.12: Taken from [6]

With this setup, a negative group delay time is measured for certain frequencies. A negative group time delay means that a sound pulse propagating through this channel emerges earlier downstream than if it had passed through a channel without resonators. The peak of the sound pulse seems to leave the duct before it entered it [6]. This is a clear indication of a negative bulk modulus. This behaviour is mostly seen near the designed resonant frequency ($f_{\text{res}} = 32.5$ kHz). A band gap can be found in the dispersion curve that is given in figure 2.12b between 31 and 35 kHz, for the calculated behaviour. The transmission of sound is given in figure 2.12c. This shows that according to the calculations, there is a frequency gap in which sound is not transmitted, the same as the band gap from figure 2.12b. The experiments, however, show some transmittance in this gap, but the trend of the calculated behaviour is followed. There is also a peak in transmittance, just before the gap. This peak is explained as a Fano-like transmittance peak [34] [35] because a portion of the wave can travel in a non-resonant path [6]. In figure 2.12c, the 'no resonator' data is also given. They show minor transmittance, especially for the lower tested frequencies. This means that the array of HRs can manipulate the ultrasound waves in different ways depending on their frequencies.

After this first step into acoustic metamaterials with a negative bulk modulus, further steps in developing a model to describe and predict this behaviour were taken in the paper by Wang et al. [8]. The study introduces a theoretical model to describe the influence of an array of HRs to the transmittance of an acoustic wave through a waveguide. A schematic is given in figure 2.13a, in which the geometrical parameters of influence are highlighted. With the theoretical model, the frequency gaps in transmittance can be calculated. They show multiple gaps over a wide spectrum of frequencies. The widest gap (in figure 2.13b) has the lowest frequency and this gap is caused by resonance. The frequency of the incoming sound wave coincides with the eigenfrequency of the resonator and blocks the sound wave from transmitting forward. The other gaps, at higher frequencies, are Bragg gaps [36]. These are visible if the periodic spacing between the resonators is half a wavelength or an integer plus $\lambda/2$ of the incoming sound wave [8]. In this Bragg gaps, superposition of scattered sound leads to a destructive effect on these waves.

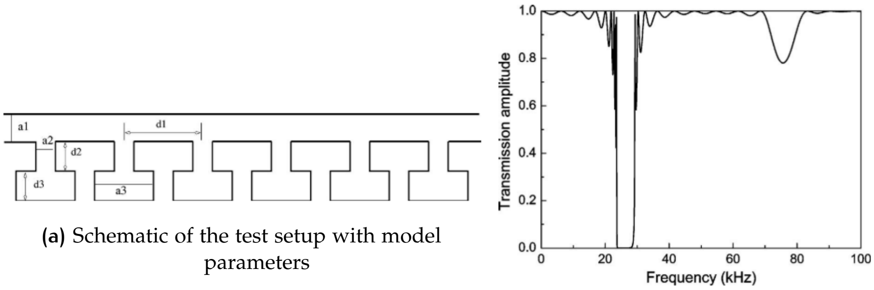

(a) Schematic of the test setup with model parameters

(b) Transmittance calculated with the theoretical model for a specific resonator array

Figure 2.13: Taken from [8]

The theoretical model by Wang et al. [8] was tested experimentally by Fey & Robertson [11]. In their study, an experiment is described in which a single resonator is connected to a waveguide. The influence of this single resonator to the transmittance is measured with the setup given in figure 2.14a. Since the model by Wang et al. [8] could also be used for a single resonator instead of an array, the model and experimental results were compared. In figures 2.14b and 2.14c, the experimental and theoretical results are given. They show good agreement with each other. Multiple transmittance gaps are present, a wider one at the lowest frequency and multiple sharp ones at higher frequencies. The first one is caused by the system's resonance, the other ones are standing-wave modes along the length of the cavity [11]. It can also be shown that the group delay, calculated with equation 2.4, can become negative in the band gap. In this region, the bulk modulus is therefore negative.

$$\tau_g = -\frac{\partial \phi}{\partial \omega} \tag{2.4}$$

Instead of Helmholtz resonators, cylindrical boreholes in a 2D lattice are used to create a band gap in transmittance in the study by García-Chocano et al. [9]. In this quasi-2D metamaterial, that is schematically visualised in figure 2.15a, it is possible to create a frequency band in which the sound is damped based on the geometrical parameters of the boreholes and the lattice. In this study, both experiments and simulations with the Finite Element Method (FEM) are used and they show good agreement. In figure 2.15b, the pressure amplitudes are given in a contour plot from a top view. The top and bottom frequency (822 Hz and 1265.5 Hz) are outside the band gap in which the bulk modulus is negative. The middle frequency (910 Hz) is inside this gap and shows sound wave suppression from left to right. Because boreholes are used instead of HRs, losses are reduced. This concept can therefore be used to filter the sound propagating through the waveguide with high efficiency [9].

In order to reach a well absorbing metasurface, it is important that the impedance of the surface matches with the impedance of acoustic waves in the medium [10]. The impedance of acoustic waves in air can be calculated with $Z = \langle p \rangle / \langle v_{\perp} \rangle$, so the average pressure above the surface divided by the average velocity normal to

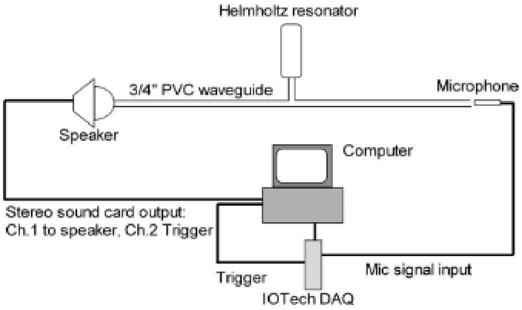

(a) Schematic of the test setup

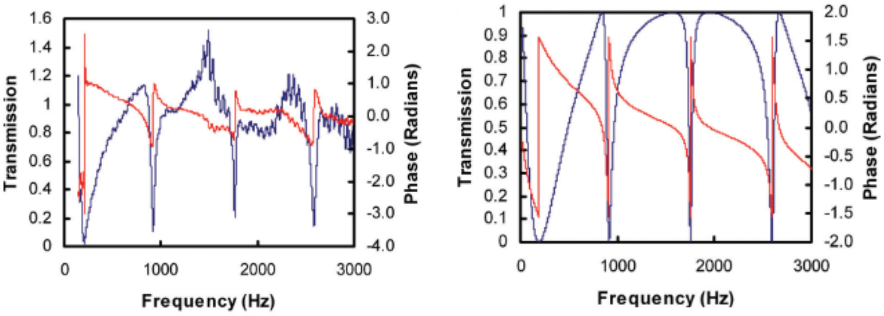

(b) Transmittance calculated from experimental data

(c) Transmittance calculated by model from Wang et al. [8]

Figure 2.14: Taken from [11]

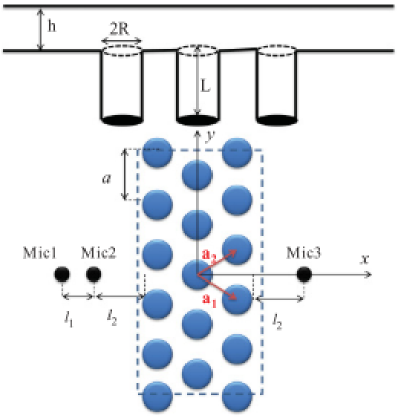

(a) Schematic of the test setup with model parameters

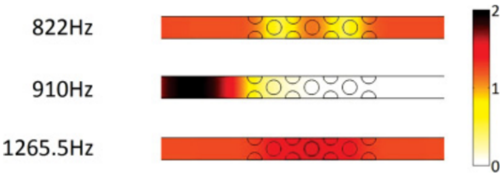

(b) Top view contour plot of acoustic pressure amplitude propagating through the waveguide

Figure 2.15: Taken from [9]

the surface. This impedance is a complex parameter. A relative impedance (Z_r) can be calculated by normalisation with $Z_{air} = \rho_{air}c_{air}$. Full absorption of incident sound waves is reached when $\Re(Z_r) = 1$ and ($\Im(Z_r) = 0$). This was also shown experimentally in the study by Li et al. [10]. To get to this impedance matching surface, an array of HRs with different dimensions and therefore different resonating properties. An acoustic energy absorption of 99% was achieved at a frequency around 500 Hz. The absorption bandwidth of 50% was 140 Hz, so for these low frequencies, sound was damped in a broaden region.

Multiple ways are described to get a frequency band with a negative bulk modulus. It was shown that the band width and maximum absorption frequency is only dependent on the geometry of the metamaterial. The properties of the metamaterial

can therefore change directly if the geometry can change by itself. This can for example be accomplished by having a pneumatic actuator that changes the size of the cavity, This was researched by Hedayati & Lakshmanan [37], they were able to shift and increase the band gap using this technique.
Another way of changing the behaviour of the metamaterial is changing the temperature of the medium. This was done by Xia et al. [38] in 2016. A different temperature changes the density and the speed of sound. This can influence the transmittance through the metamaterial. In their experiment, in which water was used as working fluid, the negative effective bulk modulus and local resonant band gap could be tuned about 11%.

Similar to the acoustic metamaterial concepts discussed in section 2.2.1, the ones discussed here are also able to inhibit sound transmission. A difference is that most numerical and experimental setups are based on sound propagation through a waveguide instead of through the acoustic metamaterial itself. This is more closely related to the situation of wave-like instabilities propagating inside a boundary layer. The behaviour of a system with Helmholtz resonators as meta-atoms is only dependent on geometrical parameters. This branch of acoustic metamaterials is therefore feasible to work with in an experimental setting as the current study requires.

2.2.3 Double negative

The double negative quadrant in figure 1.5a for electromagnetic metamaterials is the part where its apparent properties exhibit unnatural behaviour. There, it was the goal to find a material that has this negative permittivity and permeability simultaneously. For acoustic metamaterials (figure 1.5b), the double negative properties can be reached by combining concepts from the negative mass/density and negative bulk modulus quadrant in one, new concept. This combining of methods was suggested by the earlier mentioned paper of García-Chocano et al. [9]. A membrane can be added to the bottom of the boreholes to get a double negative metamaterial.

Earlier, in 2004, Li & Chan [39] already came up with a double negative acoustic metamaterial. Physically this means that the metamaterial shows expansion upon compression (negative bulk modulus) and movement to the left when being pushed to the right (negative mass/density) at the same time at certain frequencies. This odd behaviour could mathematically be possible by dispersing soft rubber in water. For electromagnetic metamaterials, negative permittivity and negative permeability could be reached via two distinct sources of resonance. In acoustics, both negative effective density and negative bulk modulus originate from the same resonance source. The only distinction that can be made is that a negative effective density comes from dipolar resonances and a negative bulk modulus comes from monopolar resonances [39]. With the double negative acoustic metamaterial, a negative acoustic refractive index could be reached, similar to the electromagnetic refractive index.

In 2019, a theoretical method was developed and described by Hu et al. [40] on the concept proposed by García-Chocano et al. [9]. A coupled membrane HR system was developed where the normally rigid bottom of the HR is replaced by a membrane. This double system can have multiple resonances in the low frequency range. These natural frequencies of the coupled system are different from the natural frequencies of the systems independently. In the study, multiple lumped parameter models are constructed and compared with each other and a COMSOL Multiphysics simulation that serves as benchmark. The main outcome is that multiple band gaps occur in the dispersion curve with this coupled system in which sound is well attenuated.

In a follow-up study by the same group of researchers [41], a central mass was added to the the membrane bottom of the HR. With this, the main concepts of negative effective mass/density and negative bulk modulus acoustic metamaterials are combined. An array of these coupled systems is schematically visualised in figure 2.16. Similarly to the configuration without masses attached to the membranes, multiple band gaps were found for this concept. Although negative mass/density and negative bulk modulus concepts were coupled, no indication of double negativity was given in the paper.

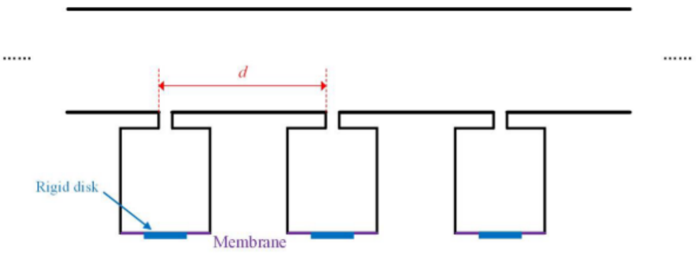

Figure 2.16: Schematic of the array of mass-membrane coupled Helmholtz resonators [40]

Double negativity was found in a study by Yang et al. [42] in which two membrane-mass systems were combined. A schematic of the combined system is given in figure 2.17a. Because of the symmetry in the system, it is able to generate both monopolar and dipolar resonances. These can be tuned separately to obtain a frequency band where both resonances occur simultaneously and cause double negativity. In the study, the double negativity is found between the second and third eigenfrequency of the system. In the frequency spectrum, the bulk modulus and effective density both instantly become negative after the second eigenfrequency as can be seen in figure 2.17b.

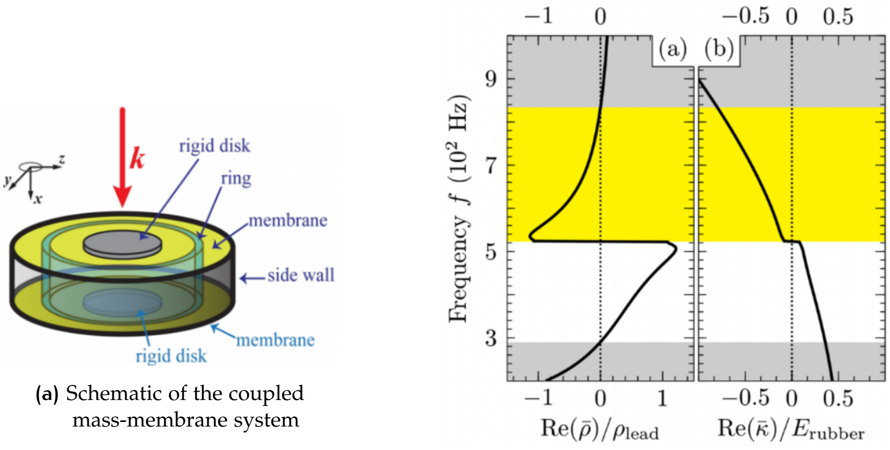

(a) Schematic of the coupled mass-membrane system

(b) Relative effective mass/density and bulk modulus, the grey areas represent band gaps and the yellow area is the double negativity band

Figure 2.17: Taken from [42]

The acoustic metamaterial concepts mentioned in this section are in general more complex than the ones discussed in sections 2.2.1 and 2.2.2. Some extraordinary behaviour can be obtained with the double negative acoustic metamaterials, but for this study it is more convenient to stay with the simpler concepts to evaluate their interaction with TS waves. The metamaterial concept that is chosen for this study is based on the system of Helmholtz resonators. In terms of feasibility to use experimentally, this concept stands out in comparison with the mass-membrane system. The behaviour of a system of Helmholtz resonators is only dependent on geometrical parameters. Moreover, this concept was tested successfully in a waveguide setup which seems closely related to the situation of wave-like instabilities travelling inside a boundary layer.

2.3 METAMATERIALS AND FLOW CONTROL

In previous sections, some concepts for boundary layer instability control and acoustic metamaterials are described. In this section, examples will be given that make use of metamaterial concepts in the flow control application. These are very limitedly available in literature. Because of that, a method of boundary layer instability control is discussed which uses a compliant surface [43] in section 2.3.2. This is strictly not a metamaterial, but it does not require any input energy and it still shows interaction with the flow. This concept acts similarly to what is expected from an acoustic metamaterial.

The applications that will be discussed cannot be directly projected on the current project of TS wave cancellation, but they will give an idea of the possibilities. After describing the goals, methods and results of the studies, a paragraph will be added that links the literature to the current research.

2.3.1 Flow stabilisation using a phononic crystal

In the paper by Hussein et al. [44], the goal is to damp TS waves from a laminar boundary layer using a subsurface phononic crystal. A phononic crystal makes use of the elastic wave propagation through an inhomogeneous material. The wave energy is transferred from the TS wave to the elastic waves in the phononic crystal. Due to the interaction between this structure and the passing fluid, some TS wave frequencies are damped out. This study shows the only successful application of acoustic metamaterial concepts in subsonic boundary layer instability control.

The study [44] is based on numerical simulations that represent a fluid flowing through a channel in which the subsurface phononic crystal is present, this is schematically shown in figure 2.18. Manually, a TS instability with a certain frequency is added to the plane Poiseuille flow and its development can be evaluated. The phononic crystal is homogeneous in spanwise direction to make it a quasi-2D problem. Besides this, the crystal is built up from ten unit cells that each include a layer of ABS plastic and a layer of aluminium. The other walls are considered solid as their movement is negligible compared to the movement of the phononic crystal.

The models that are used to evaluate the interaction between the flow and the phononic crystal are an uncoupled model used for predictions and a coupled Fluid-Structure Interaction (FSI) model that gives the actual solution. For the uncoupled model, a harmonic force is implied to the top of the phononic crystal and its response is investigated for different frequencies. Part of the result from this model is a dispersion curve that corresponds to the phononic crystal. This is shown in figure 2.19. In this figure, it can be seen that there are two operating areas of the phononic crystal. There is the pass band, in which an in-phase response is expected and there is a stop band, in which out-of-phase responses with respect to the TS wave can be present. As this last phenomenon is desired for TS wave damping, TS waves in this stop band are more thoroughly evaluated to see whether they are suppressed because of the behaviour of the phononic crystal.

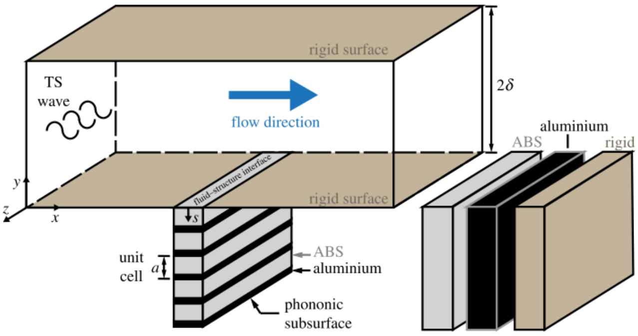

Figure 2.18: Schematic of the channel used in the study by Hussein et al. [44]

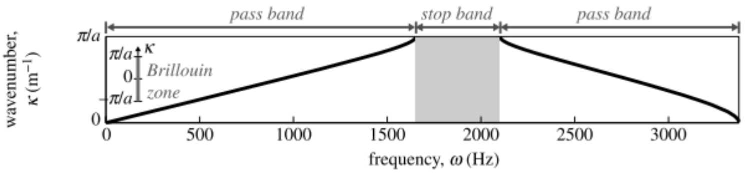

Figure 2.19: Dispersion curves from the phononic crystal [44]

The second model that was used in this paper is a FSI model that solves for the flow and the solid and couple their solutions at the interface. The results from this solver are considered the actual performance of the crystal. In figure 2.20, the performance calculated using both models is given. It can be seen that the uncoupled model gives a good indication of the actual performance of the crystal. The left axis gives the performance according to the performance metric that combines the amplitude and relative phase between the force acting on the crystal and its top surface displacement. The right axis gives the difference in perturbation kinetic energy in the flow past the crystal. In almost the whole stop band, TS wave attenuation is expected, with a maximum reduction at 1690 Hz.

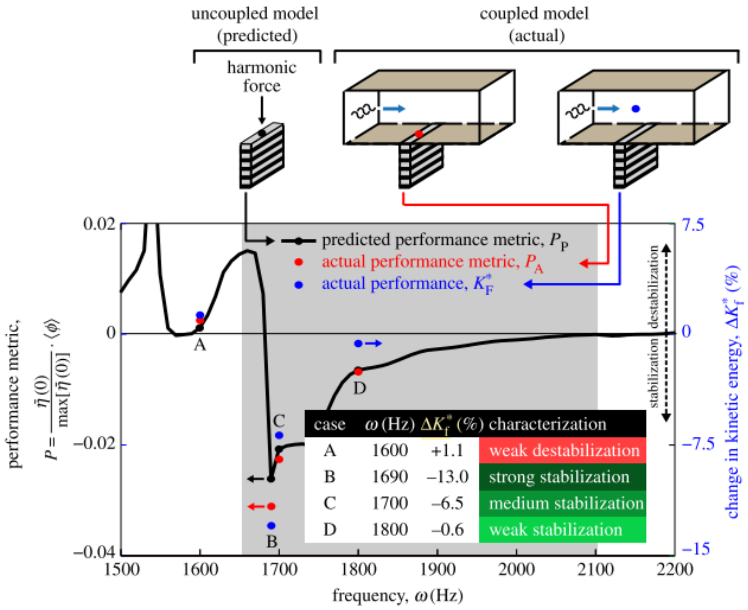

case	ω (Hz)	ΔK_f^* (%)	characterization
A	1600	+1.1	weak destabilization
B	1690	−13.0	strong stabilization
C	1700	−6.5	medium stabilization
D	1800	−0.6	weak stabilization

Figure 2.20: Performance of the phononic crystal in attenuating the passing TS wave [44]

Using the phononic crystal presented in this paper, the perturbation kinetic energy is reduced at certain frequencies and therefore it can be said that this method damps certain TS waves. A real physical implementation of this concept is however challenging due to some chosen parameters in this study. The working fluid is water instead of air, which changes the Reynolds number. Besides that, the geometry of the phononic crystal is not drawn to scale in figure 2.18. The actual steamwise width of the crystal is only 0.676 mm and its height is 10 times the height of a unit cell (0.4 m), so 4 meters. The study shows that the concept of phononic crystals can be used to damp TS waves. However, this was only shown numerically, the concept is far from applicable to a real experimental setting due to the infeasible phononic crystal dimensions.

2.3.2 The use of compliant walls for laminar flow control

In 2001, Carpenter, Lucey and Davies published a review paper [43] that addresses the progress of the use of compliant walls for laminar flow control. Strictly speaking, a compliant wall is not a metamaterial as it does not consist of multiple sub wavelength resonant elements. However, since the interaction between the compliant wall and the passing flow is similar to the interaction in a metamaterial concept, this study is investigated in this section. Moreover, the compliant wall interacts with the boundary layer instability like it is an actively actuated system, however, there is no energy required as an input. This is similar to the expected behaviour of an acoustic metamaterial.

A wall can be called compliant if it is a passive flexible wall in which free surface waves propagate with the same speed as the free stream velocity. At the interface between this wall and the fluid, an energy transfer takes place. This can happen in the form of travelling-wave flutter, where there is an irreversible energy transfer from the flow to the wall. In the experiment conducted by Gaster [45], from which a schematic is shown in figure 2.21, the influence of this travelling-wave flutter on the TS wave development was tested with water as the working fluid. The main outcome was that the passing TS wave of a certain frequency could be completely suppressed by this compliant wall. As mentioned earlier, the suppression is mainly caused by irreversible energy transfer from the wave to the flexible wall. If there was an unsteady potential flow passing over the compliant wall, the phase difference between the pressure and the wall normal velocity would be 90 degrees. The net work done by the fluctuating pressure over a full cycle is zero, which makes it a conservative (reversible) system. But due to the presence of the boundary layer, this phase difference is changed such that it becomes a non-conservative system in which net work is done by the fluctuating pressure of the boundary layer instability. In this case, energy is transferred from the instability to compliant wall to achieve TS wave damping [43].

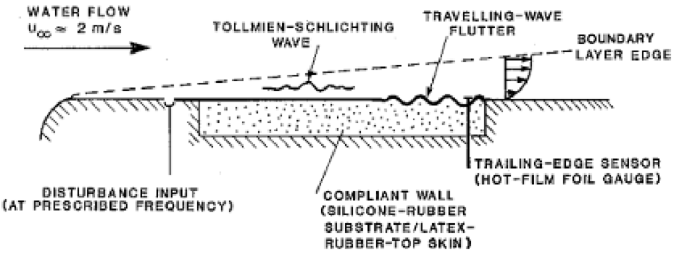

Figure 2.21: Schematic of experiment used by Gaster
Taken from [45]

The paper by Carpenter et al. [43] conjectures that a compliant wall can be used for TS wave damping. The main difference between the situation described in this paper and situation of the current study is that the working fluid is water instead of air. Theoretically and numerically, the same relations hold for both fluids. However, testing experimentally, brings up substantial challenges. The density of water is approximately 800 times the density of air and the kinematic viscosity of air is 15 times higher than the kinematic viscosity of water. Since the compliant wall inertial properties need to be similar to those of the fluid, a very delicate material needs to be used in this wall. The study [43] concludes that the aeronautical application of compliant walls is impractical because of a lack of robustness.

2.3.3 Impedance-near-zero acoustic metasurface for hypersonic boundary layer flow stabilisation

The study by Zhao et al. [46] focuses on hypersonic flow control. For hypersonic flow the Mach number is between $5 \leq M \leq 10$ and the boundary layer looks completely different in comparison with a subsonic boundary layer. The path to transition, however, is similar and follows the scheme given in figure 1.1a. That is why this study is relevant for the current research.

For the hypersonic boundary layer, the most dominant path to transition is the linear amplification of the first or Mack second mode (according to the theory of Mack [14]) which can eventually break down to turbulence. For cooling wall conditions, the first mode (similar to the TS wave) is stabilised, but the Mack second mode remains unstable and this mode can trigger transition. Transition towards a turbulent hypersonic boundary layer is unwanted due to an increase in drag and heat flux.

The Mack second mode behaves like an acoustic wave inside a waveguide between the wall and the sonic line above it. It belongs to the family of trapped acoustic waves and they represent inviscid instabilities of acoustic nature [47]. The phase velocity of this propagating wave is higher than the speed of sound. Every time the wave is reflected at the sonic line, its nature changes from compression to expansion or the other way around. The frequency of the Mack second mode in a boundary layer is in the order of $\mathcal{O}(10^5)$ Hz, which is in the ultrasound band of the spectrum. Research has been conducted that uses an Ultrasonic Absorptive Coating (UAC) to absorb the acoustic energy inside the unstable mode to suppress it [48]. The main idea behind this research is to promote incident ultrasonic wave scattering to suppress the unstable modes in the boundary layer. The assumption was made that the acoustic energy dissipation is critical for attenuation of the Mack second mode.

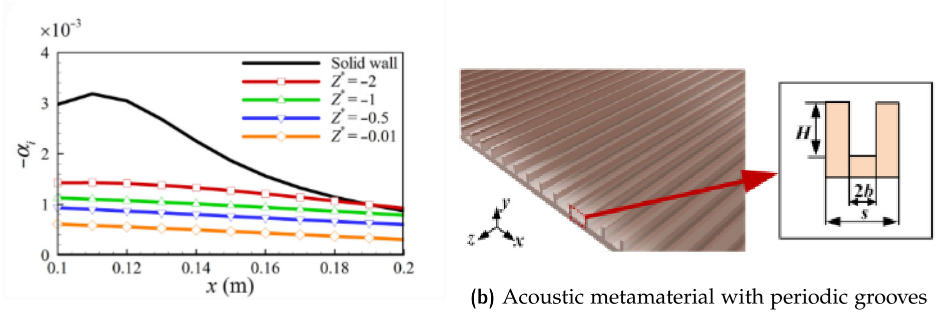

(a) Growth rate of Mack second mode for different impedance values

(b) Acoustic metamaterial with periodic grooves

Figure 2.22: Taken from [46]

A specific parameter to describe the influence of a surface to an acoustic wave is the impedance, denoted with $Z = p'_w / v'_w$, pressure fluctuations at the wall divided by the wall normal velocity fluctuations. This was also discussed in the paper by Li et al. [10] mentioned in section 2.2.2. To obtain a wall with the optimal sound absorptive capabilities, the normalised surface acoustic impedance $Z^* = Z/Z_0$ needs to become -1. The minus sign is added because of a convention difference with the paper of Li et al. [10]. However, the growth rate of the Mack second mode seems to decrease even further as Z^* approaches zero. The wall boundary becomes non-dissipative and the Mack second mode is even more effectively suppressed [46], which can be seen in figure 2.22a. Realising an impedance-near-zero boundary is difficult with traditional materials and structures, so here the solution was found in acoustic metamaterials. A rigid surface with periodically arranged sub-wavelength grooves was opted as the metamaterial to use (figure 2.22b). The geometry of these grooves determine the acoustic impedance.

With a Direct Numerical Simulation (DNS), three surfaces were tested and compared (figure 2.23a). As a baseline, a rigid wall with an impedance of $Z^* = -\infty$ was taken. A perfectly absorbing surface was taken with an impedance of $Z^* = -1$ and an impedance-near-zero surface was taken with $Z^* = 0.15$. In a hypersonic boundary layer, the grooved surface with a matched impedance inhibits amplification of the Mack second mode. The main cause of this is absorption due to viscothermal dissipation inside the grooves. The impedance-near-zero wall boundary succeeds even better in suppressing the Mack second mode, this can also be seen in figure 2.23b. The main principle behind this behaviour is not absorption, but out-of-phase superposition of a pressure wave. This impedance-near-zero grooved acoustic metamaterial outperforms the UAC in suppressing the Mack second mode to stabilise a hypersonic boundary layer although this is a non-dissipative surface.

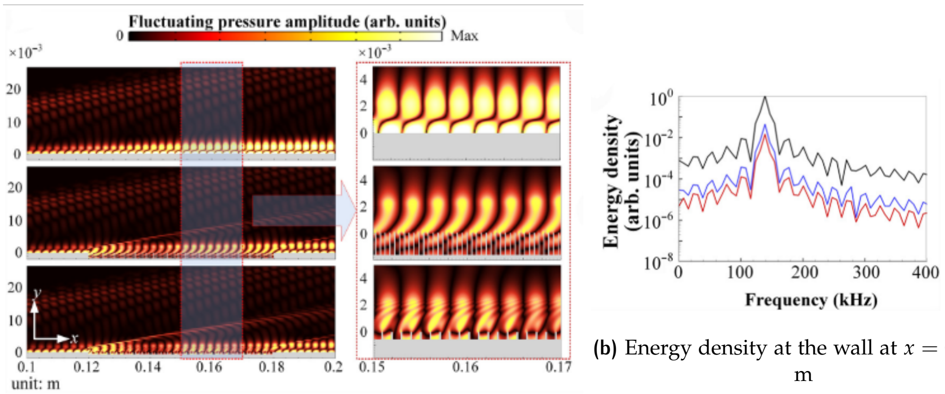

(a) 2D contour plot of pressure fluctuation amplitude for the three tested metasurfaces

(b) Energy density at the wall at $x = 0.16$ m

Figure 2.23: Taken from [46]

The method suggested by Zhao et al. [46] suppresses the Mack second mode in a hypersonic boundary layer adequately. If this method is projected on the current study with a subsonic boundary layer and TS waves as the most dominant mode in the path to transition, some challenges arise. First, the frequency of the Mack second mode is in the ultrasonic band, where the TS waves in a boundary layer of about 20 m/s are most unstable in the order of 300 Hz. Designing an impedance matched or an impedance-near-zero surface for these low frequencies can lead to some (practical) difficulties.

Secondly, the Mack second mode grows linearly following LST in 2D. However, the nature of the Mack second mode is different from the TS wave. Where the TS wave is a convective instability with a moving mass and a fluctuating pressure, the

Mack second mode behaves more like an acoustic wave. Therefore metamaterial concepts from acoustics might be more easily applicable to suppressing these secondary modes.

The three concepts discussed in this section are used to delay boundary layer transition in their own way. A similarity between the concepts is that they interact with the boundary layer instabilities as if they are actively actuated, but they are not. There is no energy required to achieve the TS wave damping. However, in order to come from the methods described in this section, to a concept that damps TS waves in an experimental setup, some challenges must be overcome. The concepts suggested by Hussein et al [44] and Carpenter et al. [43] are proven numerically or with water as working fluid, but for experimental aeronautical applications these concepts are not feasible. Therefore, the potential of another acoustic metamaterial concept will be investigated in this study.

2.4 INTERACTION BETWEEN HELMHOLTZ RESONATOR AND BOUNDARY LAYER

As described in sections 1.1.2 and 2.2, the chosen acoustic metamaterial concept for the experimental study includes system of Helmholtz resonators. A series of Helmholtz resonators seems to attenuate acoustic waves of certain frequencies [6] [8] [9] and even a single unit can can suppress sound waves in a waveguide [11]. In literature, there are limited references that investigate the interaction between a Helmholtz resonator and instabilities like TS waves in a laminar boundary layer. However, some related studies discussed in this section. These studies are mostly investigating the interaction between a Helmholtz resonator and a turbulent boundary layer.

The excitation of a Helmholtz resonator by a turbulent boundary layer was investigated by Panton & Miller [49]. This was done experimentally on the fuselage of a sailplane with a microphone in the boundary layer above the resonator throat and inside the resonator cavity. The outcome of the study shows that the turbulent fluctuations in a boundary layer with a broaden frequency spectrum can excite a Helmholtz resonator on its resonant frequency. Moreover, it was shown that the resonant frequency of the Helmholtz resonator can change with the flow conditions. This relates to the end correction in the moving mass that fluctuates in the resonator throat, denoted with L' in equation 2.3 in section 2.2.2. In static conditions, this is a fixed volume of air, but with grazing flow, this correction factor is dependent on the flow conditions [49]. Another conclusion drawn from this study was that acoustic sound was radiated from the resonator back into the flow.

A further investigation into the pressure fluctuations inside the resonator cavity due to boundary layer excitation is performed by Ma et al. [50]. This study suggests that the complex pressure fluctuation inside the resonator equals the hydrodynamic forcing from the boundary layer divided by the acoustic impedance of the resonator (equation 2.5). This impedance can be determined in quiescent conditions and the integrated vorticity-velocity product can be interpreted as the hydrodynamic forcing that excites the resonator. The response of the resonant frequency of the resonator to the passing flow is also dependent on the quality factor of the Helmholtz resonator [50].

$$\hat{p}^*_{\text{res}} = \frac{\hat{F}^*}{Z^*} \tag{2.5}$$

In research conducted by Flynn et al. [12], the influence of a single spanwise row of Helmholtz resonators to the turbulence inside a turbulent boundary layer is investigated. The main conclusion of the experimental study was that the resonators suck in high momentum flow and expel low momentum flow back into the boundary layer. The velocity defect that is introduced by this effect increases the turbulent fluctuations in the boundary layer for the u- and v-velocity closely downstream of the Helmholtz resonator row. With this increase in turbulent fluctuations, the Reynolds shear stress is increased. Besides this, the momentum thickness is locally increased at the streamwise position of the row of resonators. Another observation was that there is no noticeable upstream effect in velocity fluctuations of the Helmholtz resonators [12].

Because the study by Flynn et al. [12] shows a local increase in near-wall velocity fluctuations, Lin et al. [13] used this concept to delay separation. The main idea behind this concept is that tripping a laminar boundary layer to a turbulent one, makes the flow stay attached longer. This was also shown by Lin et al. [13] by using vortex generators. The Helmholtz resonators produce an acoustic disturbance, but an effect of the resonators to the separation location was not noticeable. In the paper [13], this was mainly explained by the observation that the effect of the Helmholtz resonators to the turbulence level seems to attenuate further downstream. This was also a presented result in the paper by Flynn et al. [12].

The presented studies refer mostly to the excitation of Helmholtz resonators to turbulent pressure fluctuations in the flow and what the dependency is of flow conditions to the resonant frequency. Also, the turbulent velocity fluctuations in the boundary layer are amplified locally by the presence of the resonator. However, further downstream, these fluctuations are too weak to potentially delay flow separation. All in all, the interaction between a Helmholtz resonator and a boundary layer is studied, but the specific effect of the resonator to Tollmien-Schlichting waves in a laminar boundary layer is not discovered yet.

3 METHODOLOGY

In the introduction chapter in section 1.1.1, the linear stability theory by Mack [14] and the parabolised stability equations by Herbert [15] are discussed. With these techniques, the boundary layer stability can be visualised in stability diagrams (figures 1.2 and 1.2). From these figures, the conclusion can be drawn that the most unstable TS waves have a low frequency. In the state of the art chapter (section 2.2), different acoustic metamaterial concepts are described. The two mainly used concepts are the mass-membrane system to achieve a negative effective mass/density and the Helmholtz resonator (HR) to get a negative bulk modulus in specific frequency bands. The position and width of this band in the frequency domain is dependent on the resonant behaviour of the system and the meta-atoms. The parameters influencing the resonant properties of a mass-membrane system are the geometry of the membrane, the size of the mass, the material the membrane is made of and the tension in the membrane. For an experimental setup in which resources are limited, it is not feasible to tune all these parameters up to the desired specifications. Thus, the chosen metamaterial concept that is investigated in this study is a system of Helmholtz resonators. The resonant behaviour of a Helmholtz resonator is only dependent on the geometrical parameters of the throat and cavity. This is beneficial for the feasibility of using this concept in an experimental setting. This choice is more elaborately justified in sections 1.1.2 and 2.2.

In most studies regarding this kind of metamaterials, a particular lattice or array of Helmholtz resonators is connected to a waveguide and the transmission is evaluated [6] [8] [9] [10]. In the paper by Fey & Robertson [11], the influence of a single resonator to sound transmission is studied. Although a single HR can technically not be seen as an acoustic metamaterial, this meta-atom was already able to suppress sound waves with some particular frequencies. Since this thesis describes an exploratory study to the application of metamaterials to boundary layer stability control, the influence of a single HR to TS wave development will be investigated. The results of a test with a single meta-atom of a metamaterial could give an insight in the interaction between boundary layer instabilities and a complete acoustic metamaterial. Since the boundary layer over a flat plate can be assumed to be two-dimensional, the resonator is also made 2D. The numerical models that are used to investigate the interaction between the Helmholtz resonator and the TS wave are also two-dimensional. The setup is constant in the spanwise direction. In order to achieve a 2D resonator in the experiment, the geometry highlighted in red in figure 3.1 is stretched in spanwise direction. This means that the resonator throat is a slotted opening in the flat plate model, which is connected to the a rectangular box that serves as the cavity of the resonator.

A flat plate model is used without any externally exerted pressure gradient. A schematic of the model is given in figure 3.1. An initial instability is introduced to the flow upstream of the resonator (at x_i) with a frequency that will amplify sufficiently downstream to be measurable near the resonator. The amplification factor N of the TS wave can be predicted from a calculation using a PSE solver that uses the approach described in section 1.1.1. This TS wave frequency is chosen close to the resonant frequency of the resonator.
In order to perform experimental measurements in the setup visualised in figure 3.1, three microphones are installed in the model. These are highlighted in blue.

Moreover, images will be acquired during the experiment to get a quantitative flow field using PIV or PTV. The field of views used in this study are highlighted with the red and green boxes in figure 3.1. The experimental measurements can be compared with numerical models that simulate the experimental setup. The flow and the geometrical parameters of the flat plate model are given in table 3.1. It must be noted that the free stream velocity and therefore the Reynolds number is fixed throughout the study.

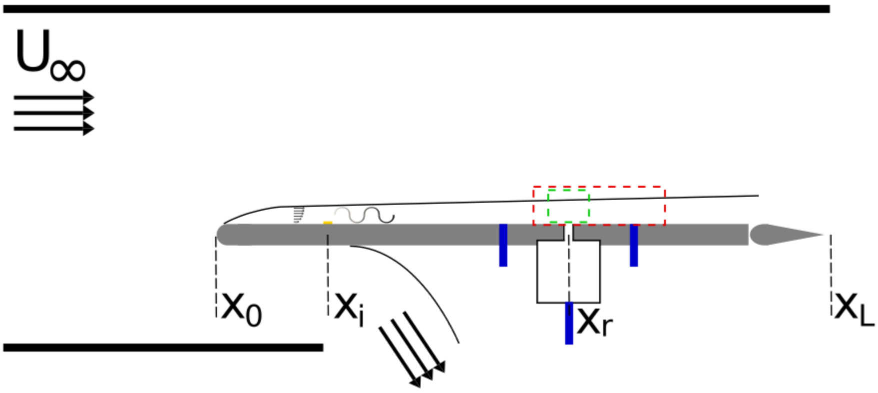

Figure 3.1: Schematic of the used test setup throughout the study

Table 3.1: Test setup parameters

Parameter	Symbol	Value
Free stream velocity	U_∞	20.8 m/s
Position initial instability	x_i	0.182 m
Position resonator	x_r	0.55 m
Length of the flat plate	x_L	1 m
Reynolds number	Re_L	$1.4 \cdot 10^6$

For these flow parameters, a stability analysis can be performed using a PSE solver. With this, it can be investigated what TS wave frequency has the highest amplitude at the resonator location x_r when it is initiated at x_i. The N-factor, determined with all values of α_i including positive ones, at x_r is given over a range of frequencies in figure 3.2a. It can be seen that the frequency with the highest N-factor, computed with a PSE solver based on the equations given in section 1.1.1 is around 320 Hz. The resonant frequency of a 2D Helmholtz resonator with a square cavity of 68 × 68 mm, a throat length of 5 mm and a throat width of 1 mm is approximately 290 Hz. This frequency is determined in an iterative process using a COMSOL Muliphysics thermoviscous acoustics simulation, which is discussed more elaborately in section 3.1.1. The resonant frequency of the resonator and the TS most substantial effect of the resonator on the TS wave stability is expected near resonance. The main frequencies on which the TS wave development will be analysed throughout the report are 240, 270, 290, 310 and 340 Hz. Most of these frequencies are inside the unstable region of the stability diagram at x_r, according to figure 3.2b.

In this chapter, three methods to investigate the influence of the resonator to the TS wave development are described. First, an adjusted PSE solver will be discussed in which inhomogeneous boundary conditions are added to model the presence of a resonator or another arbitrary v-velocity boundary condition. Next, a high-fidelity linearised Navier-Stokes simulation is presented. This simulation will give insight in all flow parameters in the resonator, the boundary layer and the free-stream. Eventually, the experimental wind tunnel test setup will be described. This

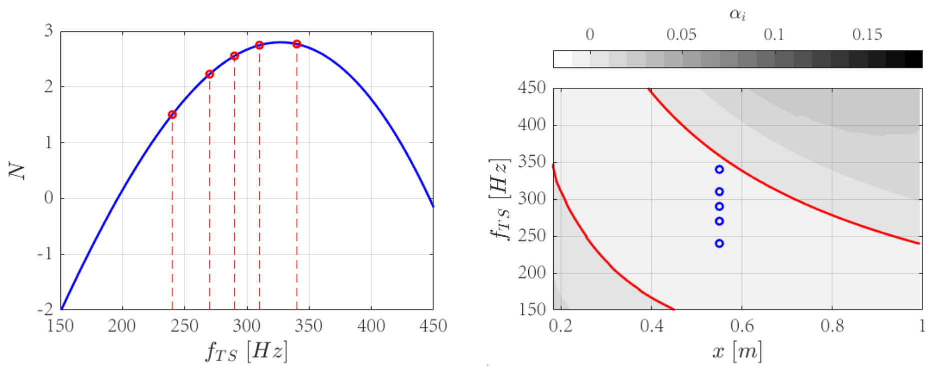

(a) N-factor of TS waves at x_r introduced at x_i, the red circles represent the mainly used frequencies

(b) Growth rate α_i, the red line represents the neutral stability curve and with blue circles the main evaluation points are highlighted

Figure 3.2

description includes the way the initial instability is introduced in the flow and the flow measurement techniques used to measure the relevant flow parameters.

3.1 ADJUSTED PARABOLISED STABILITY EQUATIONS

Prior to performing extensive wind tunnel tests or simulations with high computational costs, it is convenient to predict the outcome with a low-fidelity numerical model. In order to make this prediction, a solver based on the PSE theory by Herbert [15] with some modifications is made. PSE was chosen over LST because of the lower computational costs and the possibility to inert a periodic inhomogeneous boundary condition for the u- and v-velocity at certain x-locations as discussed in section 1.1.1. This inhomogeneous boundary condition can be arbitrarily chosen to simulate an ideal boundary condition. However, it is also possible to find the frequency response of the Helmholtz resonator from a thermoviscous acoustics simulation in COMSOL Multiphysics [51] and use this as an input to the solver. The procedure followed in this adjusted PSE solver with inhomogeneous boundary conditions calculation is given here. First, the implementation of the arbitrary v-velocity boundary condition is described. The coupling between the adjusted PSE solver and the thermoviscous acoustics simulation is discussed afterwards, in section 3.1.1.

In order to run PSE calculations over a boundary layer, first, a boundary layer needs to be created. This is done with a boundary layer solver. A non-similar boundary can be resolved on a 2D (x, y) domain $[S, L] \times [0, H]$. An implicit discretisation scheme is used in x-direction, while in y-direction, Chebyshev polynomals are used. Inflow boundary conditions are produced by a Falkner-Skan-Cooke solver. To get the output of the u- and v-velocities and their derivatives with respect to y in the domain, the input settings must include the domain geometry, free stream flow properties and the amount of grid points in all directions. The input parameters used to create the boundary layer are listed in table 3.2. The domain height is dependent on the boundary layer thickness δ_{99} the end of the domain. This is calculated with the Blasius boundary layer theory. The equation to calculate this Blasius boundary layer height is given in equation 3.1.

$$\delta_{99_{\text{Blas}}} = 4.91\sqrt{\frac{\nu L}{U_\infty}} \tag{3.1}$$

The boundary layer that is computed from the boundary layer solver will be used as an input to the PSE solver. The underlying main assumptions and equations are

Table 3.2: Input parameters to create boundary layer

Parameter	Symbol	Value
Domain start (streamwise)	S	0.182 m
Domain end (streamwise)	L	1 m
Domain height (wall-normal)	x_r	$6\ \delta_{99_{\text{Blas}}}$ m
Chebyshev node coordinate median (wall-normal)	y_i	$2\ \delta_{99_{\text{Blas}}}$ m
Free stream velocity	U_∞	20.8 m/s
Kinematic viscosity	ν	$1.511 \cdot 10^{-5}$ m^2/s
Reynolds number	Re_L	$1.4 \cdot 10^6$
Amount of grid points in streamwise direction	n_x	500
Amount of grid points in wall-normal direction	n_y	300

described in section 1.1.1. The solution marches through the domain in streamwise direction, the solution at point x_n is used to compute point x_{n+1}. To get the solution on x_1, a LST calculation is used because this method is independent of information on other steps. The amount of Chebyshev polynomials N_{Cheb} taken into account in the PSE calculation is 80.

In order to get a stable PSE calculation, the marching step size in streamwise direction is limited. The governing equations that are used in the PSE approach require a sufficiently large step size in order to 'skip' over the weak and rapidly decaying upstream propagation of information [15]. In this way, the equations can be solved as an ill-posed initial boundary value problem. If the marching step size is too small, numerical instabilities can occur. This is caused by a residual ellipticity of the parabolised stability equations. However, this ellipticity is necessary to describe the instability in the form of a wave [15].

The choice of the marching step size is therefore always a trade-off. Especially if an inhomogeneous boundary condition is imposed on one or multiple nodes. A small step size would make this boundary condition local and in better accordance with the modelled situation. However, the PSE solver must remain stable in order to give an output. In this study, the step size Δx is dependent on the situation. In general the step is around 20 to 25 mm, which is relatively large, but necessary to assure solver stability.

Normally, the boundary conditions at the wall in the PSE calculation are homogeneous. This means that the velocity fluctuations at the wall and at the free stream are zero ($v_{\text{wall}} = u_{\text{wall}} = v_{\text{fs}} = u_{\text{fs}} = 0$). So in order to model a resonator connected to the wall, an inhomogeneous v-velocity boundary condition is imposed at $x = x_r$ based on the local pressure at that x-location at the wall ($x = x_r$ and $y = 0$). To investigate the desired relation between pressure and velocity at the wall, an ideal situation is created. In this ideal situation, the amplitude ratio between p_{wall} and v_{BC} can arbitrarily be chosen. The N-factor that results from the PSE calculation can be evaluated at a point downstream of the resonator and compared with a baseline configuration without a resonator to get to the optimal $v - p$ relation.

Mathematically, this inhomogeneous boundary condition is inserted in the right hand side (RHS) of equation 3.2. This equation results from equation 1.10, which is the compact form of the governing equation as described in section 1.1.1. An explicit differencing scheme is used to calculate $\partial \mathbf{q}/\partial x$ with the knowledge of the solution of the previous spatial step. The left hand size (LHS) of equation 3.2 is unknown, while the RHS is either known from the previous step or imposed by boundary conditions.

$$\underbrace{\left[L + \frac{M}{dx} + \frac{d\alpha}{dx}N\right]}_{\text{LHS}} \mathbf{q}_i = \underbrace{\frac{M}{dx}\mathbf{q}_{i-1}}_{\text{RHS}} \tag{3.2}$$

The RHS vector has a length of 4 times N_{Cheb}, to include the velocities (u, v and w) in three directions and the pressure in that order. The indexing goes from high in the domain (free stream) to low (wall) per velocity/pressure. This means that the first index of the RHS vector is the perturbation of the u-velocity at the free stream and that index N_{Cheb} is the perturbation of the u-velocity at the wall. These are manually imposed to be zero to comply to the no-slip conditions. The shape of this RHS vector is clarified with equation 3.3.

$$\text{RHS} = [u_{\text{fs}}, \cdots, u_{\text{wall}}, \; v_{\text{fs}}, \cdots, v_{\text{wall}}, \; w_{\text{fs}}, \cdots, w_{\text{wall}}, \; p_{\text{fs}}, \cdots, p_{\text{wall}}]^T \tag{3.3}$$

The indices between the free stream and the wall, denoted with the dots in the vector in equation 3.3 are computed with the eigenvector of the previous spatial step. The indices shown in this vector are all imposed boundary conditions. In the homogeneous situation all of these are zero and the left hand side matrix from equation 3.2 is modified such that the boundary conditions are correctly represented in the eigenfunction $\mathbf{q}_i$.

For the adjusted PSE solver, an inhomogeneous v-velocity boundary condition is imposed at the wall. At the streamwise position that coincides with the resonator location x_r, the pressure at the wall is evaluated by picking the last index of eigenvector $\mathbf{q}$ at the particular x-location. The amplitude of this pressure is multiplied with a factor A_{BC} to get the amplitude of v_{BC} in the frequency domain. A term ϕ_{BC} is added to the phase of the pressure to get the phase of v_{BC}. The phase and the amplitude of the boundary condition can arbitrarily be chosen via the factors A_{BC} and ϕ_{BC}. These can be used to find out the optimal boundary condition to damp the TS wave. This process is visualised with the diagram in figure 3.3. The pressure boundary conditions follow from the compatibility conditions, denoted with 'comp.' in this diagram. Per x-location, the determination of the solution is an iterative system. The TS wave characteristics, including the extracted wall pressure and the imposed v-velocity boundary condition need to converge before marching to the next station. The regular PSE solver is developed within the boundary layer stability research group of the TU Delft. The modifications to include an arbitrary v-velocity boundary condition are given in appendix A.1.

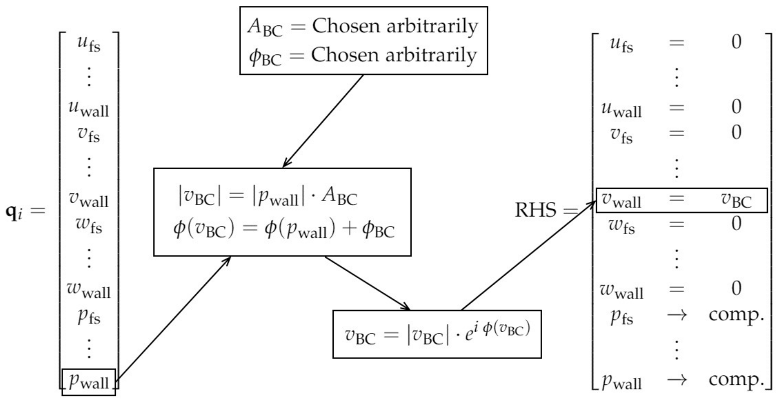

Figure 3.3: Diagram of the implementation of the arbitrary v-velocity boundary condition

3.1.1 Modelling of resonator in adjusted PSE

To model the presence of the resonator, the terms A_{BC} and ϕ_{BC} can be extracted from a thermoviscous acoustics simulation in COMSOL [51]. The use of an acoustic simulation to capture the behaviour of the resonator is justified by the assumption that everything under the surface, inside the resonator happens acoustically. A two dimensional resonator is modelled as shown in figure 3.4a. In the frequency domain, a linear perturbation is imposed above the throat for a range of frequencies. This is used to determine the response of the resonator. This response is captured by evaluating the pressure and the acoustic velocity at the resonator throat exit ($y = 0$). In this simulation, no external (boundary layer) flow is imposed to the domain. The amplitude A_{BC} is calculated with the use of amplitude ratio of $|v_{\mathrm{tv}}|/|p_{\mathrm{tv}}|$. The phase angle ϕ_{BC} is calculated using the difference between the phases $\phi(v_{\mathrm{tv}}) - \phi(p_{\mathrm{tv}})$. For a range of frequencies, these parameters look as shown in figure 3.4b. This is calculated for the resonator geometry described in the first part of this methodology chapter. For the coupling between the adjusted PSE solver and the thermoviscous acoustics simulation, the values for A_{BC} and ϕ_{BC} can be used as an input to the PSE calculation as shown in figure 3.3.

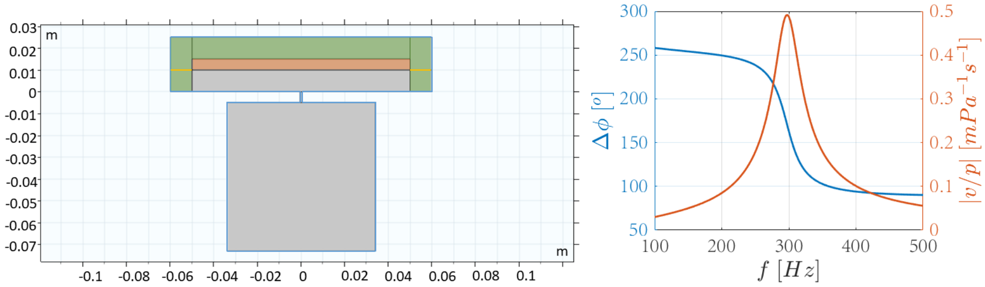

(a) Setup for the thermoviscous acoustics simulation in COMSOL, the perturbation is imposed on the orange domain, the green domains are perfectly matched layers and blue and yellow lines represent walls and interior walls respectively

(b) Amplitude phase response of the resonator with in blue (left y-axis) the phase difference $\phi_v - \phi_p$ and in red (right y-axis) the amplitude relation $|v|/|p|$

Figure 3.4

The mesh that is used for this thermoviscous acoustics simulation has similar characteristics as the mesh used for the linearised Navier-Stokes simulation that is described in section 3.2. The minimum size of the rectangular elements equals half the viscous penetration depth for a wave with a frequency of 300 Hz (equation 3.4). This dependency on δ_ν is chosen to catch the oscillating boundary layer that forms for the acoustic wavelength in the simulation. The maximum growth rate of the elements is 1.05, so the maximum element size of 5 mm is not reached within this domain.

$$\delta_\nu = \sqrt{\frac{2\eta}{\omega\rho}} \tag{3.4}$$

Where η is the gas viscosity and ρ the density of the gas.

The boundary condition of the resonator should only work over the width of the throat. The step size of the PSE is generally longer than the width of the resonator throat. The effective boundary condition is therefore normalised with the ratio between the throat width and the PSE step size. This could possibly change the effect of the resonator, as a sharp peak with a high gradient can influence the TS wave differently than a weaker effect that continues over a longer distance. However, since the step size of the (adjusted) PSE is limited as described above, this implementation is still chosen.

The elements of eigenvector $\mathbf{q}$ in the adjusted PSE solver are non-dimensional and do not have a physical meaning. In order to use pressure at the wall to impose a boundary condition in v to model the resonator, this pressure needs to be dimensional. This dimensionalisation can be done by multiplication with ρU_∞^2. This dimensional pressure serves as the input for the dimensional transfer function derived from the thermoviscous acoustics simulation. This transfer function is linear and therefore only dependent on the frequency. Eventually, the dimensional v-velocity boundary condition needs to be non-dimensionalised before inserting it in the PSE calculation.

In order to control the magnitude of the modelled resonator effect, a multiplication factor F_{BC} is included in the transfer function. If $F_{\mathrm{BC}} = 1$, the full predicted effect is used in the calculation. However, if the magnitude of this effect is too large, the PSE solver can become unstable. With the multiplication factor, the resonator effect can be controlled to get a stable output in most situations. A diagram of the final implementation of the thermoviscous acoustics simulation in the adjusted PSE solver is given in figure 3.5. The corresponding Matlab code is given in appendix A.2.

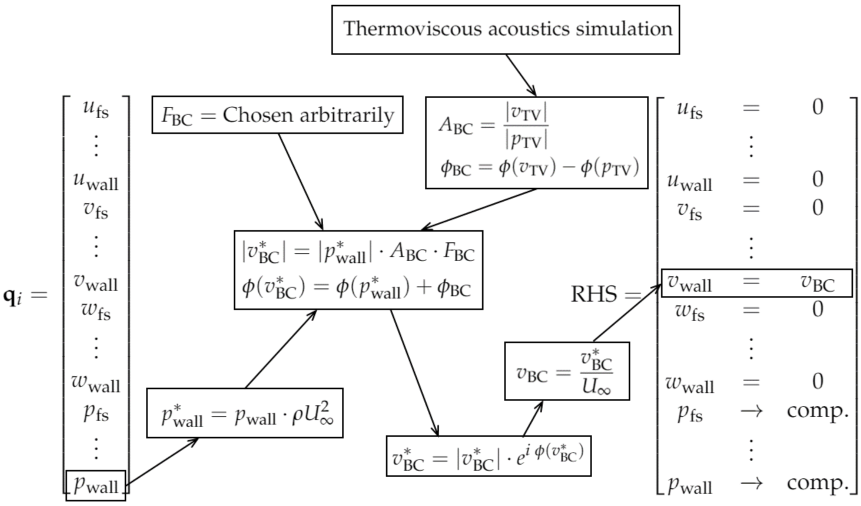

Figure 3.5: Diagram of the implementation of the thermoviscous acoustics simulation in the adjusted PSE solver

3.2 LINEARISED NAVIER-STOKES SIMULATIONS

Predictions of the outcome of the experiments can be made with the adjusted PSE solver as described in the previous section. In order to predict the influence of the resonator to the boundary layer stability in more detail with a higher-fidelity model, the linearised Navier-Stokes (NS) simulation from COMSOL Multiphysics is used. The linearised version of the Navier-Stokes equations, can be found in COMSOL documentation [51]. This simulation determines the transient behaviour of a perturbation pressure/velocity over a steady state field. This steady state field will first be determined by using a combination of the 'Laminar flow' [52] and 'Heat transfer in fluids' [53] solvers. With this coupling the full compressible Navier-Stokes equations are solved without turbulence modelling, so this can be considered a 2D DNS. This simulation is stopped if the field converges into a steady state which can serve as the basis to run the linearised Navier-Stokes simulation on to model the perturbations. The boundary layer from the steady state simulation can also be used as the input for the (adjusted) PSE solver instead of the boundary layer that is computed with the boundary layer solver as described in section 3.1.

The complete two dimensional setup is given in figure 3.6. At the position where a TS wave is introduced, a distributed sinusoidal forcing is added as a body force in a small domain just above the wall. This models the plasma actuator used in the experiment to introduce a TS wave. The body force exerted by a plasma actuator is discussed in section 2.1. The implementation of this actuator in the experiment is discussed later in section 3.3.1. The TS wave develops over space and time until a converged wave is passing over the resonator. From the linearised Navier-Stokes simulation, per time step, the spatial development of the TS wave can be evaluated. Moreover, the transient development of the pressure and velocity inside and outside the resonator can be investigated.

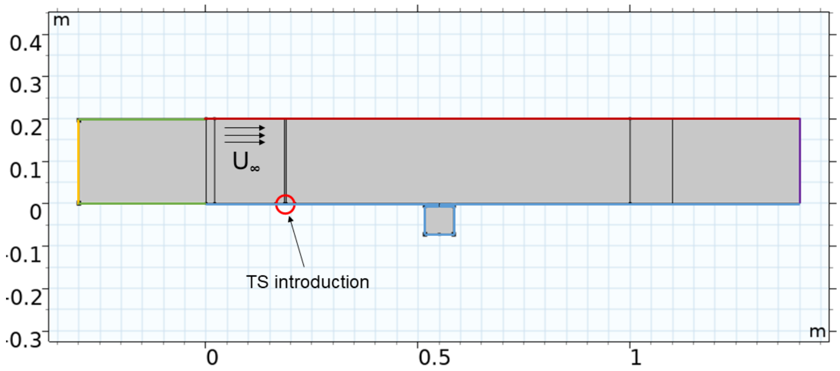

Figure 3.6: Setup used for linearised NS simulation in COMSOL, the yellow and purple lines indicate the in- and outflow respectively, the blue lines represent the no-slip walls, the red line indicates a slip wall and the green walls have an imposed symmetry condition

The boundaries highlighted in blue in figure 3.6 are considered no-slip walls. The yellow and purple lines indicate the in- and outflow respectively. At these boundaries, the velocity perturbation is imposed to be zero. The green lines indicate the boundaries where a symmetry condition is applied. Lastly, the red line represents a slip wall at the top of the domain. The mesh that is used for the linearised NS simulation is similar to the one used for the thermoviscous acoustics simulation described in section 3.1.1. The used mesh is structured and built-up from rectangular cells. The smallest elements have a width and height of half the viscous penetration depth for a frequency of 300 Hz (equation 3.4). The maximum element width is 7 times the minimal element width. In height, the maximum size is 10 times the maximal element width. These element sizes are chosen to make sure that all effects, especially near the resonator throat, can be captured appropriately.

In order to find a similar optimal boundary condition for TS wave attenuation as described for the PSE with inhomogeneous boundary conditions in section 3.1, a linearised NS simulation can be performed without the resonator cavity. Instead of the cavity, an imposed v-velocity boundary condition can be imposed at the bottom side of the throat. This boundary condition has an absolute amplitude and a relative phase delay with respect to the initial TS wave forcing. This phase delay has a range from 0° to 330° in discrete steps to capture a full TS wave cycle. This method of using the linearised Navier-Stokes simulation is referred to as the 'active throat' simulation in section 4.2 of this thesis.

The evaluation of a TS wave at a certain time instance over space needs to take place at a relative distance from the wall, depending on the boundary layer characteristics. This distance can be chosen at a δ^* or at a factor times δ^* from the wall. Boundary layer integral quantity δ^* is a parameter that can be calculated at each x-location of the boundary layer based on volumetric flow rates (equation 3.5. The v-velocity of the TS wave is mainly used to evaluate the amplitude of the TS wave. The v-velocity shape function of the TS wave grows with the boundary layer thickness, so evaluating v at $y = 2\delta^*$ gives a direct image of the TS wave development.

$$\delta^* = \int_0^H \left(1 - \frac{u(x,y)}{U_\infty}\right) dy \tag{3.5}$$

3.3 WIND TUNNEL EXPERIMENT

The wind tunnel experiment takes place in the vertical A-tunnel at the Low Speed wind tunnel Laboratory of the TU Delft. The test section has a cross-section of 0.5×0.5 m and this is filled with a flat plate model with a round leading edge and a sharp, movable trailing edge. This flat plate model is schematically visualised in figure 3.1. A 3D CAD model made in SolidWorks is given in figure 3.7a, next to it, a picture of the experimental setup is shown in figure 3.7b.

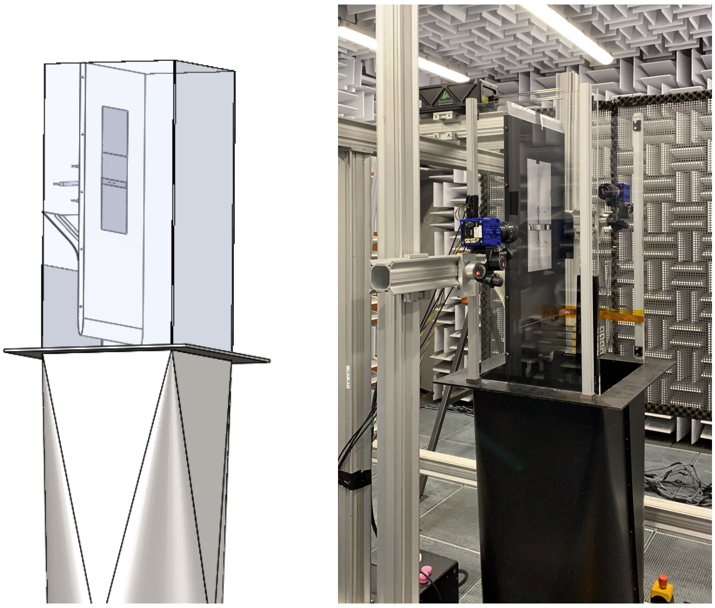

(a) CAD model from SolidWorks **(b)** Picture of the situation

Figure 3.7: Setup wind tunnel test

The test setup is mostly fixed, to keep the testing conditions constant. The only part that is changed in the setup is the throat part in which the narrow slot is milled. Three throat parts are used. The first part does not have a slotted opening to serve as the baseline configuration (C_{base}). The second part has a slot with a width of 1 mm and a depth of 5 mm to create the resonator as described in the first part of this chapter. This configuration will be called C_1. The third throat part (C_2) has a slot with a depth of only 4 mm. It also has a smaller 0.4 mm orifice at the top. Cut-views of the throat parts are shown in figure 3.8. The cavities in this figure, which are connected to the throat parts are not to scale. The third part, configuration C_2, has this narrow part at the top to reduce the local circulation at the surface of the model. Because this small orifice increases the friction of the air fluctuating in the throat, the throat length is decreased. The influence that this has to the resonant behaviour is described in section 4.1.

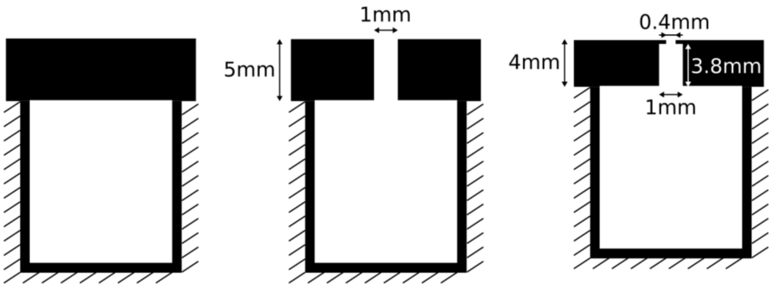

Figure 3.8: Schematic cut-views of the throat part configurations C_{base}, C_1 and C_2

Multiple measurement devices are used in the experimental setup to capture the flow characteristics. Three microphones are installed in the model and over the whole flat plate model, pressure taps are placed to measure the pressure (gradient) at the surface. Besides that, an imaging system is installed to measure and visualise the flow field in a certain field of view using Particle Image Velocimetry (PIV) or Particle Tracking Velocimetry (PTV). The individual measurement techniques are more elaborately described in the next sections.

3.3.1 Plasma actuator

To manually introduce a TS wave in the boundary layer, an Alternating Current Dielectric Barrier Discharge (AC-DBD) plasma actuator is used. In chapter 2, the plasma actuator is identified as a tool to control TS waves in a boundary layer. However, it is also possible to use this tool to introduce a TS wave. With a plasma actuator it is possible to get a specific body force close to the wall (figure 2.4). This body force is controllable in frequency, phase and amplitude by changing the electric input of the plasma actuator. The work described in the paper by Benard & Moreau [54] shows different modulation techniques to get the appropriate forcing inside the boundary layer.

The plasma actuator that is used consists of a layer of copper tape on top of a thin layer of Kapton tape. The Kapton tape serves as the dielectric material. The copper tape is connected to a high voltage AC source. The model itself is made of aluminium and serves as the ground.

A relatively low forcing frequency ($\approx$ 300 Hz) needs to be exerted on the boundary layer in order to get a TS wave growing to a sufficient amplitude at the resonator location. This is needed to observe the waves with the chosen flow measurement techniques described in sections 3.3.2, 3.3.4 and 3.3.5. The used forcing frequencies are described in the beginning of this methodology chapter and based on PSE calculations. The forcing in this frequency range is accomplished using burst modulation similar to what is described in the paper by Benard & Moreau [54]. A full sine wave of a higher carrier frequency is burst at the chosen modulation frequency. This makes the energy per pulse constant. In the frequency spectrum, a peak is expected at the modulation frequency, carrier frequency and at harmonics. However, since we are dealing with boundary layer stability, the only wave that will be amplified between the point of the introduction of the instability and the area of interest near the resonator has the chosen modulation frequency. The peak-to-peak Voltage V_{pp} is fixed to 4 kV. All relevant parameters for the plasma actuator are combined in table 3.3.

Table 3.3: Plasma actuator parameters

Parameter	Symbol	Value
Carrier frequency	f_{car}	4 kHz
Modulation frequency	f_{mod}	[240, 270, 290, 310, 340] Hz
Peak-to-peak Voltage	V_{pp}	4 kV
Amount of sine waves per burst	N_{cycle}	2

3.3.2 Microphones

A TS wave is a convective wave with vortex-like velocity fields. In these waves, the pressure fluctuations are an effect of inertia. The amplitude of the TS wave pressure gives an indication of the magnitude of the TS wave itself. This fluctuating pressure can be captured with microphones, which are mounted to the model. Two microphones are connected to the surface of the flat plate through a pressure tap hole, 60 mm upstream and downstream of the resonator throat location. The third microphone is placed inside the resonator cavity. The placement of the microphones can be seen in figure 3.9. This figure also shows how the flow is redirected at the back side of the flat plate to reduce noise and blockage.

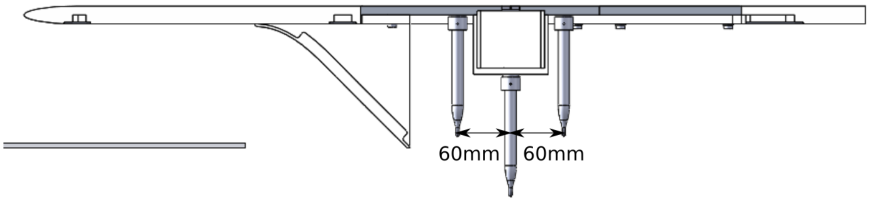

Figure 3.9: Cut-view of the CAD model with the positions of the microphones

The microphones used in this experiment are LinearX M53 measurement microphones. This is a high performance, low voltage electret condenser microphone which has a high sensitivity for low noise applications. The microphones have an output in Voltage. To translate this Voltage signal into a pressure signal, a pistonphone is used for calibration. The microphone inside the resonator cavity was calibrated inside the pistonphone because it is exposed completely inside the cavity. The other two microphones measure through a narrow orifice in the surface. Therefore, these are calibrated with the pistonphone in-situ.

The raw Voltage data coming from the microphones has a sampling rate of 51.2 kHz to be able to capture frequencies from a broaden frequency spectrum. The measurement time is 10 s. The Voltage data is, after acquisition, processed and transformed into a pressure signal with the calibration coefficients. A correction to normalise the amplitude over the frequency band is applied as described in the microphone manual. With the corrected pressure signal, a frequency spectrum can be extracted by windowing the signal and performing a Fast Fourier Transform (FFT). From this spectrum, the pressure amplitude corresponding to the TS wave frequency can be extracted.

3.3.3 Pressure taps and wind tunnel data

Over the whole flat plate model, pressure taps are placed. The placement of the taps is given in figure 3.10. By measuring the pressure over the plate, the pressure gradients can also be evaluated, which is of influence to the stability of the boundary layer. Moreover, the assumed two-dimensionality of the flow over the plate can be evaluated from the taps at different spanwise locations. The data from the pressure taps is captured at a sampling rate of 2000 Hz. The time average over the total measurement time of 30 seconds gives the mean pressure development over the model.

If the wind tunnel is operational, some general data is acquired. The main input for the tunnel is the motor rpm, which is fixed to 1500 for all measurements. This results in a certain free stream velocity, which is measured with a pitot tube. There is also a measurement of temperature and this can be used to calculate the air density. This data can be logged to verify that the conditions remain similar throughout the experimental campaign.

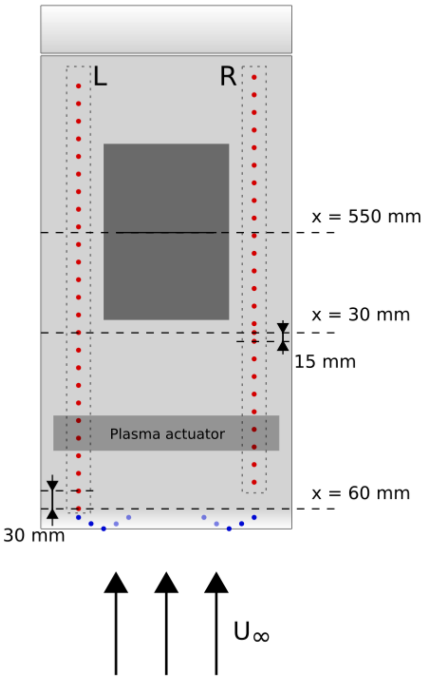

Figure 3.10: Locations of the pressure taps in the model, in red the taps at the flat part of the model and in blue the taps near the leading edge (light blue are placed on the back side of the plate)

As shown in figure 3.10, there are two categories of pressure taps, highlighted in red and blue. The red highlighted taps are the ones placed on the flat part of the model. These can be used for proving two dimensionality, because the taps have a different spanwise location. The pressure taps can be divided in a left group and a right group. The pressure taps highlighted in blue are located near the leading edge, these are not used in this study. However, these could be used to evaluate the stagnation at the leading edge.

3.3.4 Global field of view: Particle Image Velocimetry

In order to capture the development of the TS waves in the experiment, planar particle Image Velocimetry (PIV) measurements are used to capture the flow field in the global field of view as visualised in figure 3.12. PIV is a processing technique in which images of air flow are used. To visualise the flow, smoke particles are added. A laser sheet is constructed and the light of this laser is scattered by the smoke particles. This scattered light is captured by a camera. Two images are taken in quick succession and the captured images can be correlated with each other to find the instantaneous velocity field. In order to do this, the time between the two frames (Δt) has to be manually fixed.

The laser used for this experiment is a ND:YAG laser that emits green light (532 nm). This light is transformed into a light sheet with an array of spherical lenses and a cylindrical lens. The particles are small water-glycol mixture droplets. The camera type that is used for the experiment is the Imager sCMOS CLHS camera which has 2560×2160 pixels with a pixel size of 6.5×6.5 μm. To the camera, a lens with a focal length of 105 mm is attached. The camera and laser are automatically controlled by LaVision DaVis to remain in-sync with each other. With this program, the images are also processed to obtain the velocity vector fields. The top half of the domain is cropped to spare hard drive memory, so the eventual amount of pixels used in y-direction is 827.

The time between the acquisition of the two images of a single image pair is 30 μs. Usually, for this kind of experiments, a rule of thumb is used to get 12 pixels of displacement between the frames, one quarter of the initial interrogation window size [55] [56]. This leads to a Δt of about 15 μs. In this case, where the fluctuations inside the boundary layer are most important to investigate, the higher Δt is justified to capture more displacement caused by these fluctuations. This higher value of Δt improves the capturing of the TS wave. This is observed while conducting the experiment.

The displacement of the particles is calculated from the image pairs using the multi step interrogation algorithm [57]. The initial window size is 48×48 pixels and the process is followed until the final interrogation window size of 24×24 pixels with an overlap of 50% is reached. For this final interrogation window size, the vector spacing is 0.3 mm in both directions.

Two types of PIV measurements are performed: phase random and phase locked. For the random phase measurements the plasma actuator and the PIV system are not in-sync. In every image, a different phase of the TS wave is captured. For a sufficient amount of images, a standard deviation can give the amplitude development of the TS wave in streamwise direction.
For the phase locked measurements, the PIV system is in-sync with the plasma actuator. The timing between the plasma actuator excitation and the PIV capturing is fixed for each measurement case. In order to do so, the plasma actuator modulation frequency must be an integer times the PIV measurement frequency. The same phase of the TS wave is captured in every image, so a mean velocity field of the TS wave can be calculated. By varying the delay between the plasma excitation and the PIV capturing, a different phase of the wave is caught. A sweep through the phases can be performed to capture the full TS wave cycle.

The global field of view spreads in steamwise direction from 30 mm upstream of the resonator throat centre to 90 mm downstream. In wall normal direction, it reaches a height 20 mm from the surface. In order to get to this FOV with a sufficient resolution, two of the same cameras are used in series. Stitching the acquired images together leads to a wider view. A schematic of the global FOV is given in figure 3.12, the relevant parameters considering the PIV setup are given in table 3.4.

The reliability of the PIV data is evaluated in section 4.4.2 by checking the convergence and uncertainty. The convergence is calculated by looking at the deviation of a value calculated with a smaller data set to the value corresponding to the full data set. The uncertainty of the PIV data can originate from different sources. Here, only the time averaged uncertainty is evaluated as described in the paper by Sciacchitano & Wieneke [58].

This calculated time averaged uncertainty gives the range (U_x) around the measured value (V) in which the actual value is placed with a probability level of σ assuming a Gaussian distribution [59]. This is visualised with figure 3.11. The time-averaged uncertainty quantification is different for the mean and standard deviation and it can be calculated with equations 3.6 and 3.7 respectively [58].

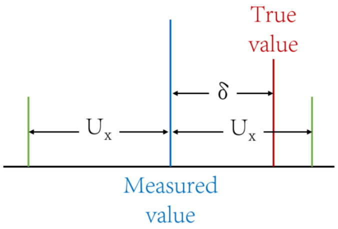

Figure 3.11: Visualisation of uncertainty definition in DaVis Adapted from [59]

$$U_{\bar{x}} = \frac{\sigma_x}{\sqrt{N}} \tag{3.6}$$

$$U_{\sigma_x} = \frac{\sigma_x}{\sqrt{2(N-1)}} \tag{3.7}$$

In equations 3.6 and 3.7, x is an arbitrary parameter.

Table 3.4: Global FOV setup parameters

Parameter description	**Value**
Lens focal length	105 mm
f#	5.4
Magnification factor	0.26
Amount of pixels	2560 × 2160
Pixel size	6.5 × 6.5 μm
Time between frames (Δt)	30 μs
Acquisition rate phase random	13.68 Hz
Acquisition rate phase locked	Dep. on f_{TS}
Amount of images phase random	2000
Amount of images phase locked	1000
Initial interrogation window size	48 × 48
Eventual interrogation window size	24 × 24
Overlap between windows	50%
Overlap between images	10 mm
Total amount of vectors (single cam)	214 × 70
Spacing between vectors	0.3 mm

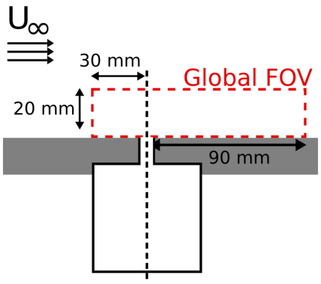

Figure 3.12: Schematic of global FOV

3.3.5 Local field of view: Particle tracking velocimetry

To investigate the interaction between the resonator and the passing TS wave in detail, a more zoomed-in image is created with the local FOV setup. The image is in streamwise direction centred around the resonator throat and it spans 15 mm to both sides. The viewing height normal to the surface is 20 mm, this is visualised in figure 3.13.

The image acquisition for this setup is similar to the process discussed for PIV on the global field of view, only the processing of the images is different. Particle tracking velocimetry (PTV) is used to calculate the flow fields from the image pairs. Contrary to PIV, PTV does not use correlation in interrogation windows, but it follows the tracks of the individual particles and projects these on a specified grid. The main advantage of PTV over PIV for this application is that the velocity near the wall is better resolved. This is especially important near the resonator throat. Individual particles near the wall can be traced in PTV, where a correlation will also be influenced by the reflections on the surface. This higher resolution near the wall is important for the evaluation of the resonator behaviour. In general, the velocity information is obtained with a finer spatial localisation, because each velocity vector corresponds to a single particle track [56].

In the PTV process, individual particles are identified in both images of the image pair. If the same particle is identified in both images, a track is found and these tracks can be fitted on a specified grid [56]. The approximated total amount of tracks found in the field of view is 55000. This means that there are 72 tracks found per squared millimetre at every time instance. The eventual grid is created from the binning process and every cell has a size of 6 × 6 pixels. This means that there are eventually 426 × 360 vectors with a spacing of 0.07 mm in the field of view.

In order to get to the zoomed-in, local field of view, a 200 mm macro lens is attached to the Imager sCMOS CLHS camera. The view is not cropped, so the full amount of pixels is used. The resulting magnification factor corresponding to this setup is 0.55, the time between two frames is $\Delta t = 15\ \mu$s. As also mentioned in section 3.3.4, this Δt is larger than usual for these applications [56]. However, with this higher value, the fluctuations inside the boundary layer can be captured more accurately. For this local field of view PTV, only phase locked experiments are performed. All relevant parameters for this setup are stated in table 3.5. The time averaged uncertainty can also be evaluated for the PTV measurements. This can be done using the same procedure as explained for the global field of view PIV measurements.

Table 3.5: Local FOV setup parameters

Parameter description	**Value**
Lens focal length	200 mm
f#	5.4
Magnification factor	0.55
Amount of pixels	2560 × 2160
Pixel size	6.5 × 6.5 μm
Time between frames (Δt)	15 μs
Acquisition rate	Dep. on f_{TS}
Amount of images	1000
Total amount of tracks	55000
Tracks per mm^2	72
Binning grid size	6 × 6 px
Total amount of vectors	426 × 360
Spacing between vectors	0.07 mm

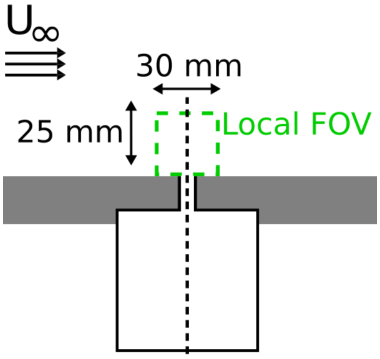

Figure 3.13: Schematic of local FOV

4 RESULTS & DISCUSSION

As described in the previous chapter, three different techniques are used to answer the main research questions. In this chapter, the results are given and discussed per subject. First, a relation is shown between pressure and v-velocity at the wall that is needed for TS wave damping. Next, the predicted influence of the Helmholtz resonator on the TS wave is given and this behaviour is validated with the experimental data. Moreover, the reliability of the experimental data is evaluated based on convergence and uncertainty. At the end of this chapter, some side steps will be taken to get to a physical framework that defines the interaction between a TS wave and a Helmholtz resonator.

The data given in this chapter is mostly given in non-dimensional form. For the streamwise location x, it means that this is normalised with the displacement thickness at the position of the resonator x_r. The resonator location is also chosen as the zero location. The streamwise location will be denoted with $\tilde{x}$ and can be calculated using equation 4.1. For the wall-normal position, non-dimensionalisation is done with the same length scale ($\delta^*|_{x_r}$), as given in equation 4.2. The velocity components u and v can be non-dimensionalised with the free stream velocity, which is constant throughout the study. The same free stream velocity can be used, together with the air density ($\rho\ U_\infty^2$) to get pressure in non-dimensional form. The frequency is dimensional throughout the study to remain the frequency scale the metamaterial is used on.

$$\tilde{x} = \frac{x - x_r}{\delta^*|_{x_r}} \tag{4.1}$$

$$\tilde{y} = \frac{y}{\delta^*|_{x_r}} \tag{4.2}$$

4.1 RESONANT FREQUENCY

The main property of the Helmholtz resonator used in this study is its resonant frequency. The behaviour of the resonator at or near this frequency determines what the interaction with the passing wave will be. In the first part of the methodology chapter, the resonator geometry is designed. In section 3.3, the thee different resonator configurations are presented. Here, the resonant frequencies of the designed configurations are evaluated to see whether the intended specifications are reached. The resonant frequency is investigated experimentally by monitoring the pressure fluctuations just outside the throat and inside the resonator cavity with microphones in quiescent conditions. A transfer function between the microphone inside and the microphone outside can be made in terms of dividing the absolute measured pressure in the frequency domain.

The experimental transfer function can be compared with the numerical results from a thermoviscous acoustics simulation in COMSOL. The setup for this simulation is given in section 3.1.1. A pressure probe is placed just above the resonator throat and in the centre of the resonator cavity in the numerical domain. For this thermoviscous acoustics simulation, a frequency sweep was performed from 100 to

400 Hz. In the experimental setup, a loudspeaker exerting white noise was used to obtain the pressure transfer function. This white noise has a broaden band of frequencies with an equal amplitude which makes it a good tool for this resonance evaluation. The transfer functions calculated from the thermoviscous acoustics simulation and the experimental pressure measurements are given in the frequency spectrum in figure 4.1.

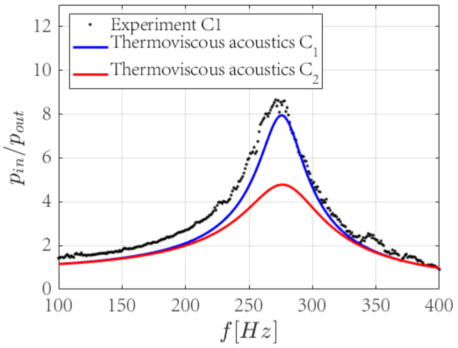

Figure 4.1: Transfer function between pressure inside and outside the Helmholtz Resonator

In this figure, it can be seen that there is only a small deviation between the numerical and experimental results for configuration C_1. The experimental curve shows a slightly higher peak at a frequency which is about 5 Hz lower than the numerical peak. The peak in the experimental data also seems to be wider. In general, the two curves coincide appropriately to make a valid comparison between the numerical and experimental results throughout this study.

A possible explanation for the small discrepancy between the numerical and the experimental curve is the two dimensionality of the experimental model. The 2D Helmholtz resonator has a slot as its throat (as explained in section 3.3) where in general a 3D Helmholtz resonator has a round hole. The losses in the throat can be lower because of the slotted opening which could make the peak in figure 4.1 wider. Another possible explanation considers the geometry of the produced throat and cavity parts. The sizes could differ slightly from the nominal design due to manufacturing limitations.

In figure 4.1, the red line represents the pressure ratio determined from a thermoviscous acoustics simulation for resonator configuration C_2. The peak of the curve is at a lower amplitude than the peak for configuration C_1. However, the peak frequency is approximately the same for both configurations. Due to the small 0.4 mm cavity at the top of the throat, more friction is expected if air passes through. This friction causes losses which probably lead to the lower amplitude for this configuration. Normally, this would also change the resonant frequency, but because the throat length is reduced to a total of 4 mm (instead of 5mm), the resonant frequency shift has been counteracted.

From the results presented in this section, the conclusion can be drawn that a valid comparison can be made between the experimental and numerical data. The numerically and experimentally obtained resonant frequency curves corresponding to resonator configuration C_1 show only minor differences. Resonator configuration C_2 has a similar resonant frequency as configuration C_1. This opens the possibility to make a comparison between the different resonator configurations, although the peak heights in figure 4.1 do not match.

4.2 PRESSURE-VELOCITY PHASE RELATION

From different studies in acoustics (for example [10]), the acoustic impedance is identified as an important factor in characterising an acoustic metamaterial and their damping properties at a certain frequency. This is also discussed in section 2.2.2. Impedance, denoted with Z can be seen as a complex resistance in the frequency domain and it can be calculated by dividing the complex acoustic pressure by the complex acoustic velocity. In the study by Zhao et al. [46] it was shown that an impedance matched surface, where Z is purely real and has a magnitude of -1, suppresses the instability well. However, it was also shown that an impedance-near-zero surface can have even better wave suppressing properties. The driver behind an impedance matched surface is that it absorbs the wave energy. An impedance-near-zero surface suppresses the passing wave by reflecting a similar wave with an 180° phase change to get suppression by superposition [46]. This wall controller property of exerting another wave, exactly out of phase with the passing wave was also found in boundary layer stability control methods [24] [27] [28].

Where acoustic impedance includes the complex acoustic velocity and pressure, a similar method could be used for the pressure of the TS wave and the velocity coming from an acoustic metamaterial. This can be captured in an amplitude/phase relation between p and v. In this section, it is investigated whether this amplitude/phase relation between pressure and velocity is also an important factor for the interaction between an acoustic metamaterial and TS waves. This investigation is performed using the modified version of the PSE solver (section 3.1) and the active throat linearised Navier-Stokes simulation (section 3.2).

The TS wave pressure at the wall can be read while solving the stability analysis using the adjusted PSE. The v-velocity at the wall can be imposed based on this pressure. As described in methodology section 3.1, the pressure amplitude is multiplied with a factor A_{BC} and a phase angle constant ϕ_{BC} is added to the phase angle of the pressure to construct the v-velocity boundary condition at the wall. The N-factor is determined at $\tilde{x} = 100$ and normalised with the N-factor determined from a baseline configuration without inhomogeneous boundary condition. The N-factor development as calculated with the adjusted PSE for three cases is given in figure 4.2a. These three cases consist of a baseline, one with $A_{\mathrm{BC}} = 2$ and $\phi_{\mathrm{BC}} = 0°$ and one with $A_{\mathrm{BC}} = 2$ and $\phi_{\mathrm{BC}} = 180°$. To see what the influence of a v-velocity boundary condition at the wall is. A sweep over phase angles ϕ_{BC} for two different values of A_{BC} gives the influence of the boundary condition on the stability. This is presented in in figure 4.2b. The N-factor is evaluated at $\tilde{x} = 100$ from the resonator location, denoted with the red dashed line in figure 4.2a. The normalised downstream N-factor used in figure 4.2b can be calculated with equation 4.3.

$$\tilde{N}_{\mathrm{ds}} = N_{\tilde{x}=100} / N^{\mathrm{Baseline}}_{\tilde{x}=100} \tag{4.3}$$

From figure 4.2a, two observations can be made. The effect of the imposed v-velocity boundary condition at $\tilde{x} = 0$ is only a local effect. The N-factor jumps or drops at the particular boundary condition location and further downstream, the same trend is followed as in the baseline configuration. Besides that, the conclusion can be drawn that according to the PSE calculation, the TS wave can be suppressed if its pressure and the v-velocity boundary condition are in-phase. This is further strengthened by looking at figure 4.2b. The most optimal suppression is found when $\Delta\phi = \phi(v) - \phi(p) = -4.5°$. If the TS wave pressure and the boundary condition v-velocity have a phase difference outside of $-88.8° \leq \Delta\phi \leq 90.4°$, the N-factor downstream is reduced compared to the baseline. If this condition is not satisfied, the TS wave is amplified by the boundary condition and the N-factor downstream is higher than the baseline. Figure 4.2b shows that there are strict turning points at $\Delta\phi = -88.8°$ and $\Delta\phi = 90.4°$ on which no difference with the baseline can be

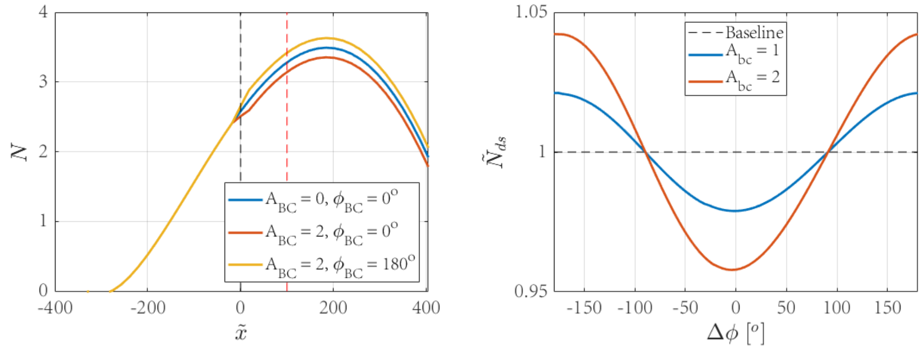

(a) N-factor development calculated with PSE with inhomogeneous boundary conditions for a baseline case and two imposed boundary conditions

(b) Effect of the inhomogeneous v-velocity boundary condition on the N-factor 60 mm downstream

Figure 4.2

noticed. Furthermore, the amplitude of the v-velocity boundary condition does not influence the qualitative amplification or suppression, it only influences the magnitude of this effect.

In order to validate this amplitude/phase relation between the TS wave pressure at the wall and an imposed v-velocity boundary condition, the active throat linearised Navier-Stokes simulation can be used as described in methodology section 3.2. For this numerical simulation, the cavity of the Helmholtz resonator is omitted and the bottom of the throat has an imposed v-velocity boundary condition. The phase of this boundary condition is relative to the TS wave introduction forcing. The results of a full 360° sweep can also give the full phase relation between the pressure above the throat ($\tilde{y} = 2$) and the velocity in the throat centre. The TS wave amplitude is extracted using the standard deviation of the v-velocity perturbation at $2\delta^*$ at $\tilde{x} = -92$ and $\tilde{x} = 92$ with the active v-velocity boundary condition as described in section 3.2. The effect of the boundary condition phase relation with the passing TS wave pressure as calculated using the linearised Navier-Stokes simulation is shown in figure 4.3.

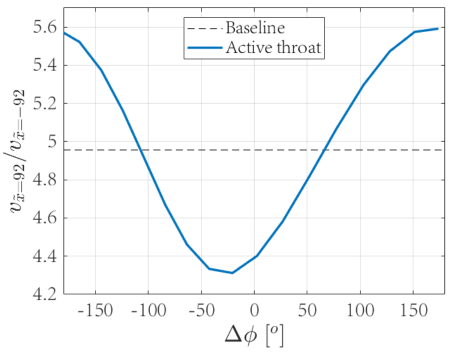

Figure 4.3: Effect of the inhomogeneous v-velocity boundary condition on the TS wave amplitude 100 mm downstream as calculated from linearised Navier-Stokes simulations

From figure 4.3 and especially a comparison with figure 4.2b, the conclusion can be drawn that the phase relation between the pressure of the TS wave and the wall controller velocity is an important factor in the suppression/amplification of TS waves. This is similar to the importance of impedance in acoustics. Figure

4.2b suggests that there is not a perfectly symmetrical distribution centred around $\Delta\phi = \phi_{v_{\text{BC}}} - \phi_{p_{\text{TS}}} = 0°$, but there is a slight shift to the left. A similar shift is seen in figure 4.3, but for the results from the linearised Navier-Stokes simulation, this shift is larger. The resolution in phase angles for the active throat linearised Navier-Stokes simulation is limited, because of the high computational costs. It is unpractical to resolve the active throat simulation for an equal amount of phase angles as the adjusted PSE calculation. The slight asymmetrical shift in figure 4.3 can therefore not be investigated to its smallest detail. However, the point of optimal attenuation is found at $\Delta\phi = -21°$ and the turning points that coincide with the baseline are located at $\Delta\phi = -106°$ and $\Delta\phi = 64°$. This seems to be contradictory to the statement that the relation is almost symmetrical around $\Delta\phi = 0°$. However, the determination of $\Delta\phi$ in the active throat linearised Navier-Stokes simulation is dependent on the evaluation points of v and p. Therefore, it could be inconvenient to rely on the values of $\Delta\phi$ from this simulation. All in all, some discrepancies are found between the active throat results and the adjusted PSE results. However, the general outcome in terms of amplitude/phase relation between pressure and velocity and its importance for TS wave attenuation remains the same.

4.3 PREDICTED INFLUENCE RESONATOR ON TS WAVE STABILITY

In the previous section, the wall controller property needed for TS wave attenuation is specified. The assumption is made that the only wall controller property of importance for TS wave stability is this amplitude/phase relation between the TS wave pressure and the v-velocity boundary condition. With this assumption, the influence of a Helmholtz resonator to the stability can be predicted. This is done with the adjusted PSE solver coupled with the thermoviscous acoustics simulation, which is described in section 3.1.1. If figure 3.4b from this methodology section is recalled, the amplitude/phase relation computed with this simulation can be evaluated. The amplitude relation $|v|/|p|$ gives a clear peak at the resonance frequency of the resonator ($f \approx 300$ Hz). At that frequency, the phase difference between velocity and pressure $\Delta\phi = \phi(v) - \phi(p)$ crosses 180°.

The phase relation corresponding to the resonator is again given in figure 4.4. In this figure, the turning points from the adjusted PSE with inhomogeneous boundary condition calculation are added as discovered in section 4.2. The phase difference between the pressure and velocity evaluated at the top of the throat, as extracted from a thermoviscous acoustics simulation, will not go out of the bounds set by the black dashed lines within the tested frequencies. Therefore, according to a combination of the adjusted PSE and the amplitude/phase response of a single Helmholtz resonator, the resonator will only amplify the passing TS wave.

The influence of the phase difference to the stability is nearly symmetrical around zero degrees, as discussed in section 4.2. If the assumption is made that the effect is symmetrical and that the turning points are at ±90°, the magnitude of suppression depends on two parameters: the phase difference between the velocity and pressure and the ratio between the pressure and velocity amplitudes. This can be captured with a performance metric P. The formula to calculate the performance is given below in equation 4.4. A positive performance means that the TS wave is amplified.

$$P = (-90° + |\Delta\phi|)\,\frac{|v|}{|p|} \qquad \text{With: } \Delta\phi = [-180°, 180°] \tag{4.4}$$

The performance of a Helmholtz resonator based on the thermoviscous acoustic calculation can be evaluated over a range of frequencies. This is shown in figure 4.5. It

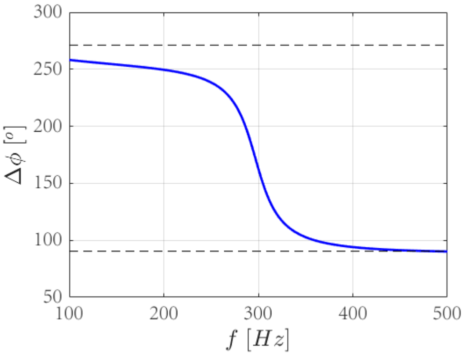

Figure 4.4: Phase response of the resonator calculated with the thermoviscous acoustics calculation including turning point boundaries

can be seen that only TS wave amplification is expected and that the magnitude of amplification increases when the frequency reaches the resonant frequency of the resonator.

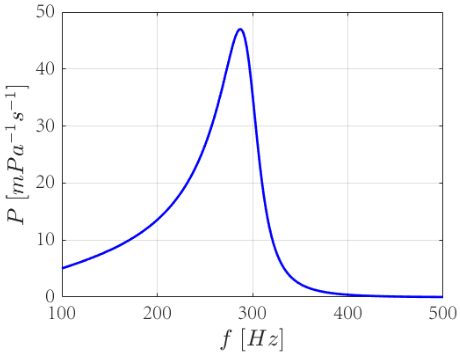

Figure 4.5: Performance of the resonator as calculated with equation 4.4

The amplitude/phase response of the resonator calculated from the thermoviscous acoustics simulation can also be used in the adjusted PSE calculation to calculate the influence on the TS wave stability as described in section 3.1.1. The magnitude of the TS wave pressure at a particular x-location is dependent on the stability of the wave. A higher TS wave pressure also leads to a stronger response from the resonator, so the amplitude/phase relation given in figure 3.4b does not include every aspect of the behaviour.

As a result of the coupling between the adjusted PSE and the thermoviscous acoustics simulation, the influence in terms of N-factor of the resonator can be evaluated. For a TS wave frequency of 290 Hz and including the presence of the resonator with a multiplication factor F_{BC} of 1, the N-factor development is calculated. This is given in figure 4.6a. For a sweep over frequencies, the N-factor at $\tilde{x} = 100$ gives information about the effect of the resonator in the frequency domain. The influence given in figure 4.6b includes both the performance (P) and the stability of the TS wave and can be represented by $\tilde{N}_{\mathrm{ds}}$, which is calculated with equation 4.3. In order to create this figure from the solutions of the adjusted PSE solver, a multiplication factor F_{BC} of 0.5 is used to assure solver stability for all frequencies.

Figure 4.6a shows that the modelling of the resonator using the thermoviscous acoustics simulation leads to a relatively large jump in N-factor. This means that, for this TS wave frequency (290 Hz), the resonator amplifies the TS wave locally

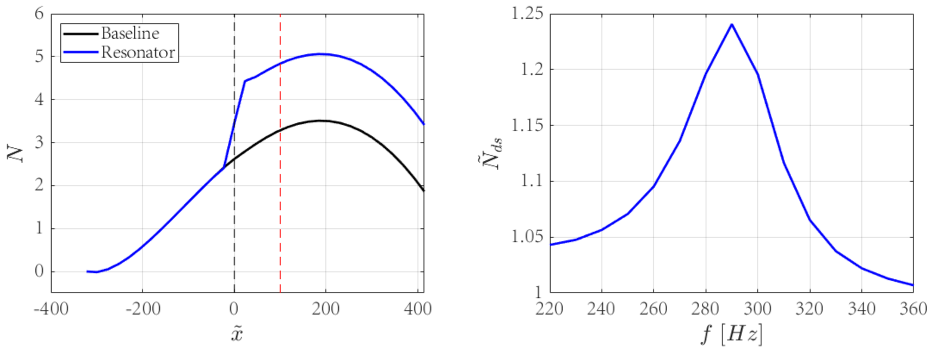

(a) N-factor development of a TS wave with a frequency of 290 Hz

(b) Influence of the resonator to the downstream N-factor

Figure 4.6: Coupling PSE and resonator amplitude/phase response from the thermoviscous acoustics calculation

with respect to a baseline without modelled resonator. For a range of frequencies, the relative jump in N-factor downstream of the resonator location is given in figure 4.6b. The result presented in this figure couples the performance (P) from figure 4.5 to the TS wave stability. The lines in figures 4.6b and 4.5 follow a similar path. The main discrepancy between the two is that the line in figure 4.6b descents more gradually for frequencies higher than the peak frequency. This is caused by the TS wave pressure amplitude driving the Helmholtz resonator, which peaks at $f_{\text{TS}} \approx 340 Hz$ according to figure 3.2a. Figure 4.6b gives a more complete overview of the predicted influence of the modelled Helmholtz resonator to the TS wave development than figure 4.5. However, the conclusion that the TS wave will only be amplified by the resonator is unchanged.

With the results presented in this section, the conclusion can be drawn that the Helmholtz resonator will only amplify the TS wave because of the amplitude/phase relation between pressure and velocity. This hypothesis originates from the results of the adjusted PSE solver with arbitrary inhomogeneous boundary conditions and the linearised Navier-Stokes simulation with the active throat from section 4.2. This is supplemented with the adjusted PSE solver results coupled with the thermoviscous acoustics simulation presented in this section. The magnitude of amplification is based on the TS wave frequency in terms of stability and the frequency difference between the TS wave and the resonant frequency of the Helmholtz resonator.

4.4 CONVERGENCE AND UNCERTAINTY OF EXPERIMENTAL DATA

The hypothesis that the TS wave will only be amplified by the presence of the resonator is tested experimentally. Moreover, the influence of the frequency difference between the TS wave and the resonant frequency of the Helmholtz resonator is further investigated. In a wind tunnel test, data is gathered via pressure taps, microphones and by using PIV or PTV as described in section 3.3. In order to draw reliable conclusions from these experimental methods, the uncertainty and convergence need to be proven.

In this section, the convergence of the microphone measurements and PIV/PTV data will be evaluated. Besides that, the uncertainty of the PIV/PTV measurements is investigated with the method described in section 3.3.4. The boundary layers used in the different numerical and experimental methods are compared to each other. Furthermore, the assumed two-dimensionality of the boundary layer is evaluated. Eventually, the consistence of the TS wave entering the area of interest is investigated.

4.4.1 Convergence of microphone data

As described in section 3.3.2, three microphones are installed in the model. To ensure that the measurement time and sampling frequency are sufficient to get a reliable result, the convergence is investigated in this section. This is done by evaluating the pressure amplitude coming from the processed microphone measurements corresponding to the specific TS wave frequency. The throat part configuration for this convergence test is C_1. The total measurement time is 10 seconds, FFT is performed on windows of 1 second with a 50% overlap. So eventually $N_{\text{Win}} = 19$ windows are used for averaging to compute the amplitude. The pressure amplitude convergence is determined as given in equation 4.5 and the result for the three microphones is given in figure 4.7.

$$\tilde{p}_{\text{mic}} = \frac{\frac{1}{n}\sum_{i=1}^{n} p_i}{\frac{1}{N_{\text{Win}}}\sum_{i=1}^{N_{\text{Win}}} p_i} \cdot 100\% \tag{4.5}$$

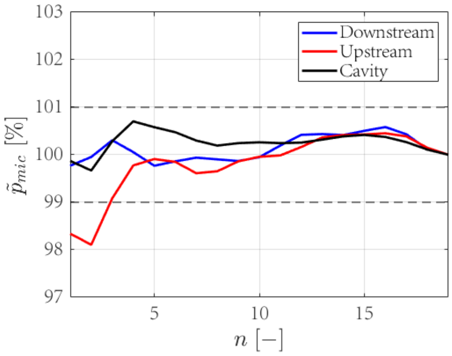

Figure 4.7: Convergence of microphone data for $f_{\text{TS}} = 290$ Hz and throat configuration C_1

From figure 4.7, it is clear that there is already convergence within reasonable bounds (±1%) from the third window on. After that, the three lines representing the three microphones come closer to each other but they do not exactly match the 100% line between $n = 12$ and $n = 18$. Since this is the case for all three microphones, this could have different causes than a lack of convergence. While performing the experiments, the observation was made that the TS wave entering the area of interest does not always have the same magnitude. The TS wave could therefore be inconsistent in strength between the different test cases, this is more elaborately discussed in section 4.4.5.

All in all, from figure 4.7 the conclusion can be drawn that the current settings with a measurement time of 10 seconds and a sampling rate of 51.2 kHz give sufficient convergence. This means that the data from the microphone measurements form a reliable source of information for the evaluation of the TS wave amplitude.

4.4.2 Convergence and uncertainty of PIV/PTV data

Besides the microphone measurements, the convergence of the PIV/PTV data also needs to be investigated to evaluate the reliability of the measurement data. This is done in two ways. First the convergence of the acquired data to the amount of taken images is evaluated. Next, the uncertainty of the used standard deviation or average velocity field is investigated for the full range of taken images. This investigation can be performed for both the global field of view PIV and local field of view PTV data.

PIV: Global field of view

The PIV measurements on the global field of view include phase random and phase locked cases, as described in section 3.3.4. A phase random case is used to evaluate the convergence of the captured boundary layer. The convergence evaluation for this particular test, is representative for all PIV measurements in this study. For the phase locked measurement, the convergence test is expanded to include the convergence the velocity of a certain point in the domain.

First, the convergence of the boundary layer integral quantities is evaluated for the experimental measurements for the global field of view. This includes the displacement and momentum thickness, denoted with δ^* and θ respectively. The formula to calculate the displacement thickness was already given in equation 3.5, the momentum thickness can be calculated using equation 4.6. The two points used for the convergence analysis of the boundary layer integral quantities are taken at $x = -20$ mm and $x = +50$ mm. These locations are dimensional for this convergence test, because the normalisation parameter is based on the momentum thickness. For the random phase measurements, the amount of image pairs that are taken by both cameras is 2000 per test case. The convergence can be evaluated by calculating the momentum and displacement thickness using less image pairs and comparing that to the integral quantities calculated using full amount of acquired images. This is done by calculating a percentage difference from δ^* and θ calculated from the full data set. In figure 4.8, convergence plots are given for two streamwise points corresponding to a test case with $f_{\mathrm{TS}} = 290$ Hz and throat configuration C_{base} and C_1.

$$\theta = \int_0^H \frac{u(x,y)}{U_\infty}\left(1 - \frac{u(x,y)}{U_\infty}\right) dy \tag{4.6}$$

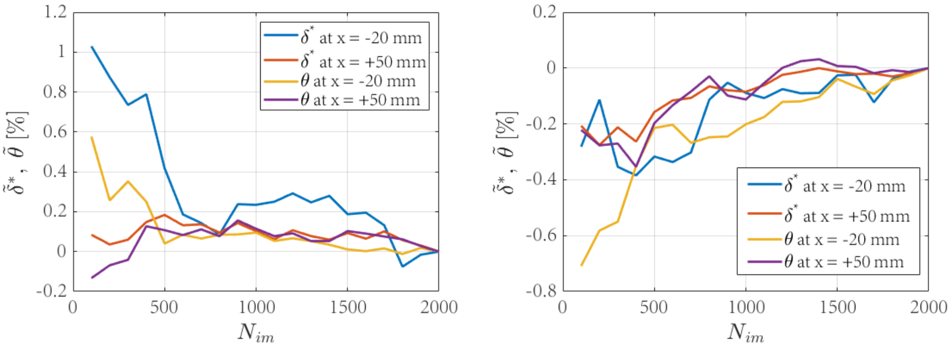

(a) Resonator configuration C_{base} **(b)** Resonator configuration C_1

Figure 4.8: Convergence to the amount of taken images of δ^* and θ at two streamwise locations for the phase random tests with $f_{\mathrm{TS}} = 290$ Hz

The lines in figure 4.8 representing the convergence of the boundary layer integral quantities show that convergence is reached within bounds of ±1% already from the smallest data set on. Most lines converge further to reach a range of ±0.2% for a data set of more than 1000 image pairs. The largest fluctuation in convergence is visible for the momentum thickness at $x = -20$ mm for configuration C_{base}. However, because the relative fluctuation in percentage is still minor, this will not affect the reliability of the measurement data. From figure 4.8, the conclusion can be drawn that the boundary layer thickness is accurately captured with a data set of 1000 or more image pairs.

For the phase locked measurements, the amount of image pairs is 1000. The convergence of this data is two-fold. On one hand, the boundary layer must be captured correctly and the integral quantities given above can verify that. On the other hand, the TS wave velocity convergence at a certain point in space gives a good indication on whether the TS wave is captured correctly. This TS wave velocity can only be investigated by extracting a case without an induced TS wave. The spatial points for this convergence test are taken at $\tilde{x} = 10$ and $\tilde{x} = 24$ at $\tilde{y} = 2$ for $f_{\text{TS}} = 290$ Hz. The throat configuration is C_1 and phase angle of the TS wave is $\phi_{\text{TS}} = 0°$. For this phase angle, the v-velocity of the TS wave has a positive peak at the streamwise location of the resonator. The evaluation points are highlighted in figure 4.9. The convergence to the amount of images taken for the calculation of the average velocity for both points is given in figure 4.10. The velocity convergence at a point is denoted with $\tilde{v}_p$ and this can be calculated with equation 4.7.

$$\tilde{v}_p = \frac{v_p|_{N=N_{\text{im}}} - v_p|_{N=1000}}{v_p|_{N=1000}} \cdot 100\% \tag{4.7}$$

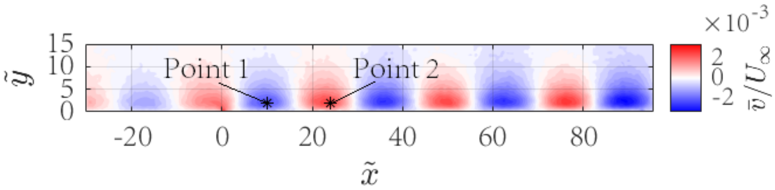

Figure 4.9: Points used for velocity convergence check

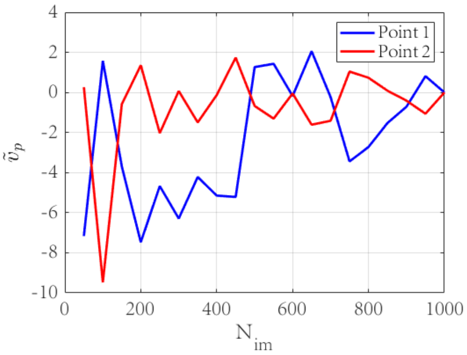

Figure 4.10: Convergence of velocity to the amount of images takes to determine the average for $f_{\text{TS}} = 290$ Hz and configuration C_1

As visualised in figure 4.9, the points are approximately located in the centre of a negative and a positive v-velocity part of the TS wave. The convergence in a percentage of the reference case ($N_{\text{im}} = 1000$) in figure 4.10 shows that there is a fluctuation in the point velocity, also if the amount of images reaches its maximum. This fluctuation is larger for the convergence at point 1 than at point 2. A possible explanation for this fluctuating behaviour of the convergence is the inconsistency of the TS wave strength entering the area of interest. This was also mentioned for the convergence of the microphone measurement data in section 4.4.1. This effect is more elaborately discussed in section 4.4.5. Moreover, there will always be a certain uncertainty in the velocity field calculated by using PIV. This could also influence the convergence of the velocity at a certain point.

Despite the unwanted fluctuating convergence of the velocity, the global PIV phase locked data can still be useful for the qualitative analysis of the interaction between the Helmholtz resonator and the TS wave. A quantitative analysis needs a normalisation with a TS wave amplitude upstream of the resonator location to account for the inconsistency of the strength of the incoming TS wave. The disadvantage of this required normalisation is that the absolute information needed for a direct comparison is lost. This precludes, for example, a direct comparison between the PIV and microphone measurements.

Besides the convergence, an important factor in the reliability of the experimental results is the uncertainty of the PIV data. The uncertainty quantification is performed using the method described in methodology section 3.3.4. In this study, only the time averaged uncertainty is taken into account. The uncertainty can be visualised in a 2D contour plot. For the random phase measurements, the computed standard deviation is used to determine the TS wave amplitude, so in this case, the uncertainty of the standard deviation of the v-velocity will be evaluated. For the phase locked cases, the mean v-velocity is the relevant parameter. Therefore, the uncertainty of the mean v-velocity is evaluated for the phase locked measurements and the uncertainty of the v-velocity standard deviation is given for the phase random data. The corresponding contour plots are given in figures 4.11 and 4.12.

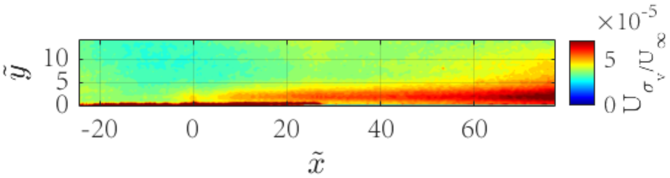

Figure 4.11: Time-average uncertainty of the random phase case with $f_{TS} = 290$ Hz and configuration C_1

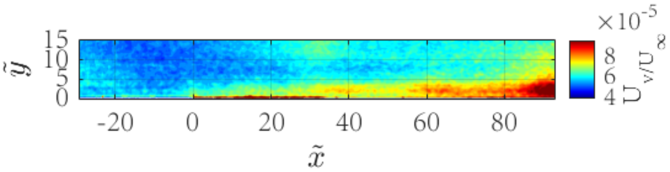

Figure 4.12: Time-average uncertainty of the phase locked case with $f_{TS} = 290$ Hz, $\phi = 0°$ and configuration C_{base}

In both figures (4.11 and 4.12) it can be seen that the highest uncertainty values are present inside the boundary layer and near the wall. Besides that, the uncertainty in the boundary layer seems to increase for a higher value of $\tilde{x}$ in both figures. In the free stream, the uncertainty values are low because of the minor disturbances in this region. In order to get the uncertainty values for the phase locked test in figure 4.12, the standard deviations of the specific TS wave case and a case without induced TS wave are added to each other. The uncertainty is reflected, because a mean velocity field is obtained by subtracting this no plasma case.

In terms of convergence, the standard deviation converges faster because the denominator in equation 3.7 is higher than the one in 3.6. However, the standard deviation is expected to be lower for the phase locked cases because the same phase of the TS wave is captured in every image. This justifies that the amount of images needed for the phase locked cases are half the amount of images taken for the phase random cases. Also, between the two cameras, there are some differences, these can be caused by some vibrations or a slight lack of focus for one of the two cameras.

For the uncertainty quantification, the standard deviation at $y = 2\delta^*$ can be evaluated with a band of uncertainty values. This is shown in figure 4.13a for $f_{\text{TS}} = 290$ Hz and configuration C_1. Since the uncertainty of the standard deviation is directly dependent on the standard deviation itself according to equation 3.7, the green band becomes wider for a higher value of σ_v/U_∞. The width of the band is relatively small, especially around the resonator x-location, such that it can capture the influence of the resonator to the TS wave accurately and repeatably.

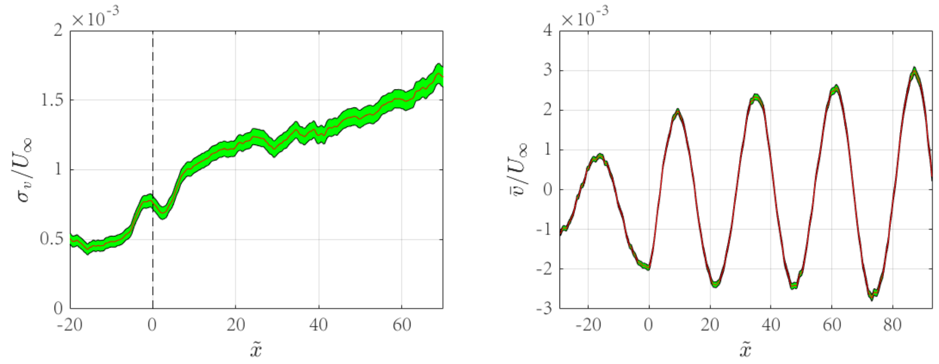

(a) Time-average uncertainty band around standard deviation determined at $y = 2\delta^*$ for $f_{\text{TS}} = 290$ Hz and configuration C_1

(b) Time-average uncertainty band around mean v-velocity determined at $y = 2\delta^*$ for $f_{\text{TS}} = 290$ Hz and configuration C_{base}

Figure 4.13: Time-average uncertainty of local field of view PTV measurements

Similar to the evaluation of the standard deviation for the phase random case, the v-velocity can be evaluated at $y = 2\delta^*$ for a phase locked case. A sine wave that is growing in amplitude is expected and also shown by the red line in figure 4.13b. The uncertainty band as calculated with equation 3.6 is narrow. This implies that the shape and values corresponding to the TS wave v-velocity are reliable.

All in all, for the global field of view PIV measurements, the velocity data at certain points in the domain are not fully converged. This is probably caused by some inconsistency of the TS wave strength, when it enters the area of interest This was already discussed for the convergence of the microphone measurements and will be more elaborately analysed in section 4.4.5. To account for this, normalisation with an upstream value is needed to make a comparison between cases. In terms of uncertainty, there is some band around the measured value to take into account. However, this band is relatively narrow. The uncertainty is sufficiently small to capture the relevant information about the TS wave accurately. The conclusion can be drawn that the global field of view PIV results are reliable to use in the investigation to the influence of the resonator to the TS wave stability.

PTV: Local field of view

Similar to the global field of view PIV data, the convergence and uncertainty of the local field of view PTV data can be evaluated to investigate the reliability and accuracy of these results. For this local FOV setup, only phase locked measurements are performed, so the convergence will be based on the velocity at a certain point in the domain to the amount of images used to calculate this.

PIV gives out a vector at every interrogation window for every time step. PTV, on the other hand, only outputs a vector if a particle track is found at a certain point. This track is then mapped on a certain grid. A vector might not be found for every point in the domain for every time step, so there is an effective amount of samples used for the statistical calculations per vector. This could lead to some non-uniform convergence. The convergence to the total amount of samples, therefore only gives an indication of the actual convergence at a point in space.

The convergence study is performed for the v-velocity to the amount of samples taken to calculate the average. This is done for a case with $f_{\mathrm{TS}} = 290$ Hz, $\phi = 180^\circ$ and resonator configuration C_1. A clean case without manually introduced TS wave is subtracted to obtain the TS wave from the field. The amount of samples taken for this subtraction case is fixed to the maximum of 1000. At two points, the velocity is evaluated: at the throat exit ($\tilde{x} = 0$, $\tilde{y} = 0.1$) and near the maximum of the TS wave v-velocity above the throat ($\tilde{x} = 0$, $\tilde{y} = 2$). These points are chosen because of their usage section 4.6 to evaluate the interaction between the resonator and the TS wave. The velocity is averaged over a small window around this point to reduce noise. The convergence evaluation for this specific case is representative for the other PTV measurement data. The convergence of the velocity to the amount of images taken to compute the average is given in figure 4.14.

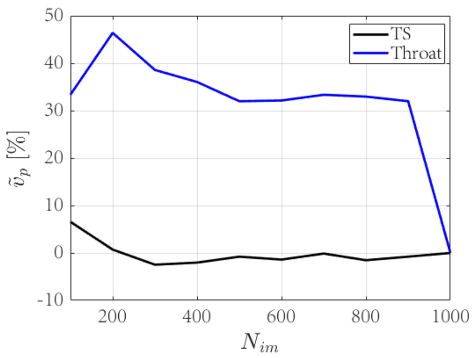

Figure 4.14: Convergence of v-velocity at two points in space to the amount of images for a case with $f_{\mathrm{TS}} = 290$ Hz, $\phi = 180^\circ$ and resonator configuration C_1

Figure 4.14 shows that the v-velocity at $\tilde{y} = 2$, corresponding to the TS wave, is already predicted within bounds of ±10% from the smallest value of N_{im} on. The TS wave velocity converges slowly to the value that is reached at $N_{\mathrm{im}} = 1000$. The throat exit velocity on the other hand does not show this behaviour. Sufficient convergence does not seem to be reached within the available data set. From values of N_{im} higher than 500 on, the obtained velocity is within 35 % of the final velocity. With the inclusion of the last 100 images in the particle tracking process, a relatively large deviation is found for the determination of $\tilde{v}_p$. Although PTV is less prone than PIV to inhomogeneous seeding [56], which can be expected at the throat exit location, insufficient convergence is still observed. This can also be explained by non-uniformity in the convergence, as there is only a small amount of seeding particles expected in the throat exit region. This is caused by the viscous effects in the boundary layer. The measured velocity value at the throat exit can therefore only be used qualitatively to demonstrate an effect, but the quantitative value is not fully reliable. This affects the results presented in section 4.6.

The convergence of point velocities at $y = 2\delta^*$ in the global field of view suffered from the inconsistency of the incoming TS wave strength. The same inconsistency is expected for the measurements with the zoomed-in setup. However, the scale in $\tilde{v}_p$ is too large to capture this in figure 4.14. The fluctuations in the global field of view velocity convergence (figure 4.10) have an amplitude of a few percents, where the fluctuations in figure 4.14 can reach tens of percents.

In terms of uncertainty of the local field of view PTV measurements, the same routine (equations 3.6 and 3.7) is used as described for the uncertainty in the global field of view in section 3.3.4. This uncertainty is only a time-averaged statistical quantity [58]. For this zoomed-in setup, the mean velocity over the images is used for further processing, so the uncertainty of the mean v-velocity is given in figure 4.15. Next to the uncertainty in the whole field of view, the v-velocity fluctuation at $y = 2\delta^*$ is given including an uncertainty band.

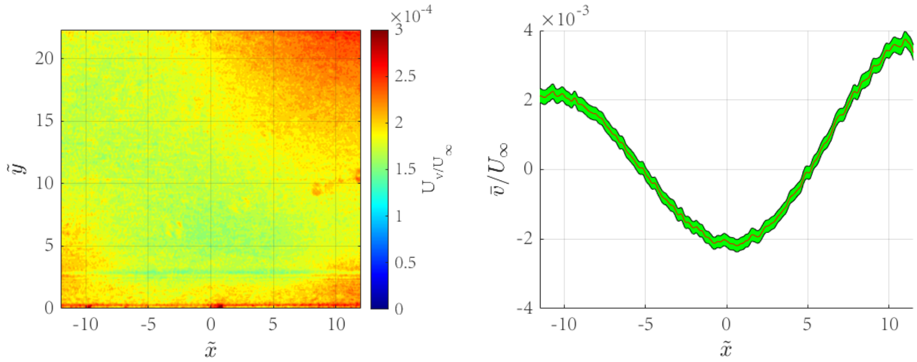

(a) 2D Contour plot of local field of view

(b) Average v-velocity at $y = 2\delta^*$ with uncertainty band

Figure 4.15: Time-average uncertainty of local field of view PTV measurements for a case with $f_{TS} = 290$ Hz, $\phi = 180°$ and resonator configuration C_1

The band around the fluctuating velocity shown in figure 4.15b is relatively constant over the whole domain. This is also visible in figure 4.15a, in which only in the corners, the uncertainty rises. In general, the time-average uncertainty for this local field of view PTV is larger than for the global field of view PIV data. The uncertainty very close to the wall in figure 4.15a is high, this can be caused by some reflections at the wall or a lack of particles there. However, this uncertainty is not propagated into the domain. The higher uncertainty at the wall can also influence the convergence of the throat exit velocity as given in figure 4.14.

It must be noted that the uncertainty and convergence for the PTV data are based on the amount of image pairs used in the calculation. As mentioned at the beginning of this section, the nature of the PTV technique could lead to an inhomogeneous convergence, because not every processed image pair leads to a full field of velocity vectors. However, from the convergence and uncertainty presented in this section, the conclusion can be drawn that most of the information extracted from the PTV measurements is reliable. Only in locations (very) close to the wall, convergence was not reached within the available data set. Moreover, this PTV data can also suffer from the inconsistency of the TS wave strength when entering the field of view, similar to what was seen for the microphone and PIV measurements. All in all, the local field of view PTV data can be used qualitatively to investigate the interaction between the Helmholtz resonator and the TS wave with the remark that the velocity data at the throat exit is not sufficiently converged.

4.4.3 Boundary layer thickness comparison

In this study, different techniques are used to determine the stability of a TS wave passing a Helmholtz resonator. While comparing the outcomes of these techniques, it is important to validate whether the used boundary layer conditions are the same.

In order to check if the boundary layers used for the PSE calculations match with the ones used in the linearised Navier-Stokes simulations and the experiments, the development of the momentum and displacement thicknesses are evaluated. The boundary used for the (adjusted) PSE calculations is computed with a boundary layer solver as described in section 3.1. The boundary layer to run the linearised Navier-Stokes simulation on is computed from the steady state laminar flow solver in COMSOL Multiphysics as described in section 3.2.

In the figures below (4.16 and 4.17), the boundary layer development is given for the three methods. The experimental boundary layer is evaluated using the global field of view results for throat configuration C_{base} without manually introduced TS wave. The processing of these global field of view images is done using PTV for this specific case in order to increase the amount of reliable u-velocity vectors close to the wall. This is needed to determine the wall location more accurately. For the experimental results, the assumption is made that the boundary layer computed for this specific case is representative for all measurement cases.

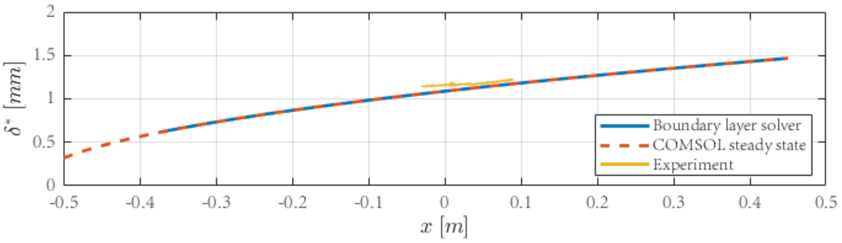

Figure 4.16: Displacement thickness development in streamwise direction

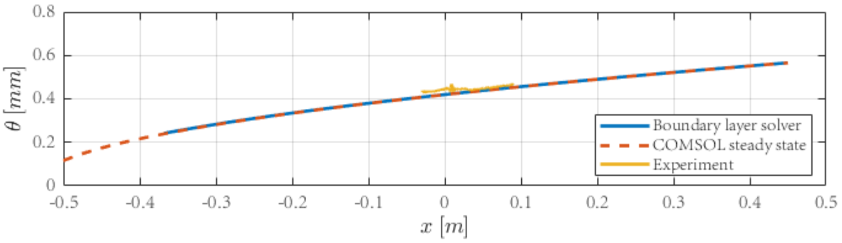

Figure 4.17: Momentum thickness development in streamwise direction

In the figures presented above, it can be seen that the boundary layer thicknesses used for the (adjusted) PSE calculation and the one used to run the linearised Navier-Stokes simulation on match appropriately over the complete domain. The boundary layer from the experiment can only be evaluated within the global field of view around the resonator (figure 3.12). The experimental boundary layer has a displacement thickness and a momentum thickness which are slightly larger than the ones used in the other methods. Although the difference is small, this could affect the TS wave and the way the TS wave interacts with the Helmholtz resonator.

Possible explanations for the difference between the numerical approaches and the experiment are two-fold. At the one hand, it is possible that the experimental boundary layer is actually thicker than the ones that are computed numerically. This can be caused by the flow conditions corresponding to the experimental setup, the stagnation point at the leading edge and a small pressure gradient because of the presence of the wind tunnel walls.
On the other hand, it is possible that the difference in boundary layer thickness comes from the algorithm behind the wall finding in the post-processing of the PIV/PTV data. This influences δ^* and θ accordingly. The wall-finding algorithm is

based on extrapolation of the boundary layer u-velocity values to the intersection with $u = 0$. The placement of the wall is therefore dependent on the amount of vectors in the lower part of the boundary layer and their accuracy. A slight displacement of the location of the wall can cause a (sub-millimetre) change in the computed boundary layer thickness. To minimise this effect, PTV with a fine binning grid was used for the boundary layer computation in this section, but a small offset can remain.

The boundary layers computed with the boundary layer solver and the laminar flow solver in COMSOL match appropriately with the experimental boundary layer. This justifies a comparison between the (adjusted) PSE, linearised Navier-Stokes simulation and experimental outcomes. Especially, if the v-velocity component is evaluated at $2\delta^*$ computed for the specific boundary layer, the error of the wall-finding algorithm can be (partly) avoided.

4.4.4 Boundary layer two-dimensionality

The (adjusted) PSE solver and linearised Navier-Stokes simulation are both two-dimensional. In order to compare the outcomes of these numerical studies to the experiment, two-dimensionality needs to be proven for this method. The experimental setup, as described in section 3.3, is two-dimensional. The flat plate is constant in spanwise direction and the resonator is also spanned in this direction. The throat is a slotted orifice that covers the centre part of the flat plate model. In order to justify the use of two-dimensionality, the flow also needs to behave 2D without spanwise velocity components. This can be evaluated using the pressure taps installed in the experimental model.

As described in methodology section 3.3.3, the pressure taps have different spanwise locations. It is possible to make a section of 'left taps' and 'right taps' looked at from the top of the flat plate. Although the streamwise locations of the taps on both sides is not equal, it is still possible to make a comparison between the sides by looking at the complete distribution. The development of the pressure coefficient C_p is given in figure 4.18. To obtain the pressure coefficient, equation 4.8 can be used.

$$C_p = \frac{p}{\frac{1}{2}\rho U_\infty^2} \tag{4.8}$$

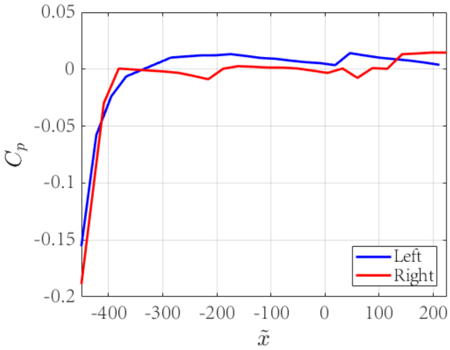

Figure 4.18: Streamwise development of the pressure coefficient for the left and right group of pressure taps

The two lines in figure 4.18 represent the pressure on the left and right of the flat plate model. In general, the pressure on the left of the flat plate is slightly higher than on the right. This can induce a (small) velocity component in spanwise direction which makes the flow three dimensional. However, this difference in pressure coefficient is so small ($C_p = \mathcal{O}(10^{-2})$) that the assumption of two dimensionality of the flow can be verified by these pressure tap measurements. With this observation, the conclusion can be drawn that the assumption of two-dimensionality in the experiment is justified.

4.4.5 Consistency of incoming TS wave strength

As mentioned in the sections about the convergence of the microphone and PIV/PTV data, there could be an influence of some inconsistency of the TS wave strength entering the area of interest. An instability is introduced in the boundary layer close to the leading edge by a DBD plasma actuator as described in section 3.3.1. This method of introducing TS waves is state of the art and the study by Benard & Moreau [54] suggests that using a burst modulation technique, a steady TS wave could be introduced in the boundary layer. However, from the microphone data and the TS wave amplitude evaluation from PIV and PTV data, the TS wave does not seem to have an equal amplitude when it enters the AOI, if different test cases are compared.

In the burst modulation method suggested by Benard & Moreau [54], a high frequency carrier signal is used. This carrier signal is multiplied by a square wave to modulate the output signal in order to reach the desired modulation frequency and duty cycle. However, in their paper, the carrier and modulation frequencies were chosen such that the carrier frequency is an integer multiplication of the modulation frequency. In this way, the signal cut made by the modulating square wave makes sure that the signal always starts from the natural starting point of a sine wave. For other frequencies, or with an additional induced phase delay, the signal could start at an arbitrary point on the sine wave. To make this statement more clear, figure 4.19 is added.

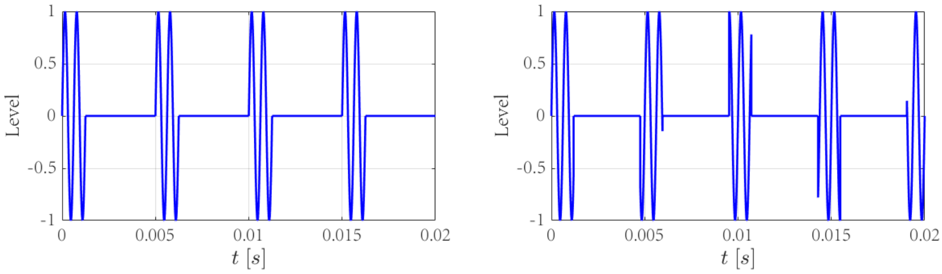

(a) $f_{\text{car}} = 1600$ Hz & $f_{\text{mod}} = 200$ Hz (b) $f_{\text{car}} = 1600$ Hz & $f_{\text{mod}} = 210$ Hz

Figure 4.19: Multiplication between an carrier sine wave and a modulating square wave

The shape and the starting point of a unit burst influence the body force that is exerted on the flow. This effect is larger for shorter unit bursts and these are used in the experimental campaign. In different parts of the high voltage sine wave, different physical phenomena take place. First, the air above the actuator is anodised and later, the ionised air is pushed away to create the body force, while still producing more ionised air. If this process is not started consistently from the sine neutral point, the induced body force that creates the TS wave becomes inconsistent.

The consequence of an inconsistent TS instability entering the AOI is that the absolute information on the development of the TS wave is lost. The only quantitative information that remains is the information of the development relative to an upstream parameter. This is especially unwanted if different phases within the phase locked measurements are compared with each other. The reason behind this, is that normalisation with an upstream value is difficult for these signals.

In order to solve this problem of a dissimilar unit burst, a somewhat different modulation technique is used. This does not include the multiplication of a carrier signal with a square wave, but a fixed unit burst that it started at a specific modulation frequency with a specified length. This can give the correct output signal to the actuator as suggested by Benard & Moreau [54] for all desired frequencies.

Although this adjustment increases the consistency of the incoming TS wave strength, there are still some discrepancies between measurement cases. The plasma actuator input can be assumed consistent, but there are some other plasma actuator or flow related phenomena that influence the TS wave consistency between different measurements cases.
One possible explanation considers some PIV seeding deposition on the plasma actuator. While conducting the experiments, smoke particles are added to the flow to be able to acquire images needed for PIV or PTV. These smoke particles are oily and can stick to the plasma actuator to affect its performance. Although the actuator was regularly cleaned with alcohol and the power loss in terms of current rise was marginally, this could still influence the TS wave strength. Also, the (sharp) cutting edge of the copper tape used to build up the actuator can be of influence.

Another possible explanation for the remaining TS wave inconsistency does not consider the plasma actuator only, but the wind tunnel test setup as a whole. On the lower side of the flat plate model, the air is directed away from the cavity and microphones by a flow guide as presented in the schematic in figure 3.1. This could imply that there is a (possibly unstable) pressure difference between the top and bottom side at the trailing edge of the model. Circulation is scattered from the trailing edge and this circulation must be conserved at the leading edge. This can lead to an unstable stagnation point at the leading edge, which could be located at the the measuring/suction side of the model. Probably, the frequency of this instability matches the TS wave frequency introduced by the plasma actuator. This unstable stagnation point changes the inflow conditions, which influences the behaviour of the TS wave accordingly.

The instabilities coming from the leading edge can be reduced by tripping the boundary layer to force laminar-to-turbulent transition downstream of the area of interest. This will decrease the circulation shredded by the leading edge and it will therefore stabilise the inflow conditions. This has been tested and the microphone data show improved consistency of the TS wave strength when a tripping device is added. It is recommended to use this tripping device for any following PIV/PTV measurements on this setup.

All in all, the consistency of the TS wave strength entering the area of interest is insufficient to obtain absolute information on the TS wave development and the influence of the resonator on it. This is especially detrimental for comparing phase locked cases. The possible explanations that are given in this section do not fully cover the full physics behind the TS wave inconsistency. Possibly, the used setup with the highly disturbing back side of the flat plate is not suitable to obtain a stable and consistent TS wave. Further research is needed to get full to understanding of this phenomenon.

In this section, the reliability of the experimental measurements is evaluated. The boundary layers used in the numerical and experimental methods match appropriately and the assumption of two-dimensionality in the experiment is validated. In general, conclusion can be drawn that the use of the microphone and PIV/PTV data in this study can be justified. However, it must be noted that some data points, especially near the wall, are insufficiently converged. Besides this, absolute comparisons between cases and techniques need a normalisation with an upstream parameter to account for the inconsistency in the TS wave strength.

4.5 GLOBAL INFLUENCE RESONATOR ON TS WAVE STABILITY

Earlier, in section 4.3, a hypothesis was set regarding the influence of the Helmholtz resonator on the stability of the TS wave. The main outcome of the adjusted PSE calculation coupled with the thermoviscous acoustics simulation is that only amplification of the TS wave is expected in the studied frequency range. This statement is strengthened by the outcome of the active throat linearised Navier-Stokes simulation. In this section, the experimental results show whether this hypothesis can be proven experimentally. This involves the global field of view random phase and phase locked PIV data and the acquired microphone measurements. Besides this, the outcomes of the different methods (adjusted PSE solver, linearised Navier-Stokes simulation and experiment) are compared to investigate the similarities between the numerical and experimental results.

4.5.1 Global field of view PIV: phase random

In order to investigate the global influence of the Helmholtz resonator to the TS wave, first, the PIV data on the global field of view will be presented. The outcome of the random phase measurements is a set of 2000 image pairs which are processed using PIV to obtain instantaneous velocity fields. From these fields, a time averaged standard deviation can be determined. This can be used to evaluate the spatial development of the TS wave. Especially the v-velocity standard deviation at $2\delta^*$ from the wall is used for this, as gives an appropriate representation of the TS wave strength.

Because of the inconsistency of the TS wave entering the AOI, a normalisation with an upstream value is needed. This was elaborately discussed in section 4.4.5. In this case, the standard deviation of the v-velocity at all streamwise locations in the field of view is divided by the mean value of this standard deviation between $\tilde{x} = -18.4$ and $\tilde{x} = 23.0$ to obtain $\tilde{\sigma}_v$. The relative v-velocity standard deviations for TS wave frequencies $f_{\text{TS}} = [240, 270, 290, 310, 340]$ Hz for the three resonator configurations C_{base}, C_1 and C_2 are given in the figures below. It must be noted that the v-velocity standard deviation field is smoothened with a kernel of 9 vectors in x- and y-direction to reduce the noise in the signal.

Figure 4.20 shows amplification of σ_v downstream of the resonator with respect to the baseline configuration for all tested frequencies and resonator configurations. Therefore, the hypothesis that the resonator will only amplify the TS wave is experimentally verified for the tested values of f_{TS}.

The pattern followed by the lines in figure 4.20 near the resonator location is specific and repeated for the different frequencies. Upstream of the resonator, the amplitude drops slightly and at the position of the throat, a peak is visible. Downstream of this peak, the amplitude drops sharply before it jumps back up to a value from which it follows the slope of the baseline configuration again. This specific local behaviour is present for all tested TS wave frequencies and it is highest for the values of f_{TS} closest to the the resonant frequency of the Helmholtz resonator. From these observations, the conclusion can be drawn that the resonator only has a locally am-

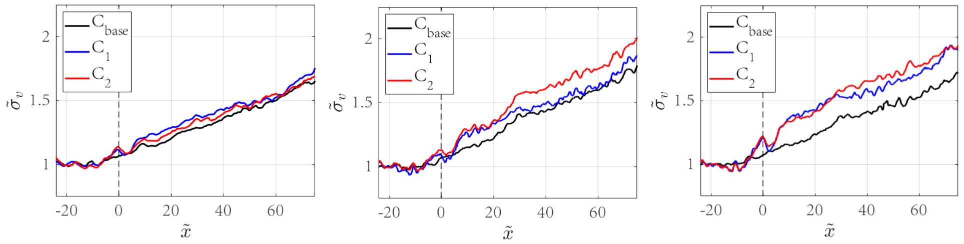

(a) $f_{\text{TS}} = 240$ Hz **(b)** $f_{\text{TS}} = 270$ Hz **(c)** $f_{\text{TS}} = 290$ Hz

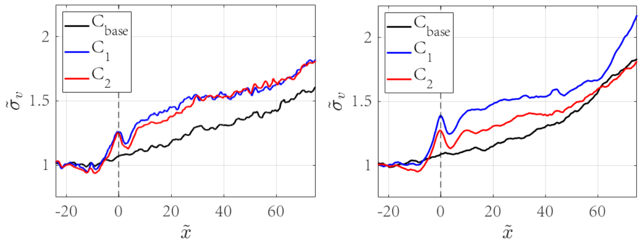

(d) $f_{\text{TS}} = 310$ Hz **(e)** $f_{\text{TS}} = 340$ Hz

Figure 4.20: Development of the standard deviation of the v-velocity at $\tilde{y} = 2$

plifying effect on the TS wave v-velocity. The v-velocity development at $y = 2\delta^*$ is considered a reliable indicator for the TS wave strength.

In order to test whether the linearised Navier-Stokes simulation and the adjusted PSE outcomes match the experimental PIV results, the experimental setup is modelled in the 2D COMSOL environment. This is described in section 3.2 in the methodology. In order to compare via the N-factor, an initial disturbance amplitude is needed for the simulation and experimental results (equation 1.8). The initial disturbance that is taken, is the TS wave v-velocity amplitude at $\tilde{x} = -20$ and $y = 2\delta^*$. This location is just within the field of view of the PIV results. This setup models the behaviour of a TS wave that starts growing closely upstream of the resonator location. The N-factor at this location is therefore zero for all three compared methods in figure 4.22.

For the linearised Navier-Stokes simulation, the amplitude of the fluctuating v-velocity is determined at $y = \delta^*$ from the wall similar to the evaluation points in the velocity fields from PIV. This height is represented by the dashed black line in figure 4.21. The colours in this figure correspond to the v-velocity in the 2D field at an arbitrary time step after convergence was reached. The amplitude of the v-velocity of the TS wave per x-location is calculated by performing a standard deviation over time between $(0.2\ s \leq t \leq 0.5\ s)$. In this way, a line representing the TS wave development in streamwise direction is created.

The adjusted PSE solver coupled with the thermoviscous acoustics simulation to model the Helmholtz resonator also outputs the N-factor. At every x-location, the PSE solver normalises the different parts of the eigenvector with the maximum u-velocity at that location. This has as a consequence that the N-factor is based on the maximum u-velocity at every streamwise location in the domain. The evaluation of the u-velocity in the PIV measurements is challenging because of the minor distance between the point of maximum u-velocity and the wall. This is why the choice has been made to use the v-velocity in the PIV and linearised Navier-Stokes simulation results to calculate the N-factor with. The assumption is made that the maximum v-velocity scales with the maximum u-velocity per x-location such that the N-factor can also be calculated with this parameter. The y-location of maximum v-velocity (green line) is close to $2\delta^*$ (black line) as visible in figure 4.21, therefore evaluation

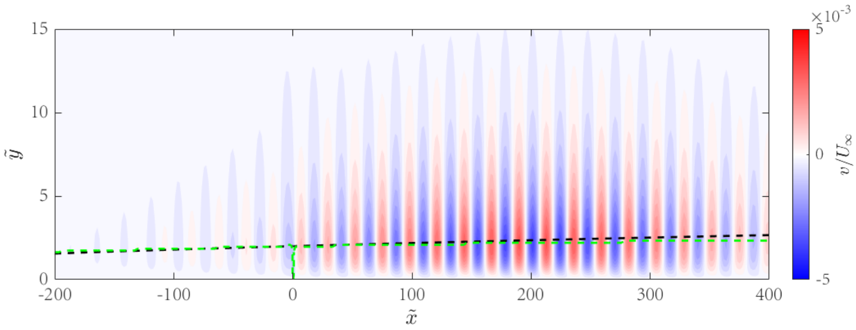

Figure 4.21: Contour plot of instantaneous v-velocity computed with the linearised Navier-Stokes simulation, for $f_{TS} = 290$ Hz and configuration C_{base}

on this point can be justified. With the N-factor, a comparison can be made between the outcomes of the linearised Navier-Stokes simulation, the experimental PIV data and the adjusted PSE solver.

The adjusted PSE solver is, just as a regular PSE solver, limited by the spatial step size in streamwise direction. This step size cannot be too small, as discussed in section 3.1. This limits the possibilities of implementing a boundary condition that is only imposed at the location and width of the resonator throat. Therefore the effect of the 1 mm wide throat of configuration C_1 is spread over the total width of a step size, which is $\Delta\tilde{x} = 23$ in this case. The overall effect is smaller in amplitude, but it continues over a larger range. In order to create a direct comparison between the different techniques, a node is exactly placed at the resonator throat centre and the steady state velocity field from the COMSOL laminar flow simulation is used to run the modified PSE on.

A comparison between the used methods based on the influence of the resonator on the TS wave stability is given in figure 4.22. In this figure, the x-location of A_0 is placed at $\tilde{x} = -20$ and the outcomes for the baseline and first resonator configurations are given separately for a fixed f_{TS} of 290 Hz.

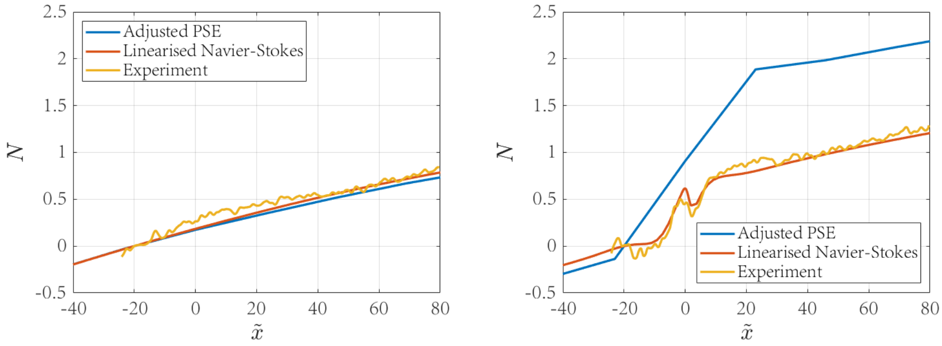

(a) C_{base} (b) C_1

Figure 4.22: N-factor development computed with the three different techniques, for $f_{TX} = 290$ Hz

Despite some noise, the lines representing both resonator configurations in figure 4.22 show good agreement between the linearised Navier-Stokes simulation and experimental data. The specific pattern in N-factor that already came forward in figure 4.20, is also predicted by the linearised Navier-Stokes simulation. Besides this, the magnitude of the resonator effect also matches well. The adjusted PSE signal, on the other hand, shows excellent agreement with the linearised Navier-Stokes simulation data for the baseline configuration. However, it performs inadequate for configuration C_1. The specific pattern around the resonator is not followed and the magnitude of amplification attributable to the resonator is overestimated. The inability to follow the specific pattern can be blamed on the large step size needed in the solver. But probably, an oversimplification of the real interaction can be expected, as the magnitude of the resonator effect cannot be matched with the other two methods. This will be discussed more elaborately in section 4.8. The adjusted PSE can therefore give qualitative information on whether amplification or attenuation is expected from the resonator, but quantitatively, it is inaccurate. The linearised Navier-Stokes simulation is able to adequately represent the experimental outcome. Therefore, this numerical method can also be used to predict the effect of a resonator on a passing TS wave quantitatively.

4.5.2 Global field of view PIV: phase locked

Next to the phase random PIV measurements, also phase locked tests are performed to investigate the influence of the Helmholtz resonator to the TS wave. In this process, the same phase of the TS wave is captured in every taken image. In this way, the shape of the TS wave can be obtained by taking the average over all the vector fields created after PIV processing. The specific behaviour of the resonator with respect to the TS wave can be evaluated for a full TS wave cycle by sweeping through the phases. To obtain the velocity fluctuations, a clean PIV case without any forced TS wave is subtracted from the phase locked results. For a full TS wave cycle, the phase locked results for the v-velocity are given in figure 4.23. The resonator configuration for this case is C_1 and the TS wave frequency is 290 Hz.

In figure 4.23, the propagation of the TS wave past the Helmholtz resonator can be seen as well as the interaction between the two. The propagation is highlighted with the black dashed line. The interaction between the TS wave and the resonator is mostly a fluctuating v-velocity coming from the resonator throat at $\tilde{x} = 0$. The v-velocity magnitude and direction are dependent on the phase of the TS wave above the resonator. The assumption is that the resonator is only driven by the pressure fluctuation of the TS wave. This pressure is not a result from PIV, but it can be predicted because of the fixed phase relation between pressure and velocity in a TS wave, as discussed in section 1.1.1.

For a specific TS wave phase, a comparison can be made between the experimentally and numerically determined development of the v-velocity fluctuation at $y = 2\delta^*$. This numerically determined development is a result of a linearised Navier-Stokes simulation. Because the initially forced TS wave for both methods is not necessarily the same, some normalisation is needed, as explained in section 4.4.5. This is similar to what was done for the random phase measurements in section 4.5.1. Because the experimental and numerical velocity signals are in-phase for the given time instance, the amplitude of the first peak in the field of view at $\tilde{x} = -25$ can be taken to normalise with. The signals both start from $\tilde{v} = 1$. For configurations C_{base} and C_1, the fluctuating v-velocity is given in figure 4.24 for one time interval.

The lines representing the v-velocity of the TS wave at $y = 2\delta^*$ are not smoothened or filtered. It can be seen that both lines are generally in good agreement with each other. Specifically, the behaviour near the resonator location in figure 4.24b is striking. A sudden sharp drop is noticeable at $\tilde{x} = 0$. This is different from the other parts of the signal and this effect is not noticed for the baseline case. Therefore, it can be concluded that this is an effect of the resonator to the TS wave. Further downstream, there are some discrepancies in the amplitudes, but this could also be influenced by the initial normalisation. These results of the phase locked measurements are in agreement with the results shown in figure 4.22. The conclusion

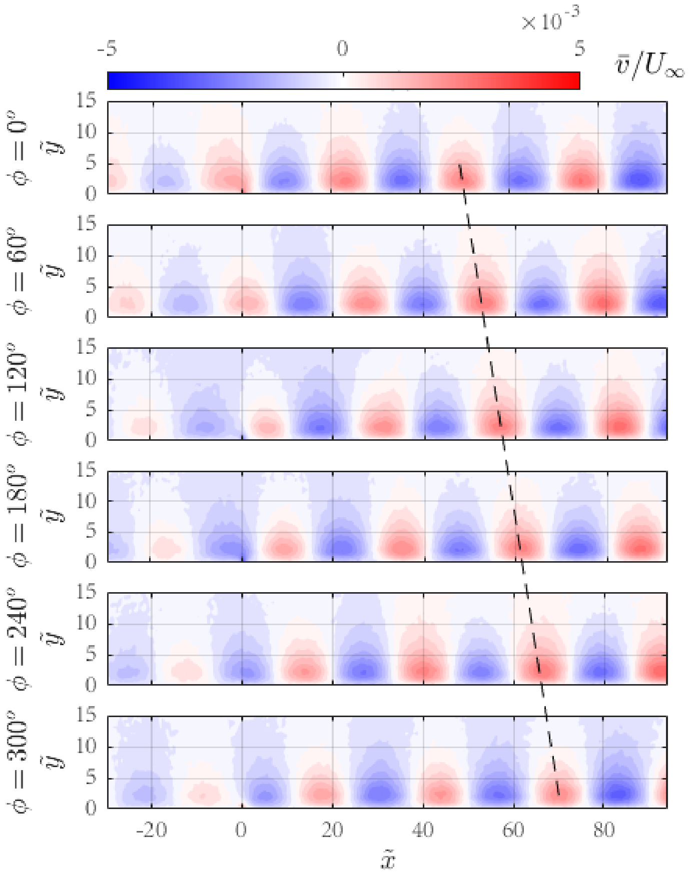

Figure 4.23: Phase locked velocity fluctuation fields for v for a full cycle of the TS wave, resonator configuration is C_1 and $f_{TS} = 290$ Hz

can be drawn that the linearised Navier-Stokes simulation and the global field of view PIV results match well. Since the same observations are made for the random phase evaluation in section 4.5.1, the conclusion can be drawn that the linearised Navier-Stokes simulation gives a reliable prediction for the experimental outcomes.

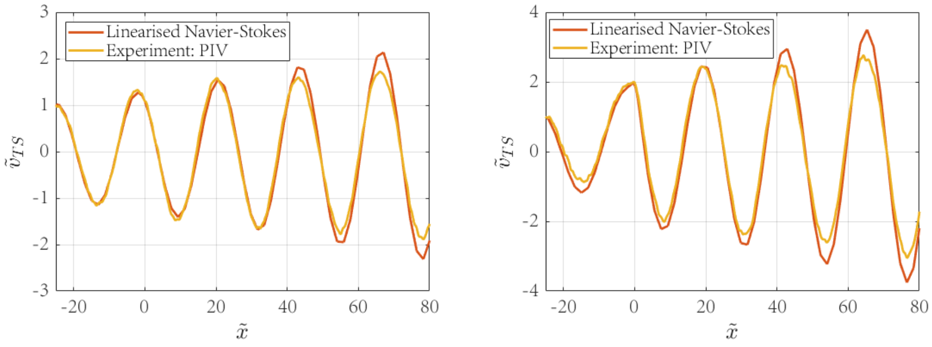

(a) C_{base}

(b) C_1

Figure 4.24: The fluctuating v-velocity determined with the phase locked PIV and a linearised Navier-Stokes simulation

4.5.3 Microphone measurements

Besides PIV, the other used measurement technique used in the experiment involves the installed microphones. With these microphones, the pressure fluctuation belonging to the TS wave can be measured. The magnitude of the pressure fluctuation is an indication for the the TS wave magnitude. So, with the microphones, the influence of the Helmholtz resonator to the TS wave can be investigated.

For a sweep of introduced TS wave frequencies between 200 and 400 Hz, the three microphones are recorded. Using the processing of the recordings with the Fourier transform as described in methodology section 3.3.2, the pressure fluctuations of the TS wave can be evaluated. Because the pressure of a TS wave is a result of the moving inertia of the wave, it can be used to quantify the strength of the passing wave and the influence of the resonator on this wave.

The absolute measured pressures are given in figure 4.25. In this figure, a comparison can be made between the different resonator configurations C_{base}, C_1 and C_2 for each microphone. It must be noted that there is no pressure value measured by the cavity microphone for the baseline configuration because the throat was fully covered to obtain a clean flat plate.

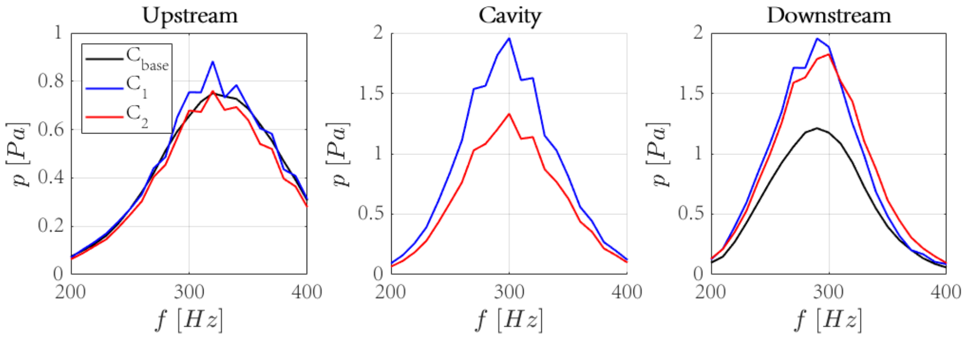

Figure 4.25: Absolute pressures measured by the upstream, downstream and cavity microphone for the three resonator configurations

The pressure signals obtained by the downstream microphone, corresponding to configurations C_1 and C_2 give a higher pressure amplitude than the baseline case for all frequencies. This implies that the resonator only amplifies the TS wave within the presented frequency range. This is in accordance with the hypothesis set in section 4.3 and the results from PIV on the global field of view (section 4.5.1 & 4.5.2). The peak in pressure amplitude for the downstream microphone measurements is located at a frequency around 290 Hz. The peak given for the cavity microphone has its centre at a similar frequency, but for the upstream microphone the peak is centred around 320 Hz. This peak at a higher frequency is caused by the stability of the TS wave, which implies that the frequency of the most amplified TS wave decreases for an increasing distance from the leading edge. This was shown in the stability diagrams in section 1.1.1. For the downstream microphone measurements, the peak location does not seem to be changed by the presence of the resonator, it is the same for all three configurations. This could be caused by the small difference between the frequency of most amplified TS wave according to stability and the resonant frequency of the used Helmholtz resonator.

The black curves in figure 4.25 that represent the baseline case are smooth, the blue and red lines are not and it is striking that the followed angular path is repeated for both resonator configurations. This path is present in the results from all microphones, including the upstream one. From the PIV results, it was clear that there is some upstream effect of the resonator. The v-velocity fluctuation amplitude just upstream of the resonator shows a dip. However, the upstream microphone is placed further upstream such that no effect on the v-velocity of the TS wave is expected. It seems that there is some additional acoustic emission from the resonator that propagates both up- and downstream. Radiation of acoustic sound from the resonator back into the flow was also mentioned in the paper by Panton & Miller [49]. This expected acoustic emission is more elaborately discussed later, in section 4.5.4.

For a fair comparison on the influence of the resonator to the TS wave stability, the strength of the incoming TS wave should be the same for all configurations at each frequency. As this is not the case according to the pressure amplitude given in the upstream microphone spectrum (figure 4.25), the cavity and downstream microphone measurement data can be normalised with the upstream microphone data. Normalisation with an upstream value was also used for the presentation of the PIV results in sections 4.5.1 and 4.5.2. This normalised pressure amplitude spectra are given in figure 4.26. The observed behaviour of the Helmholtz resonator is not expected to change for a different TS wave amplitude, because the problem is linear.

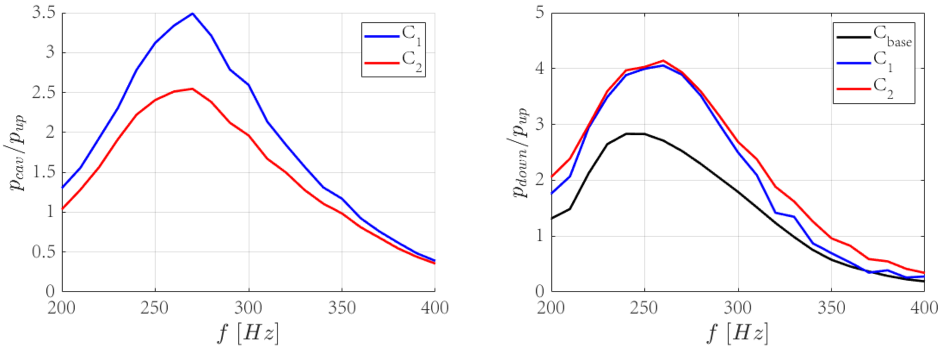

(a) Cavity microphone **(b)** Downstream microphone

Figure 4.26: Pressure amplitude for a range of frequencies relative to the upstream microphone data

Normalisation with the upstream microphone data does not change the conclusion that was drawn from the absolute pressure spectra (figure 4.25). The presence of a Helmholtz resonator leads to a higher pressure amplitude at the downstream position than the baseline case for every tested frequency according to figure 4.26. The position of the pressure amplitude peaks has shifted to a lower frequency with respect to the peaks in figure 4.25, because of the TS wave stability. Besides that, figure 4.26b shows that there is also an effect of the resonant frequency of the Helmholtz resonator. As known from section 4.1, the resonant frequency based on the pressure ratio between inside and outside the cavity peaks around 260 Hz. The red and blue lines in figure 4.26b peak around this 260 Hz where the black line peaks at a slightly lower frequency, around 240 Hz. This suggests that the Helmholtz resonator amplifies the TS wave and that it can shift the frequency of the most dominant TS wave based on its resonant frequency.

All in all, the conclusion from the microphone measurements can be drawn that the TS wave is amplified by the Helmholtz resonator for every tested frequency. The effect of the resonator is strongest near its resonant frequency. This is in accordance with the hypothesis set in section 4.3 and the results from the PIV data in section 4.5.1.

4.5.4 Acoustic emission

In the microphone measurement results for resonator configurations C_1 and C_2, some repeatable non-smooth behaviour is found which is not present in the baseline results (figure 4.25). To investigate this behaviour more thoroughly, the fluctuating pressure of the TS wave is evaluated using the linearised Navier-Stokes simulations. At the same y-location from the wall as the v-velocity was evaluated on ($y = 2\delta^*$), the standard deviation of the pressure is calculated for configurations C_{base} and C_1. The result is given in figure 4.27.

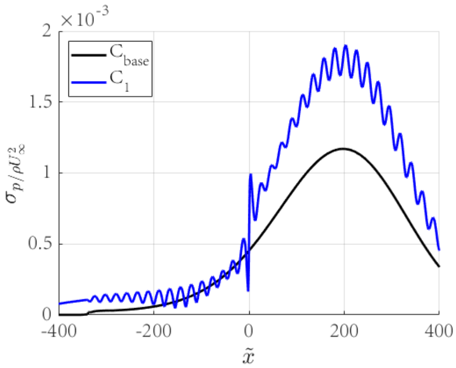

Figure 4.27: Standard deviation of the TS wave pressure at $y = 2\delta^*$, determined with the linearised Navier-Stokes simulation for configurations C_{base} and C_1 and $f_{\text{TS}} = 290$ Hz

The black line in figure 4.27 represents the baseline case. This line shows a smooth development of the TS wave pressure amplitude, similar to what is expected from the velocity components. The blue line, on the other hand, shows a similar trend as the baseline, but with an additional high frequency oscillation superimposed to it. It is expected that this extra oscillation is caused by the interaction between acoustic emission from the resonator and the TS wave. The wavelength of the extra fluctuation is also equal to the wavelength of the TS wave and therefore dependent on the frequency.

The global pressure field is visualised in a 2D plot. In this field, the acoustic emission is visible in the background, outside of the boundary layer. This is shown in figure 4.28 for time instance $t = 0.2598$ s. A dashed line is added at $\tilde{y} = 40$. The instantaneous pressure is evaluated at this line and presented in figure 4.29.

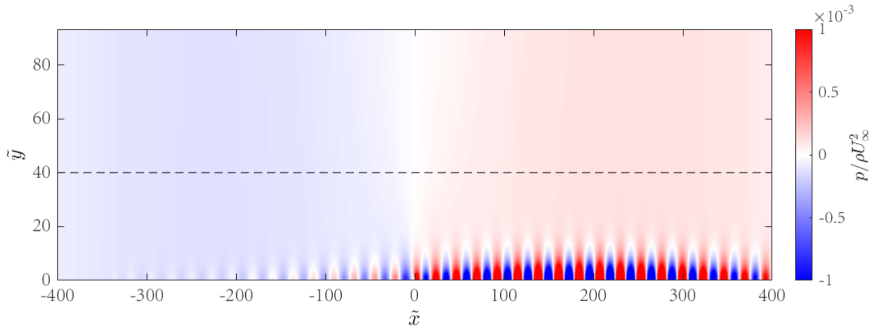

Figure 4.28: Contour plot of the pressure in the COMSOL field, determined from the linearised Navier-Stokes simulation for resonator configuration C_1, $f_{\text{TS}} = 290$ Hz and $t = 0.2598$ s

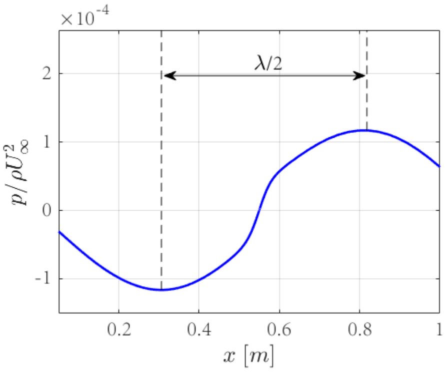

Figure 4.29: Instantaneous pressure at $\tilde{y} = 40$, determined from the linearised Navier-Stokes simulation for resonator configuration C_1, $f_{TS} = 290$ Hz and $t = 0.2598$ s

In figure 4.28, the background pressure field is clearly visible in the domain outside the boundary layer. For this specific time instance, the mean pressure location coincides with the resonator location at $\tilde{x} = 0$. In this way, the wavelength of the background pressure can be extracted as shown in figure 4.29. Half the wavelength has a length of 0.512 m. The wavelength of an acoustic wave with the same frequency as the TS wave frequency is $\lambda = c/f = 1.183$ m. The wavelength of the pressure wave in the background is close to the acoustic wavelength and with this, the acoustic emission from the resonator is demonstrated. The presence of the wind tunnel walls and their reflections can also play a role in this effect. The expectation is that the microphones are influenced by this acoustic pressure and that the angular pattern in figure 4.25 is not a measurement error. The radiation of acoustic sound from the resonator to the flow is in accordance with the findings described in the paper by Panton & Miller [49].

The acoustic emission by the Helmholtz resonator disturbs the pressure measurements in the experiment and numerical simulation. Therefore, it can be argued that velocity measurements represent the TS wave strength more reliably than pressure measurements. The velocity measurements do not seem to be affected by the acoustic emission. This observation can be included in any further research to this subject.

4.6 LOCAL INFLUENCE RESONATOR ON TS WAVE STABILITY

The conclusion drawn in section 4.5 is that the TS wave is only amplified by the Helmholtz resonator. This is demonstrated using the global field of view PIV data, supplemented with the microphone data and results from the linearised Navier stokes simulations. In this section, the influence of the resonator to the TS wave is investigated in more detail using of the local field of view PTV results as described in section 3.3.5. For the local field of view PTV, only phase locked experiments are conducted to observe the interaction over time during the full TS wave cycle as it passes through the field of view.

Similarly to figure 4.23, the interaction between the resonator and the TS wave per phase can be evaluated in a contour plot of the v-velocity. Again, these figures are made after subtraction of a velocity field obtained without a forced TS wave. In these velocity fields obtained with PTV, the flow going in or coming out of the resonator throat can be quantified in more detail than in the global FOV PIV results.

Figure 4.30 shows the interaction over a full TS wave cycle between the resonator and the passing TS wave.

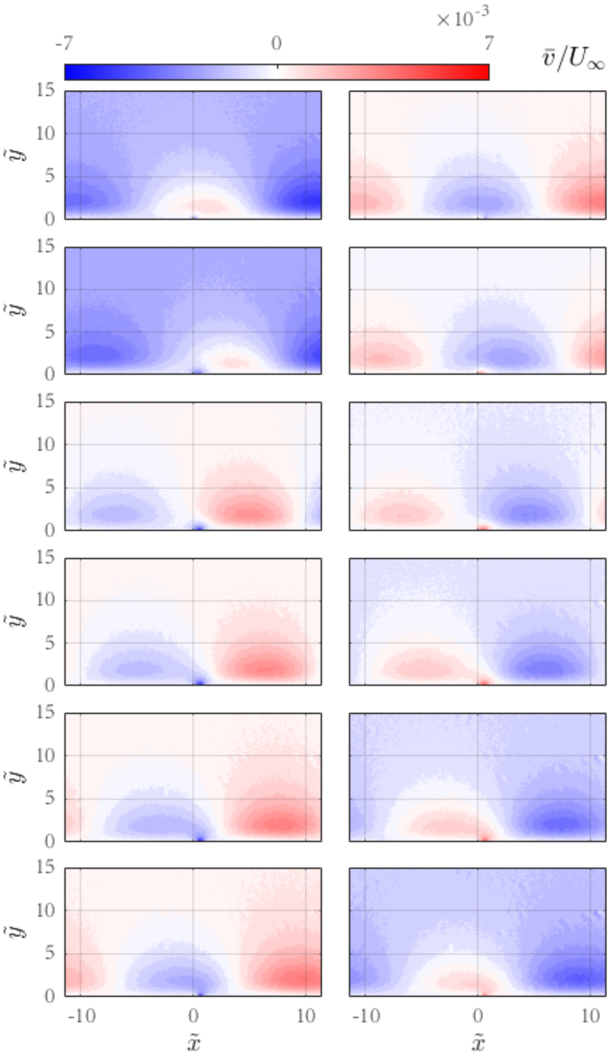

Figure 4.30: Phase locked v-velocity fluctuation fields for a full cycle of the TS wave, resonator configuration is C_1 and $f - \mathrm{TS} - 290$ Hz
Left from top to bottom $\phi = 0°$ to $\phi = 150°$ in steps of $30°$, on the right $\phi = 180°$ to $\phi = 330°$

In figure 4.30, it stands out that the background colours blue, while a white background corresponding to $\bar{v}/U_\infty \approx 0$ is expected. This is to a lesser extent the case for the global field of view PIV results in figure 4.23. In order to capture the TS wave amplitude accurately, the background v-velocity at the top of the FOV can be subtracted from the v-velocity values corresponding to the TS wave.

With the zoomed-in FOV, the v-velocity at the throat exit can directly be evaluated for the TS wave phase angles presented in figure 4.30. The TS wave phase angle $\phi = 0°$ was chosen such that there is a positive peak in v-velocity at $\tilde{x} = 0$. From the obtained data, the TS wave phase angle can be evaluated more accurately by picking the TS wave v-velocity at $y = 2\delta^*$. The phase difference between the TS wave v-velocity and the throat exit v-velocity during a full TS wave cycle can be approximated from these PTV results. The experimentally obtained velocity signals during the full TS wave cycle are given in figure 4.31.

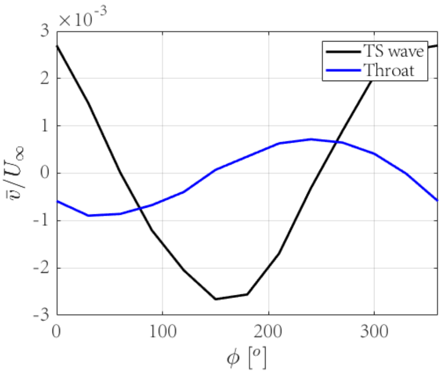

Figure 4.31: TS wave and throat v-velocity obtained from local FOV PTV data for a full TS wave cycle

In figure 4.31, the black line represents the TS wave v-velocity determined at $\tilde{x} = 0$ and $\tilde{y} = 2$. The blue line represents the wall-normal velocity at the resonator throat exit, which is evaluated at $\tilde{y} = 0.1$. It is clear that this sine wave representing the throat exit velocity has a different phase than the TS wave v-velocity signal. The phase difference between the pressure and the v-velocity of a TS wave is 90° and constant, as discussed in section 1.1.1. The pressure signal should therefore follow the same trend as the TS wave v-velocity in figure 4.31 but shifted 90° to the right. The phase difference between the pressure of the TS wave and the v-velocity at the throat exit is an important factor in TS wave stabilisation as discussed in section 4.2. The velocity signals presented in figure 4.31 suggest a phase difference between the TS wave pressure and the resonator throat v-velocity of about 180°. This causes the highest TS wave amplification according to the hypothesis set in section 4.3 which is verified in section 4.5.

The local interaction between the Helmholtz resonator and the passing TS wave is investigated in this section. Here, the main focus is on the phase relation between TS wave pressure and v-velocity in the resonator throat, which is needed for TS wave stabilisation according to section 4.2. The predicted phase difference between TS wave pressure and throat exit velocity from the thermoviscous acoustics simulation presented in figure 4.4 was investigated experimentally from the local field of view PTV data. The conclusion can be drawn that the phase difference from the thermoviscous acoustics gives an adequate prediction of the experimental situation.

4.7 DIFFERENT THROAT CONFIGURATION

In the previous sections, the interaction between a Helmholtz resonator and a TS wave is described. The eventual conclusion is that this resonator could only amplify the TS wave in the chosen frequency range. This was already predicted by a model that couples a modified PSE solver to a thermoviscous acoustics simulation to model the presence of the resonator in section 4.3. The results presented in section 4.2 imply that there is a certain phase difference threshold around $\Delta\phi \approx \pm 90°$ where an amplifying boundary condition changes into an attenuating one. A different setup is used for the thermoviscous acoustics simulation in COMSOL, this setup is shown in figure 4.32a. This new configuration has two throats connected to a single cavity. The threshold of $\Delta\phi \approx \pm 90°$ is crossed to reach an attenuating phase relation for certain frequencies as shown in figure4.33b. The outcome of this thermoviscous acoustics simulation suggests that attenuation is reached with this setups. This is further investigated using experimental data in this section.

The new throat configuration (C_3) has two throats that both see (approximately) the same pressure amplitude, but exactly out of phase. In the thermoviscous acoustics setup, this looks as presented in figure 4.32a. For the experimental setup, this implies that the throats are placed exactly half a wavelength of the TS wave apart. A new throat part is used in the experimental setup. This part has two throats with a width of 1 mm and a depth of 5 mm as presented in figure 4.32b. The spacing between the throats is 12 mm.

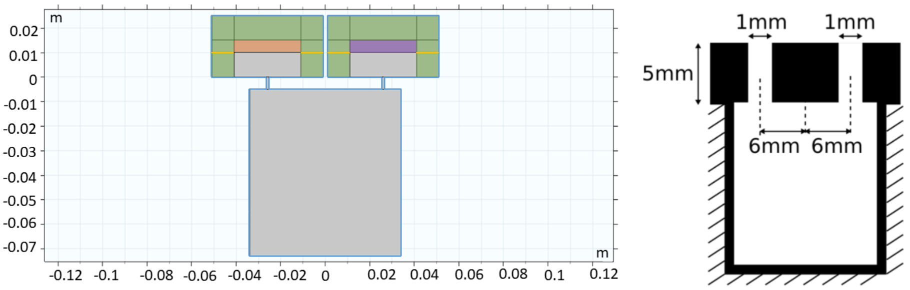

(a) Thermoviscous acoustics setup for the resonator with two throats

(b) Throat part C_3 geometry

Figure 4.32

Using the PSE solver as described in section 1.1.1, the wavelengths can be evaluated at $\tilde{x} = 0$ for different TS wave frequencies. The frequency where the half wavelength matches the spacing between the two throats (12 mm) is $f_{TS} = 295$ Hz according to figure 4.33a. So, in order to reach an experimental situation in which both throats see the TS wave completely out of phase, the frequency can only be 295Hz.

In figure 4.33b, the amplitude/phase relation between velocity and pressure is given as a result of a thermoviscous acoustics simulation. The frequency that is used in the experiment is highlighted with the vertical dashed line in this figure. The phase difference between pressure and velocity at the top of both throats is less than 90 degrees, therefore TS wave attenuation is expected. If the pressure amplitudes exerted on both throats are exactly equal and the waves have a phase difference of $180°$, the response at the top of both throats is exactly the same. This is shown in figure 4.33b. The validity of the assumption that both throats see the same pressure amplitude can be doubted. The pressure above the downstream throat can be influenced by stability of the TS wave and the effect of the upstream throat. This effect is not taken into account in the thermoviscous acoustics simulation.

The only frequency interesting to investigate experimentally for this throat configuration is 295 Hz. For every other frequency, the TS wave above the two throats is not exactly out of phase. Therefore, if the frequency is not equal to 295 Hz, the amplitude/phase relation in figure 4.33 is not longer valid. The results in terms of v-velocity standard deviation coming from the random phase global FOV PIV experiment is given in figure 4.34. In this figure, a comparison is made between the TS wave development for the baseline configuration $_{\text{base}}$ and the new double throat configuration C_3, similar to figure 4.20.

The line corresponding to the new resonator configuration C_3 in figure 4.34 shows that the amplitude of the v-velocity fluctuations of the TS wave are amplified by the presence of the resonator. This amplification is similar to what was presented for the regular Helmholtz resonator with a single throat in figures 4.20 and 4.22. The specific local behaviour around the resonator location that was also visible in figure 4.20 returns in figure 4.34 but twice in series. The double resonator configuration C_3 acts like there are two regular Helmholtz resonators closely behind each other

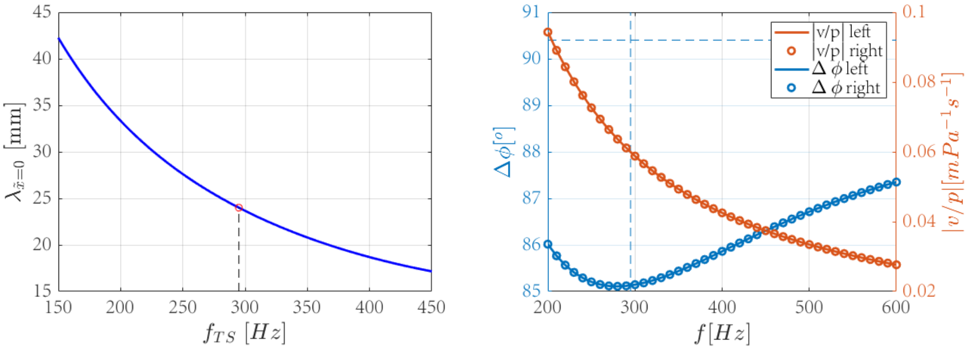

(a) Relation between TS wave frequency and wavelength at $\tilde{x} = 0$ calculated with PSE

(b) Amplitude/phase response determined with the thermoviscous acoustics calculation at the top of the two throats

Figure 4.33

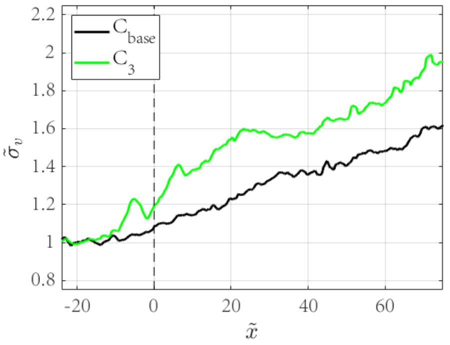

Figure 4.34: Global FOV PIV standard deviation of the v-velocity evaluated at $y = 2\delta^*$ for resonator configuration C_{base} and C_3 for $f_{\text{TS}} = 295$ Hz

in streamwise direction. However, the magnitude of amplification corresponding to a regular Helmholtz resonator is larger than what a single throat in configuration C_3 shows in figure 4.34. The magnitude of the total effect of the new double throat configuration to the TS wave is similar to the effect of resonator configuration C_1 in figure 4.20c. However, it must be noted that the TS wave frequency is not exactly the same (290-295 Hz). Moreover, a comparison between these cases does not take the inconsistency of the TS wave (section 4.4.5) into account. TS wave amplification due to the double throat configuration C_3 is in contradiction with the hypothesis based on the the amplitude/phase response computed with the thermoviscous acoustics simulation.

With the similarities between the outcomes from the different used methods (PSE, linearised Navier-Stokes simulation and experiment) presented in figure 4.22 the suggestion was made that the adjusted PSE solver was able to adequately predict the experimental outcome qualitatively. This was all based on the adjusted PSE solver coupled with the thermoviscous acoustics simulation to model the resonator. The hypothesis of TS wave attenuation based on the phase relation computed by the thermoviscous acoustics simulation for configuration C_3 is not supported by the experimental data. The outcome of the experimental PIV data shows TS wave amplification for the double throat configuration. The conclusion can be drawn that either the thermoviscous acoustics setup with two throats connected to a single cavity is inaccurate or that there is another important effect in the interaction between the TS wave and the resonator that is not accounted for in the adjusted PSE solver.

4.8 PHYSICAL FRAMEWORK

With the predictions made using the adjusted PSE solver (sections 4.2 & 4.3), the outcomes of the linearised Navier-Stokes simulation and the experimental outcomes discussed (sections 4.5 & 4.6), the physical framework behind the adjusted PSE solver can be evaluated. In general, this solver with low computational costs is able to qualitatively predict whether the Helmholtz resonator causes amplification or attenuation of the TS wave based on a v-velocity boundary condition. The magnitude and phase of the used local boundary condition are based on the TS wave pressure at that same point in the domain. The major assumptions behind this model are that the TS wave pressure fluctuation is the only driver of the resonator and that the resonator responds acoustically.

With these assumptions, the amplitude/phase response of the resonator between the pressure and velocity at the top of the throat is determined using the thermoviscous acoustics module in COMSOL Multiphysics (figure3.4b). This module is based on the propagation of acoustic waves including losses due to propagation through narrow orifices like the resonator throat. The outcome is therefore purely acoustic with the acoustic pressure fluctuations causing acoustic velocity fluctuations in the resonator throat. There is no fluid mass flow taken into account in this module.
The TS wave exerts a pressure on the wall and because the ratio between the throat width and the wavelength of the TS wave is small, the pressure can be seen as an equally distributed forcing over the throat width.

Pressure is not the only parameter propagating with the TS wave. There are also velocity fluctuations that might also influence the velocity inside the resonator throat. This cannot be captured in the thermoviscous acoustics simulation since there is no induced velocity connected to the fluctuating pressure input. The influence of the TS wave velocity to the throat velocity, however, seems to be marginal. The qualitative influence of the resonator to the TS wave amplitude is captured appropriately by the adjusted PSE calculation if this is compared with the experimental data (figure 4.22). Moreover, the predicted phase relation between p and v by the thermoviscous acoustics simulation is validated by the local field of view PTV data (section 4.6). This implies that some kind of TS wave impedance, as discussed in section 4.2, influences the TS wave stability similarly to what was seen in acoustics [10] and for hypersonic boundary layer stability control [46].

According to the research by Panton & Miller [49], the resonant frequency can change when the resonator is in turbulent grazing flow. In this study, the boundary layer is laminar, but the viscous effects inside this boundary layer could also influence the resonant behaviour of the resonator. The end correction for equation 2.3, belonging to the fluctuating mass of air inside the throat could be influenced by the presence of the boundary layer. In quiescent conditions, the air that fluctuates in the resonator throat can be seen as a moving control volume without in- and outflow. For a resonator in boundary layer flow, the air that comes out of the throat is dragged away by the flow. This can be related to the findings of Flynn et al. [12]. They state that high momentum flow is sucked in by the Helmholtz resonator and low momentum flow is expelled. This can cause an extra circulative effect above the resonator which could lead to the specific pattern that is visible in the TS wave amplitude in for example figure 4.20. This effect cannot be captured with the adjusted PSE solver.

The magnitude of amplification due to the resonator, predicted by the adjusted PSE solver is generally overestimated in comparison with the experimental and linearised Navier-Stokes results. The spatial step of the PSE solver is limited and needs to be relatively large, as described in section 3.1. The throat, on the other hand, needs to be narrow, to satisfy the assumption of equal distribution of pressure over its width. In the adjusted PSE solver, the effect of the resonator is spread over the full spatial step. This implies that locally, the magnitude of the resonator effect is reduced, but it continues over a longer streamwise range. The spread of the v-velocity boundary condition could influence the effect on the TS wave stability.

For the adjusted PSE results presented in figure 4.22, the multiplication factor F_{BC}, as described in section 3.1.1, is equal to 1. So the full resonator effect, as determined from the thermoviscous acoustics simulation is taken into account. For this value of F_{BC}, the magnitude of the effect does not match the simulation or experimental results. The effect of the resonator can be manually modified by changing this factor to match the outcome of the adjusted PSE solver with the outcome of the linearised Navier-Stokes simulation. If a factor of $F_{BC} = 0.3$ is chosen, the effect of the resonator is weakened. The step size ($\Delta\tilde{x}$) for this setup can be slightly decreased to $\Delta\tilde{x} = 18$. A comparison between the adjusted PSE results with the lower multiplication factor and the linearised Navier-Stokes simulation with its regular resonator effect is given in figure 4.35.

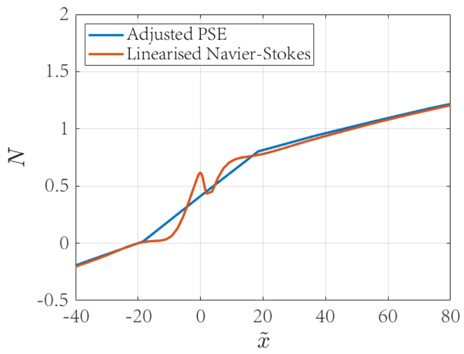

Figure 4.35: N-factor comparison between the adjusted PSE solver with attenuated resonator effect ($F_{BC} = 0.3$) and linearised Navier-Stokes equation for resonator configuration C_1 and $f_{TS} = 290$ Hz

In figure 4.35, the attenuated effect of the resonator to the N-factor is shown. As parameter A_0 for the N-factor, the TS wave amplitude at $\tilde{x} = -20$ is taken. With these settings, the amplitude computed with the adjusted PSE matches the linearised Navier-Stokes simulation result downstream of the resonator. The specific pattern of the N-factor around the resonator is skipped. This can be explained by the relatively large spatial step needed for solver stability, which covers the whole pattern above the resonator in this case. Besides this, it can be seen that there is an effect of the inhomogeneous boundary condition in the adjusted PSE solver in the points at and just downstream of the resonator. With the current solver, there cannot be any upstream effects, so the dip that is visible just upstream of the resonator in the linearised Navier-Stokes simulation result cannot be simulated with the adjusted PSE. It is expected that more effects of the interaction between the resonator and TS wave need to be included. Just the modelling of an inhomogeneous v-velocity boundary condition is insufficient to reach the same pattern as found in the simulations and experiments. Also, the effect of the acoustic emission, described in section 4.5.4, cannot be modelled by this solver. Nevertheless, it is doubtful that this influences the magnitude of the resonator effect and the specific pattern of amplification, since it is only visible in the pressure data 4.5.4).

All in all, the adjusted PSE solver that includes the results of a thermoviscous acoustics simulation can predict the effect of a Helmholtz resonator to the stability of a TS wave qualitatively. Therefore, it can be used as a tool to predict whether an acoustic metamaterial is able to potentially attenuate a TS wave. The solver only includes a v-velocity boundary condition based on the pressure at the specific location and is therefore very simplified. For a more detailed prediction of the influence of a resonator to the TS wave stability, a linearised Navier-Stokes simulation can be used, although this is computationally more expensive.

5 CONCLUSIONS & RECOMMENDATIONS

The research that is described in this thesis is conducted to answer the main question:

Are acoustic metamaterials suitable for attenuating Tollmien-Schlichting waves to delay boundary layer transition in subsonic conditions?

Prior to formulating an answer to this question, the sub-questions that are stated in the introduction need to be reviewed. The first sub-question relates to the property of the wall controller needed to achieve TS wave damping. It is possible to actively suppress TS waves with an active method using damping/suction through the surface [22] [27], wall heating/cooling [23] [28], a vibrating ribbon [24] or a plasma actuator [25] [26]. In the studies by Malik et al. [23], Liepmann et al. [28] and Thomas et al. [24], damping was achieved by superimposing a wave that is similar wave to the TS wave, but completely out of phase with. This implies that the phase relation between the TS wave and the wall controller is important for the controller performance. A similar conclusion can be drawn from studies to the damping of acoustic wave with metamaterials. The acoustic impedance of the metamaterial at a certain frequency indicates whether sound waves are damped or not. The acoustic impedance is the ratio of the complex acoustic pressure at and the complex acoustic velocity normal to the wall, which also includes the phase. Optimal damping is achieved if the impedance is either purely real or zero [46]. A purely real impedance physically means that there is no phase difference between the acoustic pressure and the obtained acoustic velocity. From calculations with the adjusted PSE solver and linearised Navier-Stokes simulations, it was demonstrated that optimal TS wave damping is achieved if the imposed wall v-velocity is in-phase with the TS wave pressure. In general, the conclusion can be drawn that damping is achieved when the phase difference between the TS wave pressure and the wall v-velocity boundary condition is less than approximately 90°.

With a clear image of the wall controller properties, the second sub-question regarding the most suitable acoustic metamaterial concept can be answered. Literature shows three main branches of acoustic metamaterials: negative effective mass/-density, negative bulk modulus and double negative [21]. With all branches of metamaterials, sound wave damping could be achieved. However, for feasibility reasons, the Helmholtz resonator concept was chosen for this study from the negative bulk modulus branch. The resonant behaviour of a meta-atom is important for the performance of the metamaterial system and the resonant behaviour of a Helmholtz resonator is only dependent on geometrical parameters. Multiple studies show acoustic wave damping with an array or lattice of Helmholtz resonators [6] [8] [9] [10] and the study by Fey & Robertson [11] shows sound damping with only a single Helmholtz resonator. Because of a lack of literature on the interaction between a Helmholtz resonator and instabilities in a laminar boundary layer, this study only evaluates the influence of a single Helmholtz resonator on the development of a TS wave. Using the adjusted PSE solver coupled with the thermoviscous acoustics simulation on this Helmholtz resonator, the phase difference between the TS wave pressure and the throat exit v-velocity can be obtained. This phase difference does not enter the damping band of $|\Delta\phi| < 90°$ for the evaluated frequencies. The hypothesis of this simplified model is therefore that a Helmholtz resonator can only increase the amplitude of a passing TS wave.

This hypothesis is further tested in a wind tunnel test campaign. During this campaign, the wind tunnel free stream velocity is fixed at around 20 m/s. To obtain a TS wave with a frequency close to the resonant frequency of the tested Helmholtz resonator configurations, a controllable plasma actuator is used. This plasma actuator exerts a fluctuating body force that leads to an instability inside the boundary layer. This instability grows into a TS wave and this propagates further downstream. Two dimensionality of the flow is proven via pressure taps that are included in the model. This justifies the use of a 2D Helmholtz resonator throughout the experiment. The TS wave behaviour is evaluated using three microphones, a global field of view PIV setup and a local field of view PTV setup. The microphones and the global field of view PIV setup are able to measure the development of the TS wave amplitude in streamwise direction. The local field of view PTV on the other hand, can give information about the interaction between the TS wave and the resonator locally near the throat exit. Linearised Navier-Stokes simulations give supplementary information to the findings in the experiments and are able to provide field pressure information which is not attainable from the PIV or PTV data.

The processed data from the microphone and PIV measurements clearly shows that, for the tested frequencies, the TS wave is only amplified by the resonator. This means that the hypothesis can be confirmed for the currently tested, resonator configurations and flow conditions. Both tested resonator configurations amplify the TS wave downstream in comparison with the baseline. A quantitative comparison between the different measurements is difficult because the TS wave entering the area of interest is not consistent in strength between test cases. A normalised study comparing the N-factors calculated from the outcomes from the adjusted PSE solver, the linearised Navier-Stokes simulations and the global field of view PIV measurements, shows similarities between all three techniques for the baseline configuration. For resonator configuration C_1, the experimental outcomes match well with the results of the linearised Navier-Stokes simulation. The same specific pattern of TS wave amplification is found in the results coming from both methods. The adjusted PSE solver, on the other hand, shows amplification, but the magnitude of the effect is overestimated. The specific pattern of amplification near the resonator throat is also not reproduced in the adjusted PSE results, this is probably caused by an oversized spatial step and an oversimplification of the interaction. Despite this, qualitatively, the effect of the resonator is well predicted by this solver.

The local field of view PTV results show that the phase difference between the v-velocity coming from the throat exit and the v-velocity of the TS wave above it are in accordance with the prediction made with the thermoviscous acoustics simulation. This implies that this phase difference is an important factor in the physical framework behind the interaction between the TS wave and the Helmholtz resonator. Next to this, there are some additional effects that play a role in this interaction. The resonant behaviour of the Helmholtz resonator can be influenced by the boundary layer, as also mentioned in the study by Panton & Miller [49]. Next to that, an emission of acoustic waves is expected from the resonator throat according to the microphone data and the pressure field in the linearised Navier-Stokes simulations. This acoustic effect was also mentioned in the paper of Lin et al. [13]. However, the increased turbulence level that is found in their study to the interaction between a turbulent boundary layer and a Helmholtz resonator is damped out downstream. This is in contradiction with the findings of this study, because the increase in TS wave amplitude remains downstream and does not damp out. Besides these extra effects, there are also discrepancies found between the prediction from the adjusted PSE and the experimental outcome. Especially for resonator configuration C_3, where two throats are connected to the same cavity. According to the thermoviscous acoustics simulation, the phase relation between the pressure and velocity at the top of the throats should cause TS wave attenuation, but the experimental results show only amplification. A setup with two throats and one cavity where both throats see a pressure fluctuation in opposite phase could strictly not be considered a Helmholtz resonator. This does therefore not influence the physical framework behind the interaction between a TS wave and a Helmholtz resonator, but it points out at a possible discrepancy in the adjusted PSE solver coupled to the thermoviscous acoustics simulation.

With the sub-questions of this research answered, the answer formulation to the main question can be considered. In this study, only a single Helmholtz resonator is used to investigate its influence on the development of a TS wave. This Helmholtz resonator is only a single meta-atom of a possible acoustic metamaterial system, so a complete answer to the main question cannot be given. However, the conclusion can be drawn that according to the findings in the experiment, the adjusted PSE solver and the linearised Navier-Stokes simulation, a single 2D Helmholtz resonator will not attenuate TS waves for frequencies close to resonance in subsonic flow conditions. On the other hand, the physical framework behind the interaction between a TS wave and a resonator shows that the phase relation between the TS wave pressure and the exerted v-velocity at the wall is important to achieve damping. This is similar to the importance of impedance matching in acoustic wave suppression for acoustic metamaterials. Thus, if a concept can be developed that gives the desired impedance-like phase relation between TS wave pressure and wall controller v-velocity, acoustic metamaterials can be suitable for TS wave damping to delay boundary layer transition.

Although this research points out at what effects play a role in the interaction between a TS wave and a Helmholtz resonator, it is unknown whether these effects describe the physics behind the interaction completely. To find this out, a more thorough investigation needs to be done to the local interactive behaviour. In the results from the global field of view, for example, a very specific pattern is followed in the TS wave amplitude development. This is also found in the outcomes of the linearised Navier-Stokes simulations, but the underlying effect is still unknown. Besides this local interaction, the global interaction to, for example, a streamwise array of Helmholtz resonators, can also be interesting for a study to the influence of an acoustic metamaterial on a TS wave. In an array, the individual units can interact with each other to possibly create a different effect on the TS wave with different outcomes. This array or lattice of resonators is also successfully used as a metamaterial to damp sound in acoustic studies [6] [8] [11] [9].

During the experimental campaign, the issue of the inconsistent TS wave entering the area of interest arose. This eventually lead to problems with quantitative comparisons between measurement cases and different techniques. The problem was described elaborately in section 4.4.5. Tripping the boundary layer from laminar to turbulent downstream of the last measurement location seems to improve the TS wave consistency according to the microphone measurements. This tripping was not used while conducting the PIV and PTV measurements, so it is recommended to use this method for further research to this setup. Furthermore, it is likely that the remaining inconsistency of the entering TS wave, as it was still not perfect according to microphone data, has to do with the used wind tunnel setup and model. Guiding the flow out from the bottom side was needed to shield the microphones and the resonator cavity, but it might also have caused instabilities at the leading or trailing edge which could influence the experiment. A revision on the model and the setup are needed to prevent this unwanted phenomenon of TS wave inconsistency.

In order to find out whether the pressure-velocity phase relation can be achieved with another acoustic metamaterial concept, it is recommended to test these. Because of the similarities between the experiment, the adjusted PSE solver coupled with the thermoviscous acoustics simulation and linearised Navier-Stokes simulations, a preliminary study to the feasibility of the right phase relation can be done numerically. A first investigation can be performed with the adjusted PSE solver to get a qualitative idea of the behaviour of the concept. If TS wave attenuation is predicted with this model, a more thorough investigation is recommended using a linearised Navier-Stokes simulation.
Possible concepts that have the potential to get TS wave attenuation are given here.

- The mass-membrane system as described in section 2.2.1 could cause negative mass/density in certain frequency bands. This could have a different influence on the TS wave than the Helmholtz resonator concept, which could cause a negative bulk modulus. Although it is difficult to physically produce such mass-membrane system up to the right specifications, it could be worth trying when a numerical study shows that it could work. A possible downside could be that it is difficult not to increase surface roughness with this concept.

- To work around this possibly added surface roughness, a concept which combines the Helmholtz resonator with the mass-membrane system could be tried. This concept was suggested by García-Chocano et al. [9] and executed by Hu et al. [40] [41]. A concept that gives a negative bulk modulus is coupled with a concept that gives a negative effective mass/density in some frequency bands. Features from both of these branches of acoustic metamaterials can be used and these may contribute to achieving the right phase response needed for TS wave attenuation.

- A concept that has been proven to suppress certain TS waves involves a phonic crystal. This was shown numerically in the study by Hussein et al. [44]. In order to take this concept from something that has an unpractical geometry, can only work in an idealised numerical environment and with water as working fluid to something that works experimentally in air, is challenging. However, since this is one of the the most promising methods for boundary layer stability control without active actuation, it is worth investigating.

BIBLIOGRAPHY

[1] W. Tollmien, "Berechnung turbulenter Ausbreitungsvorgänge," *ZAMM Journal of Applied Mathematics and Mechanics / Zeitschrift für Angewandte Mathematik und Mechanik*, vol. 6, no. 6, pp. 468–478, 1926.

[2] H. Schlichting, "Zur enstehung der turbulenz bei der plattenströmung," *Nachrichten von der Gesellschaft der Wissenschaften*, 1933.

[3] G. B. Schubauer and H. K. Skramstad, "Laminar Boundary-Layer Oscillations and Stability of Laminar Flow," *Journal of the Aeronautical Sciences*, vol. 14, pp. 69–78, 2 1947.

[4] Y. Liu and X. Zhang, "Metamaterials: A new frontier of science and technology," 4 2011.

[5] T. L. Bergman, F. P. Incropera, D. P. DeWitt, and A. S. Lavine, *Fundamentals of Heat and Mass Transfer*. John Wiley & Sons, 7th ed., 2011.

[6] N. Fang, D. Xi, J. Xu, M. Ambati, W. Srituravanich, C. Sun, and X. Zhang, "Ultrasonic metamaterials with negative modulus," *Nature Materials*, vol. 5, pp. 452–456, 6 2006.

[7] Z. Yang, J. Mei, M. Yang, N. H. Chan, and P. Sheng, "Membrane-type acoustic metamaterial with negative dynamic mass," *Physical Review Letters*, vol. 101, pp. 1–4, 11 2008.

[8] Z. G. Wang, S. H. Lee, C. K. Kim, C. M. Park, K. Nahm, and S. A. Nikitov, "Acoustic wave propagation in one-dimensional phononic crystals containing Helmholtz resonators," *Journal of Applied Physics*, vol. 103, no. 064907, pp. 1–10, 2008.

[9] V. M. García-Chocano, R. Graciá-Salgado, D. Torrent, F. Cervera, and J. Sánchez-Dehesa, "Quasi-two-dimensional acoustic metamaterial with negative bulk modulus," *Physical Review B*, vol. 85, no. 184102, pp. 1–8, 2012.

[10] J. Li, W. Wang, Y. Xie, B. I. Popa, and S. A. Cummer, "A sound absorbing metasurface with coupled resonators," *Applied Physics Letters*, vol. 109, pp. 1–4, 8 2016.

[11] J. Fey and W. M. Robertson, "Compact acoustic bandgap material based on a subwavelength collection of detuned Helmholtz resonators," *J. Appl. Phys*, vol. 109, no. 114903, pp. 1–5, 2011.

[12] K. P. Flynn, R. L. Panton, and D. G. Bogard, "The effect of a row of Helmholtz resonators on the tubulence of a boundary layer," in *AIAA 2nd Shear Flow Conference*, American Institute of Aeronautics and Astronautics Inc, AIAA, 1989.

[13] J. C. Lin, F. G. Howard, D. M. Bushnell, and G. V. Selby, "Investigation of several passive and active methods for turbulent flow separation control," in *AIAA 21st Fluid Dynamics, Plasma Dynamics and Lasers Conference, 1990*, American Institute of Aeronautics and Astronautics Inc, AIAA, 1990.

[14] L. M. Mack, "Boundary Layer Linear Stability Theory," *Agard*, vol. 709, no. 3, pp. 1–81, 1984.

[15] T. Herbert, "Parabolized Stability Equations," in *AGARD, Special Course on Progress in Transition Modelling*, (Columbus, Ohio), pp. 1–34, 1993.

[16] J. van Ingen, "A suggested semi-empirical method for the calculation of the boundary layer transition region," *Technische Hogeschool Delft, Vliegtuigbouwkunde, Rapport VTH-74*, 1956.

[17] A. Smith and N. Gamberoni, *Transition, pressure gradient and stability theory*. Douglas Aircraft Company, El Segundo Division, 1956, 1956.

[18] D. R. Smith, J. B. Pendry, and M. C. Wiltshire, "Metamaterials and negative refractive index," 8 2004.

[19] V. G. Veselago, "The Elecrodynamics of Substances with Simultaneously Negative Values of epsilon and mu," *Soviet Physics Uspekhi*, vol. 10, pp. 509–514, 4 1968.

[20] F. Zangeneh-Nejad and R. Fleury, "Active times for acoustic metamaterials," *Reviews in Physics*, vol. 4, pp. 1–17, 11 2019.

[21] G. Ma and P. Sheng, "Acoustic metamaterials: From local resonances to broad horizons," *Science Advances*, vol. 2, p. e1501595, 2 2016.

[22] G. A. Reynolds and W. S. Saric, *Experiments on the stability of the flat-plate boundary layer with suction*. PhD thesis, 1986.

[23] M. R. Malik, "Prediction and control of transition in supersonic and hypersonic boundary layers," *AIAA Journal*, vol. 27, no. 11, pp. 1487–1493, 1989.

[24] A. S. Thomas, "The Control Of Boundary-Layer Transition Using A Wave-Superposition Principle," *Journal of Fluid Mechanics*, vol. 137, pp. 233–250, 1983.

[25] M. Kotsonis, R. K. Shukla, and S. Pröbsting, "Control of natural tollmien-schlichting waves using dielectric barrier discharge plasma actuators," *International Journal of Flow Control*, vol. 7, pp. 37–54, 6 2015.

[26] H. J. Tol, C. C. De Visser, and M. Kotsonis, "Experimental model-based estimation and control of natural Tollmien–Schlichting waves," *AIAA Journal*, vol. 57, no. 6, pp. 2344–2355, 2019.

[27] S. Biringen, "Active control of transition by periodic suction-blowing," *Physics of Fluids*, vol. 27, no. 6, pp. 1345–1347, 1984.

[28] H. W. Liepmann and D. M. Nosenchuck, "Active control of laminar-turbulent transition," *Journal of Fluid Mechanics*, vol. 118, pp. 201–204, 1982.

[29] M. Kotsonis, S. Ghaemi, L. Veldhuis, and F. Scarano, "Measurement of the body force field of plasma actuators," *Journal of Physics D: Applied Physics*, vol. 44, pp. 1–11, 2 2011.

[30] G. Ma, M. Yang, S. Xiao, Z. Yang, and P. Sheng, "Acoustic metasurface with hybrid resonances," *Nature Materials*, vol. 13, pp. 873–878, 9 2014.

[31] Z. Lu, X. Yu, S. K. Lau, B. C. Khoo, and F. Cui, "Membrane-type acoustic metamaterial with eccentric masses for broadband sound isolation," *Applied Acoustics*, vol. 157, pp. 1–12, 1 2020.

[32] S. H. Lee, C. M. Park, Y. M. Seo, Z. G. Wang, and C. K. Kim, "Acoustic metamaterial with negative density," *Physics Letters A*, vol. 373, pp. 4464–4469, 2009.

[33] G. L. Huang and C. T. Sun, "Band gaps in a multiresonator acoustic metamaterial," *Journal of Vibration and Acoustics, Transactions of the ASME*, vol. 132, no. 031003, pp. 1–6, 2010.

[34] E. H. El Boudouti, T. Mrabti, H. Al-Wahsh, B. Djafari-Rouhani, A. Akjouj, and L. Dobrzynski, "Transmission gaps and Fano resonances in an acoustic waveguide: Analytical model," *Journal of Physics Condensed Matter*, vol. 20, 6 2008.

[35] U. Fano, "Effects of configuration interaction on intensities and phase shifts," *Physical Review*, vol. 124, pp. 1866–1878, 12 1961.

[36] H. Myers, *Introductory Solid State Physics*. Taylor & Francis, 2nd ed., 2 1990.

[37] R. Hedayati and S. Lakshmanan, "Pneumatically-actuated acoustic metamaterials based on helmholtz resonators," *Materials*, vol. 13, no. 1456, pp. 1–11, 2020.

[38] B. Xia, N. Chen, L. Xie, Y. Qin, and D. Yu, "Temperature-controlled tunable acoustic metamaterial with active band gap and negative bulk modulus," *Applied Acoustics*, vol. 112, pp. 1–9, 2016.

[39] J. Li and C. T. Chan, "Double-negative acoustic metamaterial," *Physical Review E*, vol. 70, no. 055602(R), pp. 1–4, 2004.

[40] G. Hu, L. Tang, and X. Cui, "On the modelling of membrane-coupled Helmholtz resonator and its application in acoustic metamaterial system," *Mechanical Systems and Signal Processing*, vol. 132, pp. 595–608, 10 2019.

[41] G. Hu, L. Tang, and Y. Yang, "Acoustic metamaterial containing an array of Helmholtz resonators coupled with mass-loaded membranes," p. 48, SPIE-Intl Soc Optical Eng, 4 2020.

[42] M. Yang, G. Ma, Z. Yang, and P. Sheng, "Coupled membranes with doubly negative mass density and bulk modulus," *Physical Review Letters*, vol. 110, pp. 1–5, 3 2013.

[43] P. W. Carpenter, A. D. Lucey, and C. Davies, "Progress on the use of compliant walls for laminar-flow control," *Journal of Aircraft*, vol. 38, no. 3, pp. 504–512, 2001.

[44] M. I. Hussein, S. Biringen, O. R. Bilal, and A. Kucala, "Flow stabilization by subsurface phonons," *Proceedings of the Royal Society A: Mathematical, Physical and Engineering Sciences*, vol. 471, no. 20140928, 2015.

[45] M. Gaster, "Is the Dolphin a Red Herring?," in *Turbulence Management and Relaminarisation*, pp. 285–304, Berlin, Heidelberg: Springer Berlin Heidelberg, 1988.

[46] R. Zhao, T. Liu, C. Y. Wen, J. Zhu, and L. Cheng, "Impedance-Near-Zero Acoustic Metasurface for Hypersonic Boundary-Layer Flow Stabilization," *Physical Review Applied*, vol. 11, 2019.

[47] A. Fedorov, "Transition and Stability of High-Speed Boundary Layers," *Annual Review of Fluid Mechanics*, vol. 43, pp. 79–95, 1 2011.

[48] T. Pagliaroli, F. Patanè, A. Pagliaro, P. Lv, and A. Tatí, "Metamaterials for hypersonic flow control: Experimental tests on novel ultrasonically absorptive coatings," in *5th IEEE International Workshop on Metrology for AeroSpace, MetroAeroSpace 2018 - Proceedings*, pp. 284–289, 2018.

[49] R. L. Panton and J. M. Miller, "Excitation of a Helmholtz resonator by a turbulent boundary layer," *The Journal of the Acoustical Society of America*, vol. 58, pp. 800–806, 10 1975.

[50] R. Ma, P. E. Slaboch, and S. C. Morris, "Fluid mechanics of the flow-excited Helmholtz resonator," *Journal of Fluid Mechanics*, vol. 623, pp. 1–26, 2009.

[51] COMSOL Multiphysics v. 5.4, "Acoustics Module User's Guide," 2018.

[52] COMSOL Multiphysics v. 5.4, "CFD module User's Guide," 2018.

[53] COMSOL Multiphysics v. 5.4, "Heat Transfer User's Guide," 2018.

[54] N. Benard and E. Moreau, "Capabilities of the dielectric barrier discharge plasma actuator for multi-frequency excitations," *Journal of Physics D: Applied Physics*, vol. 43, no. 145201, 2010.

[55] R. D. Keane and R. J. Adrian, "Optimization of particle image velocimeters: II. Multiple pulsed systems," *Measurement Science and Technology*, vol. 2, pp. 963–974, 10 1991.

[56] M. Raffel, C. E. Willert, F. Scarano, C. J. Kähler, S. T. Wereley, and J. Kompenhans, *Particle Image Velocimetry*. Cham: Springer International Publishing, 2018.

[57] F. Scarano and M. L. Riethmuller, "Advances in iterative multigrid PIV image processing," in *Experiments in Fluids*, vol. 29, pp. S51–S60, Springer Verlag, 2000.

[58] A. Sciacchitano and B. Wieneke, "PIV uncertainty propagation," *Measurement Science and Technology*, vol. 27, 6 2016.

[59] LaVision, "PIV Uncertainty Quantification," 2018.

A MATLAB CODE ADJUSTED PSE

A.1 ARBITRARY V-VELOCITY BOUNDARY CONDITION

The Matlab code presented here is part of a program that solves the PSE equations which is developed in the TU Delft boundary layer stability research group of Dr. M. Kostonis. This part described how an arbitrary boundary condition is applied. In this case, the pressure at the wall is evaluated from the eigenvector (denoted with ϕ) and modified with A_{BC} and Ang_{BC} to obtain a v-velocity boundary condition at the wall.

```
% Form LHS matrix and RHS vector
Ml   = A + B/dx + C*dax;
Mr   =      B/dx*phi(:,i-1);

% Apply b.c.'s
Ml(1,:)=[Zr Zr Zr Zr];
Ml(1,1)=1;
Mr(1)=0;                % u freestream

Ml(N,:)=[Zr Zr Zr Zr];
Ml(N,N)=1;
Mr(N)=0;                % u wall

Ml(N+1,:)=[Zr Zr Zr Zr];
Ml(N+1,N+1)=1;
Mr(N+1)=0;              % v freestream

Ml(2*N,:)=[Zr Zr Zr Zr];
Ml(2*N,2*N)=1;
 Phase_p = angle(phi(4*N,i)); % Extract phase of p wall
Amp_p = abs(phi(4*N,i));      % Extract amplitude of p wall
 Phase_v = Phase_p+ang_bc;    % Add arbitrary phase constant
Amp_v = Amp_p*a_bc(i)/dx;        % Multiply with amplitude factor
Mr(2*N)= Amp_v*exp(1j*Phase_v);       % inhomogeneous BC v wall

Ml(2*N+1,:)=[Zr Zr Zr Zr];
Ml(2*N+1,2*N+1)=1;
Mr(2*N+1)=0;            % w freestream

Ml(3*N,:)=[Zr Zr Zr Zr];
Ml(3*N,3*N)=1;
Mr(3*N)=0;              % w wall

Ml(3*N+1,:)=[Zr   -D2(1,:)/Re    Zr        D1(1,:)];      % compatibility p freestream

Ml(4*N,:)=[Zr    -D2(end,:)/Re    Zr        D1(end,:)];    % compatibility p wall
```

```
37
38 % Solve problem
39 phi(:,i) = Ml\Mr;
```

A.2 MODELLING OF RESONATOR

The modelling of the resonator is done by coupling the outcome from the thermoviscous acoustics simulation to the adjusted PSE solver. This is done by a linear, dimensional transfer function that comes from the thermoviscous acoustics simulation which relates driving pressure to resulting velocity coming from the Helmholtz resonator in the frequency spectrum. The absolute values and phase angles of the pressure and velocity are stated in a lookup table in 'Res68mm.txt'. The function 'Resonator' is called in the part where the v-velocity boundary condition at the wall is imposed. The code given below can therefore be placed on lines 20-24 of the code listed in A.1.

```
p_in = phi(4*N,i);              % Extract p wall
p_in_Dim = p_in*rho*Uo^2;     % Dimensionalise pressure
vbc = resonator(p_in_Dim,F,dStar,dx);    % Call function
    Resonator
Mr(2*N) = a_bc(i)*vbc/(Uo); % inhomogeneous BC v wall

function vbc = resonator(p_in,f_in,dStar,dx)
%% Resonator geometry
tS = 1e-3;              % Throat width [mm]
tS_nd = tS/dStar;    % Non-dimensionalise width dStar

%% Load results from COMSOL
Vf = load('Res68mm.txt');

%% Extract phase and amplitude from input pressure
abs_p_in = abs(p_in);
phase_p_in = rad2deg(angle(p_in));

%% Interpolate to the right frequency response
abs_p_ref = interp1(Vf(:,1),Vf(:,2),f_in);
abs_v_res = interp1(Vf(:,1),Vf(:,4),f_in);
phase_p_ref = interp1(Vf(:,1),Vf(:,3),f_in);
phase_v_res = interp1(Vf(:,1),Vf(:,5),f_in);

abs_p_ref_ND = abs_p_ref;
abs_v_res_ND = abs_v_res;

A_BC = abs_p_in/abs_p_ref_ND;
phi_BC = phase_p_in - phase_p_ref;

%% Determine response vbc
abs_vbc = abs_v_res_ND * A_BC;
phase_vbc = phase_v_res + phi_BC;

vbc_res = abs_vbc * exp(1i*deg2rad(phase_vbc));          %
    Transform to complex number
vbc = vbc_res * tS_nd / dx;                                %
    Spread effect over one x-step
```